

NUMERICAL LES FOR MVG CONTROLLED SUPERSONIC RAMP FLOW

by

Xiao Wang

Presented to the Faculty of the Graduate School of
The University of Texas at Arlington in Partial Fulfillment
of the Requirements
for the Degree of

DOCTOR OF PHILOSOPHY

THE UNIVERSITY OF TEXAS AT ARLINGTON

December 2014

Copyright © by Xiao Wang 2014

All Rights Reserved



Acknowledgements

Initially, I would like to thank my research advisor and committee chairman, Dr. Chaoqun Liu, for his guidance, advice, continuous support, encouragement, patience and understanding in both academics and life throughout my six years of study. I have learned a lot from him.

Also, I would like to thank the other committee members, Dr. Hristo Kojouharov, Dr. Guojun Liao, Dr. Rencang Li and Dr. Yue Liu, for their understanding and support.

I would like to thank the Department of Mathematics, for the financial support during the long semesters through Graduate Teaching Assistantships. I would also like to thank all colleagues for making my time at University of Texas at Arlington a great experience, especially my friends Huankun Fu and Yonghua Yan, for their help and encouragement.

Finally, I am extremely grateful to my family, for their unconditional love, understanding, kind support and encouragement. I can't finish without your support. Thank you.

November 21, 2014

Abstract

NUMERICAL LES FOR MVG CONTROLLED SUPERSONIC RAMP FLOW

Xiao Wang, PhD

The University of Texas at Arlington, 2014

Supervising Professor: Chaoqun Liu

An implicitly implemented large eddy simulation by using the fifth order bandwidth-optimized WENO scheme is applied to make comprehensive studies on ramp flows with micro-ramp vortex generators (MVG) at Mach 2.5 and $Re_\theta=5760$. Detailed mechanism and topology of flow structure after MVG was studied to make better understanding.

A series of new findings are obtained about the MVG-ramp flow including the three-dimensional vortex structure generated by MVG. The mechanism about the formation of vortex ring structure and momentum deficit after MVG is deeply studied. Small scale vortical structures in the rear separation and wake near the trailing edge of MVG was also analyzed. New conceptual model of the flow topology was suggested.

The two dimensional stability analysis on compressible flat plate with zero attack angle was carried out to set up for further stability analysis. Results from compressible blasius solution was analyzed for stability using global method with second order finite-difference discretization.

Table of Contents

Acknowledgements	iii
Abstract	iv
List of Illustrations	viii
List of Tables	xi
Chapter 1 INTRODUCTION.....	1
Chapter 2 NAVIER-STOKES EQUATIONS.....	6
2.1 Conservation Laws and the Equations	6
2.2 Non-Dimensional Form.....	7
2.3 Expansion in Curvilinear Coordinates	8
Chapter 3 NUMERICAL METHODS FOR SUPERSONIC RAMP FLOW	11
3.1 Numerical Scheme	11
3.1.1. The 5th Order Bandwidth-optimized WENO Scheme for the Convective Terms.....	11
3.1.2 The Difference Scheme for the Viscous Terms	15
3.1.3 The Temporal Scheme.....	15
3.2 Grid Generation	15
3.3 Boundary Conditions	20
3.4 Code Validation	22
Chapter 4 NUMERICAL LES AND ANALYSIS OF VORTEX STRUCTURE BEHIND SUPERSONIC MVG	26
4.1 Inflow Boundary Layer Profiles	26
4.2 Results of the MVG Controlled Ramp Flow - Vortex Rings.....	27
4.2.1 Velocity Profile Behind MVG	27
4.2.2 The New Dynamic Vortex Model.....	28

4.2.3. Vortex Rings - A New Mechanism in MVG-ramp Flow Control.....	30
4.2.4 Analysis of The Structure of Vortex Rings	31
4.2.5 Conservation of Vorticity	38
4.3 Stability Analysis to the Velocity Profile.....	41
4.3.1 Derivation of Linear Stability Equation	43
4.3.2 Stability Analysis to the Averaged Velocity Profile	44
Chapter 5 INVESTIGATION OF MOMENTUM DEFICIT.....	48
5.1 The Momentum Deficit	48
5.1.1 The deficit in the mean flow.....	48
5.1.2 The deficit in the instantaneous flow	51
5.1.3 The mean and instantaneous streamwise vortical structure	53
5.2. The Origin of Momentum Deficit.....	55
5.3 The Position Alternation – A Revised Mechanism	57
Chapter 6 VORTICAL STRUCTURES IN THE REAR SEPARATION AND WAKE AFTER MVG	60
6.1. Two-Dimensional Representation of the Rear Separation	61
6.2. Three-Dimensional Representation of the Rear Separation.	63
6.3. Similar Vortical Structure in the Micro-Ramp Wake	65
6.4 Conclusions and new conceptual topology model	67
Chapter 7 STABILTIY ANALYSIS OF COMPRESSIBLE FLOW PASSING A FLAT PLATE	69
7.1 The derivation of linear stability equations	69
7.1.1. Basic Flow	70
7.1.2 Compressible Linear Stability Equations.....	71
7.2 Second Order Finite-Difference (2FD) Method	75

7.3 Numerical Results.....	77
Chapter 8 CONCLUDING REMARKS	80
Appendix A The non-zero elements of the coefficient matrix B, C in Eq. (7.28).....	82
References	85
Biographical Information	92

List of Illustrations

Figure 3.1 Grid Stencils for 5 th Order WENO.....	11
Figure 3.2 Grid Stencils for 5 th Order Bandwidth-optimized WENO	13
Figure 3.3 The Geometry of MVG.....	16
Figure 3.4 The Schematic of the Half Grid System	16
Figure 3.5 The Geometry Sketch of the Ramp	17
Figure 3.6 The Grid System of Case 1	17
Figure 3.7 The Local View of Grids around the Trailing-edge	18
Figure 3.8 The Surface Grids of MVG	18
Figure 3.9 The Grids in Certain Cross-section	19
Figure 3.10 The Grids at the Foot of the Trailing-edge.....	19
Figure 3.11 The Grids at the Ramp Corner	20
Figure 3.12 The Contour of the Pressure	22
Figure 3.13 The Comparison of the Pressure.....	22
Figure 3.14 The Comparison of the Shock Location with that of Rusunov.....	23
Figure 3.15 The Converging History of the 5th WENO Scheme	23
Figure 3.16 The Pressure Contour at the Central Plane and Body Surface.....	24
Figure 3.17 The Spatial Streamlines.....	24
Figure 3.18 Comparison of Flow Structures at Ramp.....	25
Figure 3.19 Comparison of Flow Structures after MVG	25
Figure 4.1 Inflow Boundary-layer Profile Comparison with GUARINI et al's	27
(a) Averaged Velocity Profile behind MVG (b) Averaged Velocity Profile by Babinsky et al	
Figure 4.2 Qualitative Comparison of Averaged Velocity Profile behind MVG.....	28
Figure 4.3 The dynamic vortex model (Li and Liu[37])	29
Figure 4.4 Surface flow visualization image and the vortex model given by	29

Figure 4.5 The Comparison between Computation and the Experiment of Lu[56]	29
Figure 4.6 The Instantaneous Spatial Streamlines	30
Figure 4.7 The Iso-surface of the Instantaneous Pressure	31
Figure 4.8 Vortex rings shown by iso-surface of λ_2	32
Figure 4.9 The Numerical Shilieren at the Center Plane[51]	33
Figure 4.10 The Laser-sheet Flash Image at the Center Plane (Lu et al 2010)	33
Figure 4.11 K-H rings behind MVG by (Sun et al 2011)	34
Figure 4.12 Distribution of K-H Vortices and Streamwise Vortices from LES[58]	34
Figure 4.13 Vortex Rings shown by the Components of Vorticity[58]	35
Figure 4.14 Part of the Ring Structure shown by Total Vorticity Magnitude (left) and each Components (right)[58]	36
Figure 4.15 Part of the Ring Structure shown by λ_2 (from the bottom view)[58]	36
Figure 4.16 The Velocity Field on the Cross Section[58]	37
Figure 4.17 The Velocity Field close to the Foot (left) and the Head (right) of a Vortex Ring[58]	38
Figure 4.18 The Scope for Vorticity Magnitude Check	39
Figure 4.19 The Instantaneous Vorticity Distribution(Y Yan et al)	39
Figure 4.20 Averaged Streamwise Velocity at Different Sections	42
Figure 4.21 Inflection Points (surface for 3-D)	42
Figure 4.22 Eigenvector Function of \hat{v}	46
Figure 4.23 The Instantaneous Vorticity Distribution[57]	47
Figure 5.1 An overview of the streamwise development of the micro-ramp wake, cross- sections are at $x/h=1, 9$ and 17 respectively	49
Figure 5.2 Cross-sections of mean u and v contours at three streamwise positions with two-dimensional vectors overlaid	51

Figure 5.3 Cross-sections of instantaneous u and v contours at three streamwise positions with two-dimensional vectors overlaid.	52
Figure 5.4 Cross-sectional contours of streamwise component of vorticity ω_x	54
Figure 5.5 Streamlines with origins at different wall-normal positions upstream of the microramp.	56
Figure 5.6 Streamlines with origins at a fixed spanwise position $z/h=1.1$	57
Figure 5.7. The projected streamline in the x - y plane, the streamlines are those in figure 5.6(a).	58
Figure 5.8 The streamwise and wall-normal velocity components along the extracted streamlines(Sun et al.).	59
Figure 6.1 Experimental visualization of the rear separation.	60
Figure 6.2. The spiral point at the rear	61
Figure 6.3. Contour of u at four heights with projected streamlines.	62
Figure 6.4. Vortex lines passing vortex cores of V2 and V1.	63
Figure 6.5. The three-dimensional representation of the rear separation regions using isosurface of $u=-0.01U_\infty$	64
Figure 6.6 The Ω -shaped vortex lines around reverse region 1.	65
Figure 6.7. The three-dimensional representation of the micro-ramp wake with vortex lines.	66
Figure 6.8 The three vortex lines after removing the isosurface in Fig. 6.7.	67
Figure 6.9. The conceptual model of the flow topology.	68
Figure 7.1. Velocity profile in a compressible laminar boundary-layer over our flat plate	71
Figure 7.2. Velocity profile near boundary layer used in numerical analysis	78
Figure 7.3 Eigenvector Function at $Re_x = 187,000$	78
Figure 7.4 Eigenfunction of compressible stability equations for comparison	79

List of Tables

Table 3.1 The Geometric Parameters for the Computation.....	20
Table 6.1 The coordinates of the revealed vortices in Fig. 6.3.	63
Table 7.1 Flow Parameters	78

Chapter 1

INTRODUCTION

Micro vortex generators (VG) are a kind of low-profile passive control device designed for the boundary layer control. In contrast to the conventional VG (widely used in aviation applications and with height (h) of the order of the boundary-layer (δ)), micro VG has a height approximately 20-40% of the boundary layer[1-3]. As we know, in the supersonic ramp flows, shock boundary layer interaction (SBLI) can significantly reduce the quality of the flow field by triggering large-scale separation, causing total pressure loss, and making the flow unsteady and distorting. The consequences of the interaction often degrade the performance of the engine and even make an engine unable to start. Micro VG is a new device which is designed to alleviate or overcome such difficulties and, therefore, to improve the “health” of the boundary layer. There are more than one kind of micro VG, like the micro vane and micro ramp VG (MVG). Because MVG has a more robust structure, it becomes more attractive to the inlet designer. Intensive computational and experimental studies have been made on it recently.

A series of experimental and computational investigations have been carried out. The most prominent experimental studies reported are those by Babinsky[4-7]. He made a series of experiments on different kinds of micro VGs and investigated their control effects in detail. The mechanism of MVG flow control from his work concludes that a pair of counter-rotating primary streamwise vortices is generated by MVG, which are mainly located within the boundary layer and travel downstream for a considerable distance. Secondary vortices are located underneath the primary ones and even more streamwise vortices could be generated under suitable conditions. Streamwise vortices inside the boundary later bring low momentum fluid up from the bottom and high momentum fluid down to the boundary layer. A striking cylindrical momentum deficit region is observed in the wake behind the MVG. The vortices keep lifting up slowly, which is thought to be the consequence of the upwash effect of the vortices.

As we know, the purpose of the MVG is to control the shock induced separation and to improve the quality of the boundary layer velocity profile after the SBLI. Numerical simulations have been made on MVG for comparative study and further design purposes. Ghosh, Choi and Edwards [8] made detailed computations under the experimental conditions given by Babinsky. These numerical studies include RANS computations and hybrid RANS/LES computations using immersed boundary (IB) techniques. The fundamental structures, like the streamwise vortices and momentum deficit, were reproduced by the computation. Lee et al [9] also made computations on the micro VGs problems by using Monotone Integrated Large Eddy Simulations (MILES). In their computation, the MVG is placed in a domain with the configuration following the real wind tunnel. The fundamental wave system of the MVG were reproduced in the computation, which consists of the main shock, expansion waves and re-compression shock like that reported by Babinsky [6]. They [10] further tested several variations of the standard MVG and micro vane to enhance the control effect. Also some well recognized study on the characteristics of MVG can be found from the work by Dolling [11-13], Settles [14], Dussauge [15], Andreopoulos [16], Loginov [17] and their collaborators. For numerical simulations, there are three basic categories, i.e., the RANS, LES and DNS. It is well-known that RANS models do not perform well for SWTBLI (Wilcox [18], 1993). According to Zheltovodov's opinion [19], the existing RANS models cannot solve the strong SBLI problem accurately, including the supersonic ramp flow. About the numerical works of LES, Rizzetta and Visbal [20] made simulations on a compression corner by implicit LES using a high-order method; Kaenal, Kleiser, Adams, and Loginov et al conducted LES [21] on ramp flow using an approximate de-convolution model developed by Stolz. The comparisons were made and some agreement was obtained between the computational and the available experimental results. The first DNS on supersonic ramp flow was made by Adams for a 10° compression ramp at Mach 3 and $Re_\theta=1685$. In the work done by Adams [22] and his colleagues, the 5th order hybrid compact-ENO scheme was applied. Later Martin and the collaborators made a series of remarkable

investigations by using DNS [23-28]. Comparisons were made between the computation and the experiments from the low Reynolds number wind tunnel at Princeton University [29]. They used the fifth order bandwidth-optimized WENO scheme which is the same scheme that the current work uses. The effect of low Reynolds number on the separation was studied. More work on MVG and other flow control tools have been done recently [30-35]. According to the experimental and numerical research, some flow mechanisms are recognized as: a) the amplification of the turbulence after the SBLI is thought to be caused by the nonlinear interaction between the shock wave and the coupling of turbulence, vorticity and entropy waves [36]; b) the unsteady motion of the shock is considered to be generated by the very long low-momentum coherent structures in logarithmic layer and such structures might be formed by the hairpin vortex packet.

In order to carry out flow control more effectively using MVG, the mechanism of the flow should be carefully studied first. There are at least three problems which should be clarified: a) what is the three-dimensional structures of the wave system caused by MVG. b) what is the relation between the momentum deficit and the flow structure and where does the low speed fluid come from? c) Is there any new mechanism besides the pronounced momentum transportation and mixing by streamwise vortices?

In this study, we investigate the control effect of MVG on the supersonic ramp flow with a fully developed turbulent inflow by numerical simulations, and further explore the mechanisms related to those questions mentioned above. Numerical simulations are made on supersonic ramp flow with MVG at Mach 2.5 and $Re_\theta=5760$. The trailing edge declining angle of the MVG is 70° in computation. A large eddy simulation method is used by solving the unfiltered form of the Navier-Stokes equations (NSEs) with the 5th order bandwidth-optimized WENO scheme, which is generally referred to as implicitly implemented LES(ILES) [37,38]. Without explicitly using the subgrid scale (SGS) model as the explicit LES, the implicitly implemented LES uses the intrinsic dissipation of the numerical method to dissipate the turbulent energy accumulated at the

unresolved scales with high wave numbers. There are two main subfields about this category, i.e., the MILES [39,40] by Boris, Fureby and Grinstein, et al, and the implicit LES [41, 42] by Visbal, Rizzetta and Gaitonde, et al. The first subfield is based on modified equation analysis, and typically uses the high order monotone scheme like flux-corrected transport (FCT) scheme or piecewise parabolic method (PPM). The *ENO* algorithm was also reported being used as the limiter in Ref. [41]. This kind of method can be used to solve the supersonic problems with shock waves, but the order of the scheme should not be competitive to the modern high order schemes like the compact schemes or *WENO* schemes with 5th order of accuracy or higher. The second one [42] specifically uses the high order compact scheme by Lele and the high order Pade-type low-pass spatial filter. However, the published applications of the method are only for the low speed flow. When the same numerical algorithms were used on supersonic problems [43-44], the Smagorinsky dynamic SGS model was incorporated in the simulation, which implies the existence of issues related to the numerical stability. A series of shock-capturing schemes were also tried for large eddy simulation [45-46], including the *WENO* scheme. As mentioned in Ref.[46], at low Mach number the investigated compact differencing and filter scheme formulation may give better results but as the Mach number increases the relative suitability of the *ENO* method increases. However, the *ENO* scheme still produces numerical turbulence thus stabilizing filters is needed, while the *WENO* scheme does not need filtering. Recently, an evaluating computation was reported on circular cylinder flow using implicitly implemented LES by the 5th *WENO* scheme [47]. Comparisons were made between the computation and the experiment. The results show that the numerical algorithm is feasible and efficient. For the studied supersonic MVG controlled ramp flow problem, there are complex shock wave system, strong shock-vortex interaction and small scale structures. Considering the above status of implicitly implemented LES, the method by solving the NSEs with the 5th order bandwidth-optimized *WENO* scheme is used in the paper and considered as certain implicitly implemented LES[48-51].

Since the main formation of momentum deficit and vortical structures is the shear layer instability[57-58], it is necessary to study the wake instability of MVG. Global method and second order finite difference meshing[59-61] was used to the analysis of the stability of compressible viscous flow over a flat plate. The result could lead to further spatial stability analysis of nonlinear three dimensional compressible flow behind MVG.

The structure of the dissertation is as follows. In Chapter 2, the Navier-Stokes equations are introduced. In Chapter 3, the numerical scheme, the grid information and the boundary conditions are discussed. In Chapter 4, the study of ring vortex structures after MVG are presented; In Chapter 5, the mechanism of momentum deficit is analyzed in detail. In Chapter 6, small length scale structures around trailing edge of MVG is studied. Finally, in Chapter 7, two dimensional stability of compressible flow over a flat plate was studied.

Chapter 2

NAVIER-STOKES EQUATIONS

2.1 Conservation Laws and the Equations

The motion of a fluid can be described by the conservation of mass, momentum, and of energy for an arbitrary small control volume.

Consider a closed surface S whose position is fixed with relation to the coordinate axes and encloses a volume V completely filled with fluid. Given the density of the fluid ρ , the momentum $\rho \mathbf{u}$, the total energy E at a position x and at time t , the Navier-Stokes equations can be derived as follows from the conservation laws of mass, momentum and energy:

$$\frac{\partial \rho}{\partial t} + \nabla \cdot (\rho \mathbf{u}) = 0 \quad (2.1)$$

$$\frac{\partial (\rho \mathbf{u})}{\partial t} + \nabla \cdot (\rho \mathbf{u} \otimes \mathbf{u}) = (\nabla \cdot \sigma) \quad (2.2)$$

$$\frac{\partial (\rho E)}{\partial t} + \nabla \cdot (\rho E \mathbf{u}) - \nabla \cdot (k \nabla T) - \nabla \cdot (\sigma \cdot \mathbf{u}) = 0 \quad (2.3)$$

With

$$E = e + \frac{\mathbf{u} \cdot \mathbf{u}}{2} \quad (2.4)$$

and

$$\sigma = - \left[p + \frac{2}{3} \mu (\nabla \cdot \mathbf{u}) \right] \mathbf{I} + \mu [\nabla \mathbf{u} + (\nabla \mathbf{u})^T] \quad (2.5)$$

Here, σ is the internal shear stress, e is the internal energy per unit mass of the fluid, p denotes the pressure, T represents the temperature, k is the thermal conductivity and μ is the dynamic viscosity. Stokes(1845) assumption (linear relation between the stress and the rate of strain of the fluid) is used in obtaining the equation (2.5).

In three dimensions, the system above contains five equations (the conservation of momentum equation becomes three separate equations). Two extra equations are needed to

solve the system for the unknown variables ρ, \mathbf{u}, p, E , and T . These equations are the equation of state, for a thermally perfect gas,

$$p = \rho RT \quad (2.6)$$

where R is a gas constant, and the equation for internal energy equation,

$$e = c_v T \quad (2.7)$$

2.2 Non-Dimensional Form

Equations (2.1)-(2.6) can be reduced to a non-dimensional form. This can be achieved by dividing each variable by an appropriate dimensional reference parameter. Those reference parameters are defined as follows, where ∞ indicates incoming or free stream values:

L is the characteristic length;

V_∞ is the speed;

ρ_∞ is the density;

p_∞ is the pressure;

T_∞ is the temperature;

μ_∞ is the dynamic viscosity;

k_∞ is the thermal conductivity.

With these reference parameters, the non-dimensional variables are given by

$$t = \frac{t^*}{L/V_\infty}, \quad \mathbf{x} = \frac{\mathbf{x}^*}{L}, \quad \mathbf{u} = \frac{\mathbf{u}^*}{V_\infty}, \quad p = \frac{p^*}{\rho_\infty V_\infty^2}, \quad \sigma = \frac{\sigma^*}{\rho_\infty V_\infty^2} \quad (2.8)$$

where $*$ represents the dimensional variables.

We can rewrite the equations of section 2.1 in non-dimensional form, obtaining:

$$\frac{\partial \rho}{\partial t} + \nabla \cdot (\rho \mathbf{u}) = 0 \quad (2.9)$$

$$\frac{\partial (\rho \mathbf{u})}{\partial t} + [\nabla \cdot (\rho \mathbf{u} \otimes \mathbf{u})] = (\nabla \cdot \sigma) \quad (2.10)$$

$$\frac{\partial (\rho E)}{\partial t} + \nabla \cdot (\rho E \mathbf{u}) - \frac{\gamma}{RePr} \nabla \cdot (\nabla T) - \gamma(\gamma - 1) M_\infty^2 \nabla \cdot (\sigma \cdot \mathbf{u}) = 0 \quad (2.11)$$

$$\sigma = - \left[p + \frac{2}{3} \frac{1}{Re} \mu(T) (\nabla \cdot \mathbf{u}) \right] \mathbf{I} + \frac{1}{Re} \mu(T) [\nabla \mathbf{u} + (\nabla \mathbf{u})^T] \quad (2.12)$$

$$p = \frac{1}{\gamma M_\infty^2} \rho T \quad (2.13)$$

The Reynolds number is defined as

$$Re = \frac{\rho_\infty V_\infty L}{\mu_\infty} \quad (2.14)$$

while the Prandtl number evaluated at the reference conditions is given by

$$Pr = \frac{c_p \mu_\infty}{k_\infty} \approx 0.72 \quad (2.15)$$

and the Mach number is defined as

$$M_\infty = \frac{V_\infty}{\sqrt{\gamma R T_\infty}} \quad (2.16)$$

The dynamic viscosities coefficient is given by Sutherland's equation:

$$\mu = T^{\frac{3}{2}} \frac{1+C}{T+C}, \quad C = \frac{110.4}{T_\infty} \quad (2.17)$$

2.3 Expansion in Curvilinear Coordinates

In vector form, we may rewrite the equations as

$$\frac{\partial Q}{\partial t} + \frac{\partial E}{\partial x} + \frac{\partial F}{\partial y} + \frac{\partial G}{\partial z} = \frac{\partial E_v}{\partial x} + \frac{\partial F_v}{\partial y} + \frac{\partial G_v}{\partial z} \quad (2.18)$$

where

$$Q = \begin{bmatrix} \rho \\ \rho u \\ \rho v \\ \rho w \\ e \end{bmatrix} \quad E = \begin{bmatrix} \rho u \\ \rho u^2 + p \\ \rho uv \\ \rho uw \\ (e+p)u \end{bmatrix} \quad F = \begin{bmatrix} \rho v \\ \rho vu \\ \rho v^2 + p \\ \rho vw \\ (e+p)v \end{bmatrix} \quad G = \begin{bmatrix} \rho w \\ \rho wu \\ \rho wv \\ \rho w^2 + p \\ (e+p)w \end{bmatrix} \quad (2.19)$$

$$E_v = \frac{1}{\text{Re}} \begin{bmatrix} 0 \\ \tau_{xx} \\ \tau_{xy} \\ \tau_{xz} \\ u\tau_{xx} + v\tau_{xy} + w\tau_{xz} + q_x \end{bmatrix} \quad (2.20)$$

$$F_v = \frac{1}{\text{Re}} \begin{bmatrix} 0 \\ \tau_{yx} \\ \tau_{yy} \\ \tau_{yz} \\ u\tau_{yx} + v\tau_{yy} + w\tau_{yz} + q_y \end{bmatrix} \quad (2.21)$$

$$G_v = \frac{1}{\text{Re}} \begin{bmatrix} 0 \\ \tau_{zx} \\ \tau_{zy} \\ \tau_{zz} \\ u\tau_{zx} + v\tau_{zy} + w\tau_{zz} + q_z \end{bmatrix} \quad (2.22)$$

$$q_x = \frac{\mu}{(\gamma-1)M_\infty^2 \text{Pr}} \frac{\partial T}{\partial x}, \quad q_y = \frac{\mu}{(\gamma-1)M_\infty^2 \text{Pr}} \frac{\partial T}{\partial y}, \quad q_z = \frac{\mu}{(\gamma-1)M_\infty^2 \text{Pr}} \frac{\partial T}{\partial z} \quad (2.23)$$

$$p = \frac{1}{\gamma M_\infty^2} \rho T \quad (2.24)$$

$$\tau = \mu \begin{bmatrix} \frac{4}{3} \frac{\partial u}{\partial x} - \frac{2}{3} \left(\frac{\partial v}{\partial y} + \frac{\partial w}{\partial z} \right) & \frac{\partial u}{\partial y} + \frac{\partial v}{\partial x} & \frac{\partial u}{\partial z} + \frac{\partial w}{\partial x} \\ \frac{\partial u}{\partial y} + \frac{\partial v}{\partial x} & \frac{4}{3} \frac{\partial v}{\partial y} - \frac{2}{3} \left(\frac{\partial w}{\partial z} + \frac{\partial u}{\partial x} \right) & \frac{\partial v}{\partial z} + \frac{\partial w}{\partial y} \\ \frac{\partial u}{\partial z} + \frac{\partial w}{\partial x} & \frac{\partial v}{\partial z} + \frac{\partial w}{\partial y} & \frac{4}{3} \frac{\partial w}{\partial z} - \frac{2}{3} \left(\frac{\partial u}{\partial x} + \frac{\partial v}{\partial y} \right) \end{bmatrix} \quad (2.25)$$

Let us assume that the position frame of reference is fixed in time, that is, the generalized coordinates do not change with time. Then, we can define the curvilinear coordinates in relation to the Cartesian coordinates as

$$\begin{cases} \xi = \xi(x, y, z) \\ \eta = \eta(x, y, z) \\ \zeta = \zeta(x, y, z) \end{cases} \quad (2.26)$$

The Navier-Stokes equations can be transformed into generalized coordinates system:

$$\frac{\partial \hat{Q}}{\partial \tau} + \frac{\partial \hat{E}}{\partial \xi} + \frac{\partial \hat{F}}{\partial \eta} + \frac{\partial \hat{G}}{\partial \zeta} = \frac{\partial \hat{E}_v}{\partial \xi} + \frac{\partial \hat{F}_v}{\partial \eta} + \frac{\partial \hat{G}_v}{\partial \zeta} \quad (2.27)$$

where $\hat{Q} = J^{-1}Q$ and

$$\hat{E} = J^{-1}(\xi_x E + \xi_y F + \xi_z G) \quad (2.28)$$

$$\hat{F} = J^{-1}(\eta_x E + \eta_y F + \eta_z G) \quad (2.29)$$

$$\hat{G} = J^{-1}(\zeta_x E + \zeta_y F + \zeta_z G)$$

(2.30)

$$\hat{E}_v = J^{-1}(\xi_x E_v + \xi_y F_v + \xi_z G_v) \quad (2.31)$$

$$\hat{F}_v = J^{-1}(\eta_x E_v + \eta_y F_v + \eta_z G_v) \quad (2.32)$$

$$\hat{G}_v = J^{-1}(\zeta_x E_v + \zeta_y F_v + \zeta_z G_v) \quad (2.33)$$

$$J^{-1} = \det \left(\frac{\partial(x, y, z)}{\partial(\xi, \eta, \zeta)} \right) \quad (2.34)$$

Chapter 3

NUMERICAL METHODS FOR SUPERSONIC RAMP FLOW

3.1 Numerical Scheme

3.1.1. The 5th Order Bandwidth-optimized WENO Scheme for the Convective Terms

The fifth-order WENO scheme was chosen to discrete the convective terms. For clarity, its implementation is explained with the one-dimensional hyperbolic equation,

$$\frac{\partial u}{\partial t} + \frac{\partial f(u)}{\partial x} = 0 \quad (3.1)$$

The semi-discretized equation by the conservative scheme can be written as,

$$\left(\frac{\partial u}{\partial t}\right)_j = -\frac{h_{j+1/2} - h_{j-1/2}}{\Delta x} \quad (3.2)$$

where $h_{j+1/2} = h\left(f_{j+1/2}\right)$ and for second order scheme, $h_{j+1/2} = f_{j+1/2}$.

The basic ideas of the weighted schemes like WENO are as follows,

Apply basic grid stencils and difference schemes on them; Combine these schemes on different stencils and get linear weights to obtain higher order; Obtain nonlinear weights to make the scheme adaptive to discontinuity like shock waves. Fig. 3.1 shows the basic grid stencils for standard 5th order WENO scheme [48]

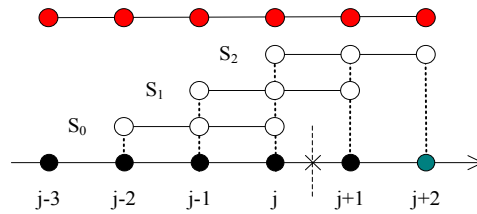


Figure 3.1 Grid Stencils for 5th Order WENO

Considering the positive flux, the three upwind-biased schemes on three candidates can be given as,

$$\begin{cases} h'^+_1 = \frac{1}{3}f_{j-2} - \frac{7}{6}f_{j-1} + \frac{11}{6}f_j \\ h'^+_2 = -\frac{1}{6}f_{j-1} + \frac{1}{3}f_j + \frac{5}{6}f_{j+1} \\ h'^+_3 = \frac{1}{3}f_j + \frac{5}{6}f_{j+1} - \frac{1}{6}f_{j+2} \end{cases} \quad (3.3)$$

The mark '+' refers to the positive flux after flux splitting. 3rd order is obtained for each individual scheme. Schemes on basic stencils are symmetric to the one with respect to $x_{j+1/2}$.

Weighting and the linear weights to obtain higher order:

$$h^{+}_{Linear, j+1/2} = \alpha_1 h'^+_1 + \alpha_2 h'^+_2 + \alpha_3 h'^+_3 \quad (3.4)$$

The optimal order for the weighted scheme is $2r + 1$, where r is the number of the stencil. The order of the scheme is 5th order. When the optimal order is realized, the α_i must be determined as:

$$(\alpha_1, \alpha_2, \alpha_3) = (0.1, 0.6, 0.3) \quad (3.5)$$

The nonlinear weighted schemes can be expressed as:

$$h^{+}_{j+1/2} = w_1 h'^+_1 + w_2 h'^+_2 + w_3 h'^+_3 \quad (3.6)$$

where w_i is changing from place to place, and

$$w_i = b_i / (b_1 + b_2 + b_3) \quad (3.7)$$

$$b_i = \alpha_i / (\varepsilon + IS_i)^2 \quad (3.8)$$

and ε is a small quantity to prevent the denominator from being zero, which should be small enough in supersonic problems with shocks ($10^{-6} \sim 10^{-10}$). IS_i is the smoothness measurement.

In order to make the nonlinear scheme still pertain the same optimal order, i.e., 5th order, IS_i should have the property:

$$IS_k = C(1 + O(h^2)) \quad (3.9)$$

where C is the same number for three IS_i .

IS_i for 5th order WENO scheme has the following form:

$$\begin{cases} IS_1 = \frac{13}{12}(f_{j-2} - 2f_{j-1} + f_j)^2 + \frac{1}{4}(f_{j-2} - 4f_{j-1} + 3f_j)^2 \\ IS_2 = \frac{13}{12}(f_{j-1} - 2f_j + f_{j+1})^2 + \frac{1}{4}(f_{j-1} - f_{j+1})^2 \\ IS_3 = \frac{13}{12}(f_j - 2f_{j+1} + f_{j+2})^2 + \frac{1}{4}(3f_j - 4f_{j+1} + f_{j+2})^2 \end{cases} \quad (3.10)$$

The scheme for $h_{j+\frac{1}{2}}^-$ has a symmetric form of $h_{j+\frac{1}{2}}^+$ to the point $x_{j+\frac{1}{2}}$

Comparing to the standard 5th order WENO scheme discussed above, the 5th order Bandwidth-optimized WENO scheme uses one more point on the right, thus it has one more grid stencil [24],

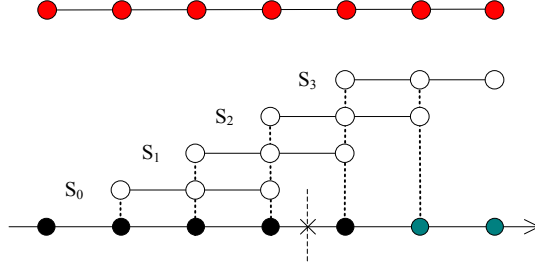


Figure 3.2 Grid Stencils for 5th Order Bandwidth-optimized WENO

Considering the positive flux, the four upwind-biased schemes on three candidates can be given as:

$$\begin{cases} h_{+0}' = \frac{1}{3}f_{j-2} - \frac{7}{6}f_{j-1} + \frac{11}{6}f_j \\ h_{+1}' = -\frac{1}{6}f_{j-1} + \frac{1}{3}f_j + \frac{5}{6}f_{j+1} \\ h_{+2}' = \frac{1}{3}f_j + \frac{5}{6}f_{j+1} - \frac{1}{6}f_{j+2} \\ h_{+3}' = \frac{11}{6}f_{j+1} - \frac{7}{6}f_{j+2} + \frac{1}{3}f_{j+3} \end{cases} \quad (3.11)$$

In the same way, we have,

$$h_{+Linear, j+\frac{1}{2}} = \alpha_0 h_{+0}' + \alpha_1 h_{+1}' + \alpha_2 h_{+2}' + \alpha_3 h_{+3}' \quad (3.12)$$

when the optimal order is realized, the α_i must be determined as:

$$(\alpha_0, \alpha_1, \alpha_2, \alpha_3) = (0.05, 0.45, 0.45, 0.01) \quad (3.13)$$

The final nonlinear weighted schemes can be expressed as:

$$h_{j+1/2}^+ = \omega_0 h_{j0}^+ + \omega_1 h_{j1}^+ + \omega_2 h_{j2}^+ + \omega_3 h_{j3}^+ \quad (3.14)$$

where

$$\omega_i = b_i / (b_0 + b_1 + b_2 + b_3) \quad (3.15)$$

$$b_i = \alpha_i / (\varepsilon + IS_i)^2 \quad (3.16)$$

IS_i has the following form:

$$\begin{cases} IS_0 = \frac{13}{12} (f_{j-2} - 2f_{j-1} + f_j)^2 + \frac{1}{4} (f_{j-2} - 4f_{j-1} + 3f_j)^2 \\ IS_1 = \frac{13}{12} (f_{j-1} - 2f_j + f_{j+1})^2 + \frac{1}{4} (f_{j-1} - f_{j+1})^2 \\ IS_2 = \frac{13}{12} (f_j - 2f_{j+1} + f_{j+2})^2 + \frac{1}{4} (3f_j - 4f_{j+1} + f_{j+2})^2 \\ IS_3 = \frac{13}{12} (f_{j+1} - 2f_{j+2} + f_{j+3})^2 + \frac{1}{4} (-5f_{j+1} + 8f_{j+2} - 3f_{j+3})^2 \end{cases} \quad (3.17)$$

In order to make the scheme stable, further modification is made as: $IS_3 = \max_{0 \leq k \leq 3} IS_k$.

Further improvement for ω_k by Martin et al is:

$$\omega_i = \begin{cases} \alpha_k & \text{if } \max(TV_k) / \min(TV_k) < 5 \text{ and } \max(TV_k) < 0.2 \\ \omega_i & \text{otherwise} \end{cases} \quad (3.18)$$

where TV_k stands for the total variation on each candidate stencil.

A large eddy simulation (LES) method is used by solving the unfiltered form of the Navier-Stokes equations with the 5th order bandwidth-optimized WENO scheme, which is generally referred to as implicitly implemented LES (ILES). Without explicitly using the subgrid scale (SGS) model as the explicit LES, the implicitly implemented LES uses the intrinsic dissipation of the numerical method to dissipate the turbulent energy accumulated at the unresolved scales with high wave numbers.

3.1.2 The Difference Scheme for the Viscous Terms

Considering the conservative form of the governing equations, a standard 4th order central difference scheme (Equation (3.19)) is used to discrete the 2nd order viscous.

$$\left(\frac{\partial u}{\partial x}\right)_i = \frac{-u_{i+2} + 8u_{i+1} - 8u_{i-1} + u_{i-2}}{12\Delta x} \quad (3.19)$$

3.1.3 The Temporal Scheme

The explicit third-order TVD-type Runge-Kutta [49] scheme was applied for temporal discretization. The scheme was implemented using eq.(3.20)

$$\begin{aligned} u^{(1)} &= u^n + \Delta t L(u^n) \\ u^{(2)} &= \frac{3}{4}u^n + \frac{1}{4}u^{(1)} + \frac{1}{4}\Delta t L(u^{(1)}) \\ u^{n+1} &= \frac{1}{3}u^n + \frac{2}{3}u^{(2)} + \frac{2}{3}\Delta t L(u^{(2)}) \end{aligned} \quad (3.20)$$

3.2 Grid Generation

In order to preserve the accuracy of the geometry to reduce numerical errors as much as possible while using 5th order bandwidth-optimized WENO scheme, the strategy of body-fitted grids is adopted. Results in later parts of the paper testify that such grid frame is very helpful to obtain the high resolution of the flow structure.

In this study, flows around MVGs are studied with back edge declining angle 70°. The geometry of MVG is shown in Fig. (3.3). The other geometric parameters in the figure are the same as those given by Babinsky⁶, i.e., $c=7.2h$, $\alpha=24^\circ$ and $s=7.5h$, where h is the height of MVG and s is the distance between the center lines of two adjacent MVGs. So the distance from the center line to the spanwise boundary of the computation domain is $3.75h$.

According to experiments by Babinsky [7], the ratio h/δ_0 of the models has the range from 0.3~1. The appropriate distance from the trailing-edge to the control area is around $19\sim 56h$ or $8\sim 19\delta_0$. In this study, the height of MVG h is assumed to be $\delta_0/2$ and the horizontal distance from the apex of MVG to the ramp corner is set to be $19.5h$ or $9.75\delta_0$. The distance

from the end of the ramp to the apex is $32.2896h$. The distance from the starting point of the domain to the apex of MVG is $17.7775h$. The height of the domain is from $10h$ to $15h$ while the width of the half domain is $3.75h$. The geometric relation of the half of the domain can be seen in Fig. 3.4, where the symmetrical plane is the centre plane.

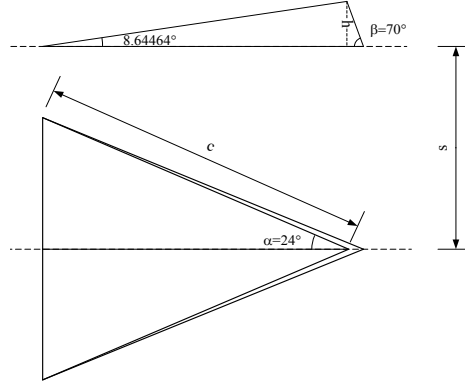


Figure 3.3 The Geometry of MVG

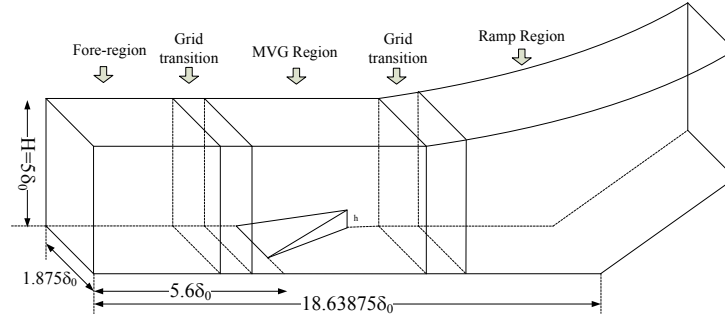


Figure 3.4 The Schematic of the Half Grid System

Because the singularity of the geometry, it is difficult to use one technique to generate the whole grid system. A general grid partition technique is used in this grid generation. As shown in Fig. 3.4, three regions are divided as: the ramp region, MVG region and fore-region. Between each two regions, there is a grid transition buffer. Because of the symmetry of the grid

distribution, only half of the grids need to be generated. The grid number for the whole system is: $n_{spanwise} \times n_{normal} \times n_{streamwise} = 128 \times 192 \times 1600$.

The grid generation includes two steps: first using analytical methods [22, 23] to generate the algebraic grids; next using elliptic grid generation equation to improve the orthogonal and smooth property of the grid.

The schematic figure can be shown in Fig. 3.5. The procedures for grid generation are: first generating the boundary grids of the lower and upper boundaries; next generating the inner grids by interpolation. Figure 3.6 shows the generated mesh with a grid interval of 8 in streamwise and of 6 in normal directions.

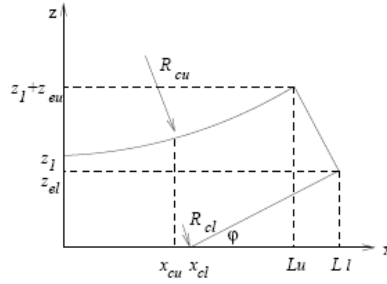


Figure 3.5 The Geometry Sketch of the Ramp

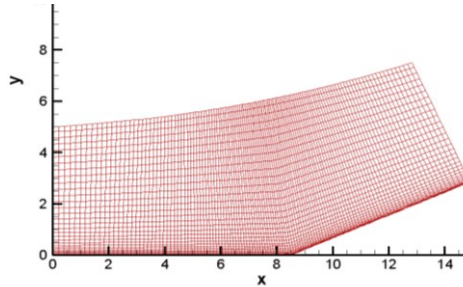


Figure 3.6 The Grid System of Case 1

Because of the specification of the boundary conditions on the body surface, an orthogonal grid is very important to ensure the high accuracy of the computation. This is particularly important to the case with complex geometry, where the zero normal gradient

condition is usually realized by using the derivative along the normal grid line. To make grids orthogonal and smooth, a grid solver was developed by the group of the second author based on Laplace equations and algebraic transformations (see Ref. 50).

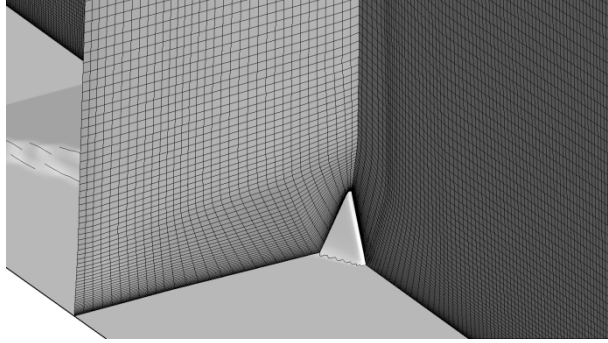


Figure 3.7 The Local View of Grids around the Trailing-edge

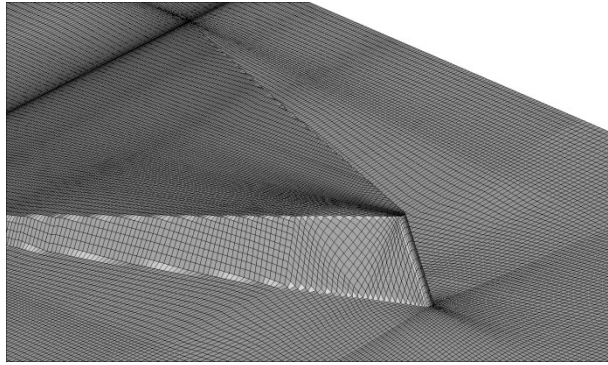


Figure 3.8 The Surface Grids of MVG

In order to generate the complete grids of MVG, it is essential to generate the surface grids. According to our experience, the quality of the surface grids will directly influence the quality of the 3-D volume grids, and the accurate description of the geometry by the surface grids can enhance the accuracy of the computation. Because the surface of MVG is of high singularity, it failed to use the automatic grid generation technique like projection by some commercial software. In this study, some manual work had to be done by the following steps: first a modification is made by smoothing the trailing-edge using a very small arc (Fig. 3.7); next the surface is divided into many small patches so that the singularity of the shape is reduced in each patch; thirdly, the skeleton grid lines are constructed manually in the patch using some

grid generation software in an interactive manner. Afterwards the lines are discretized into grid points. Careful adjustments are made to make the distribution of grids as smooth as possible; Finally, optimizations are made to let grid lines transit fluently between patches. The final surface grids can be seen in Fig. 3.8.

The detailed final grids can be seen in Fig. 3.9-3.11. Also given is the geometric parameters in Table 3.1. More details can also be found in Ref. [51].

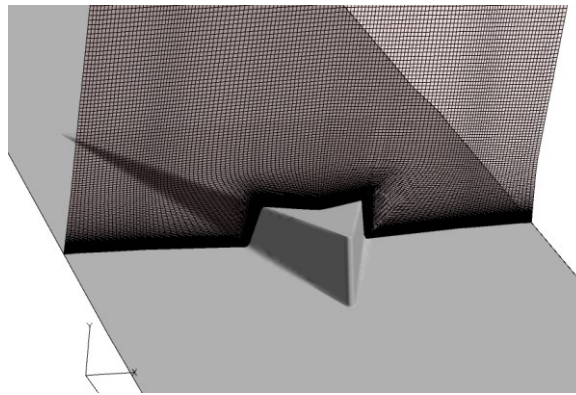


Figure 3.9 The Grids in Certain Cross-section

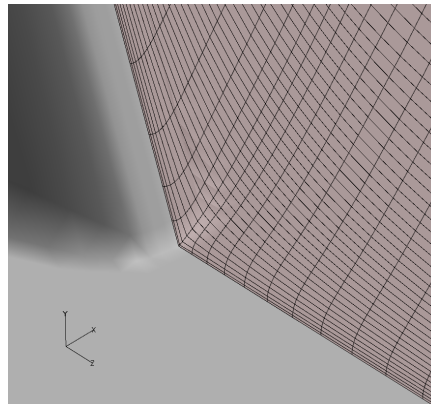


Figure 3.10 The Grids at the Foot of the Trailing-edge

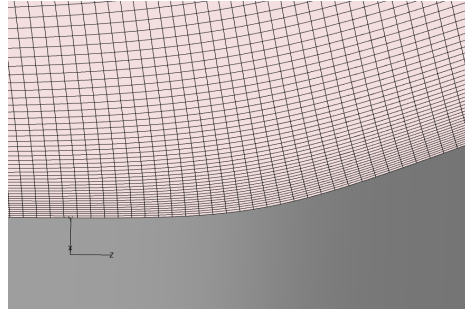


Figure 3.11 The Grids at the Ramp Corner

Table 3.1 The Geometric Parameters for the Computation

L_x	L_y	L_z	Δx^+	Δy^+	Δz^+
$3.75\delta_0$	$5-7.5\delta_0$	$25.03\delta_0$	26.22	1.36-38.38	12.79

3.3 Boundary Conditions

The adiabatic, zero-gradient of pressure and non-slipping conditions are used for the wall as:

$$\partial T / \partial n = 0, \quad \partial p / \partial n = 0, \quad U = 0 \quad (3.21)$$

The non-reflecting boundary conditions are applied for far field and periodic boundary conditions are adopted in the spanwise direction. No visible artificial reflections are observed by the shock waves.

It is a challenging topic about how to get fully developed turbulent inflow comparable to the experimental conditions. There is a large body of published work on generating turbulent inflow boundary condition for simulation of complex spatially developing external flows; the most representative paper is perhaps that of Lund, Wu & Squires (1998). Lund et al [52]. (1998) developed a simplified version of the Spalart method by invoking only the transformation on independent variables at two streamwise stations without altering the Navier-Stokes equations. This method and its subsequent variations have been shown to yield reasonable inflow conditions for complex, spatially developed flows because quite often the downstream pressure

gradients and geometrical variations mask any major defects of the inflow. However, because of their semi-empirical nature, even with DNS resolution, it would be quite challenging for these methods to generate results that can be considered as experimental data quality for the turbulent boundary layer. Therefore, in present work, the turbulent mean profile and velocity fluctuations have been obtained from a separate DNS computation of compressible turbulent boundary layer.

In order to guarantee a fully developed turbulent flow, the inflow condition were treated with two parts, the mean component and the fluctuation component. The averaged boundary layer profile from the DNS result[62] was implemented into current grid system through third-order spline interpolation. The transplant was carried out by assuming the non-dimensional velocity u/U_∞ scales with y/δ^* .

The temperature profile at inlet was determined by eq.(3.22),

$$\frac{T}{T_\infty} = \frac{T_w}{T_\infty} - \frac{r}{2}(\gamma - 1)Ma_\infty^2 \left(\frac{u}{U_\infty} \right)^2 \quad (3.22)$$

where r is the recovery factor with value $r=0.9$ and the adiabatic wall temperature was determined by eq.(3.23),

$$\frac{T_w}{T_\infty} = 1 + \frac{r}{2}(\gamma - 1)Ma_\infty^2 \quad (3.24)$$

Pressure p was set uniform at inlet and density ρ was calculated by eq.(3.24)

$$\rho = \frac{p}{RT} \quad (3.25)$$

Fluctuation components of velocity were also acquired from DNS[62] and form an input dataset of 20,000 fluctuation profiles. They were later added into the averaged profile according to different time steps. By performing derivative to eq.(3.22), the temperature fluctuation can be approximated through eq.(3.26)

$$\frac{\Delta T}{T_\infty} = -r(\gamma - 1)Ma_\infty^2 \frac{u}{U_\infty} \Delta u \quad (3.26)$$

The density fluctuation was then calculated by eq.(3.27)

$$\frac{\Delta \rho}{\rho_{\infty}} = \frac{\Delta T}{T_{\infty}} \quad (3.27)$$

The mean data and the fluctuation data were finally summed up and implemented as the inlet boundary condition.

3.4 Code Validation

Because the 5th order bandwidth-optimized WENO scheme is a quite mature method and the problem studied in this paper contains shock waves, a supersonic inviscid flow around the half cylinder at $M_{\infty} = 4$ was selected as the validating test. The test can demonstrate the scheme's ability for shock capturing and confirm the correctness of the code system. Fig. 3.12 shows the isobar contour in the middle section in the spanwise direction, which indicates that the scheme can capture shock waves with essentially free of oscillations.

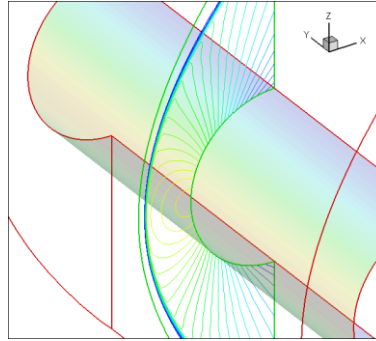


Figure 3.12 The Contour of the Pressure

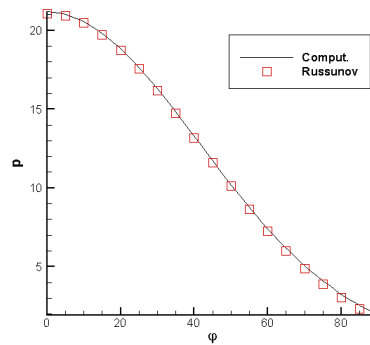


Figure 3.13 The Comparison of the Pressure

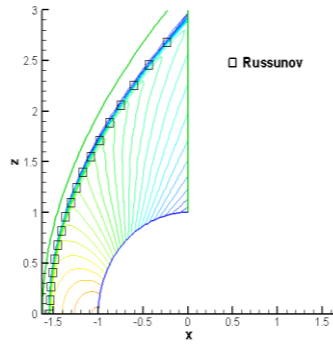


Figure 3.14 The Comparison of the Shock Location with that of Rusunov

Fig. 3.13 and 3.14 show the comparison between the numerical results and the asymptotic solution from Rusunov, which is usually considered as the “theoretical” solution of that problem. A good agreement is obtained between the two results. The convergence rate in Fig. 3.15 shows a reduction of about 6 orders of the residual was obtained.

Additional computations were made by rotating the curvilinear coordinates system alternatively to make the problem three-dimensional. The results prove the correctness of the current codes.

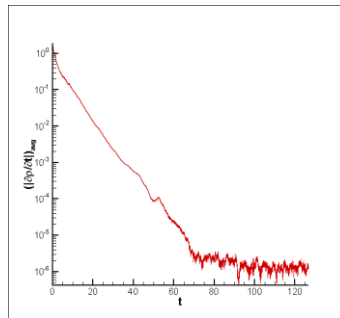


Figure 3.15 The Converging History of the 5th WENO Scheme

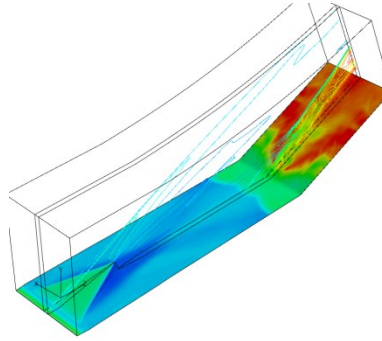


Figure 3.16 The Pressure Contour at the Central Plane and Body Surface

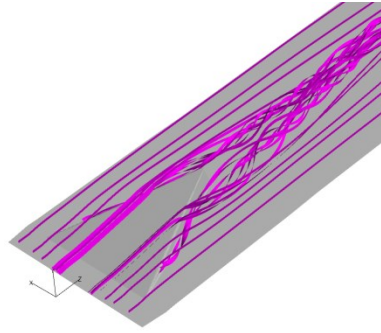
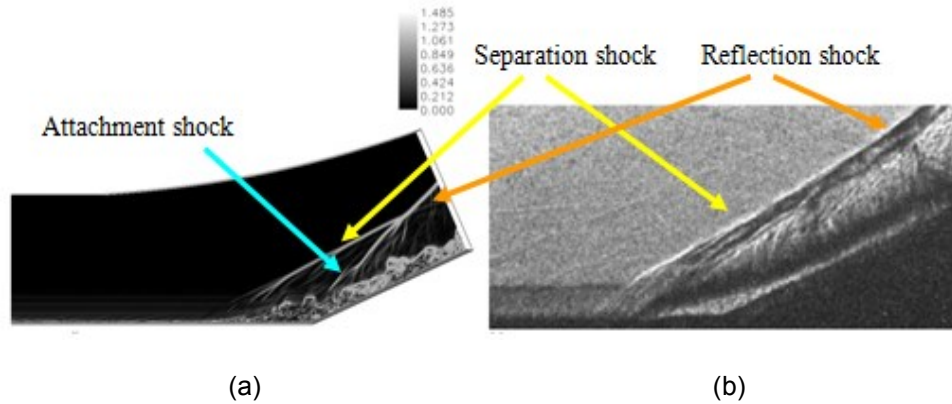


Figure 3.17 The Spatial Streamlines

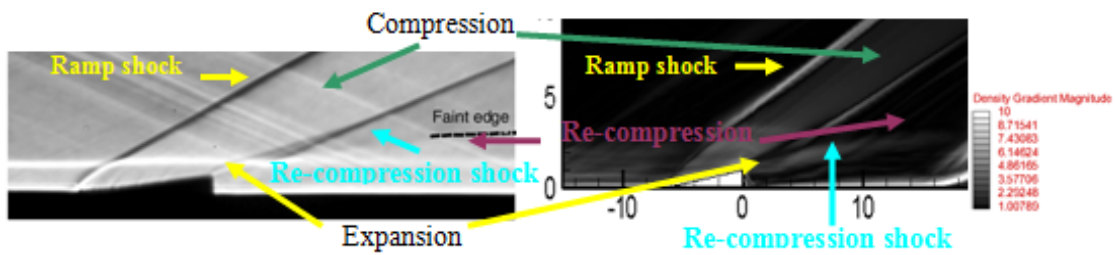
Another small case is set up for computation on a MVG controlling laminar ramp flow with $M = 3$ and $Re_\delta = 4800$, where a very coarse grid number was selected as $n_{streamwise} \times n_{normal} \times n_{spanwise} = 420 \times 121 \times 64$. The purpose of that test is to check if the computation can qualitatively capture the main flow structures of the problem. It can be found in Fig. 3.16 that the main shock and expansion waves are captured by the simulation; the reflecting shock wave generated by ramp is clearly distinguished as well. There is a hint about the possible re-compression shock wave. The pair of primary counter-rotating streamwise vortices is visualized by streamlines in Fig. 3.17. The preliminary results show that the main flow structures qualitatively agree with the results by Babinsky [7]. So this means the primary structures are captured and correctly described by the computation qualitatively, although there are few small scaled structures lost due to the reason that the grids are too coarse. The code system can be

used for the subsequent LES with much more grids. The validation made here is just for evidence that our LES code and scheme are correct for the Euler solver. The further validation for SBLI is made for a compression corner by comparing our LES results and experimental results [7,17] (see Figures 3.18 and Figures 3.19). We believe it is better to compare our LES results with experiment for the validation purpose.



(a) The Instantaneous Digital Schlieren at Central Plane (ramp angle is 24 degree) and
(b) The Schlieren Pictures from the Experiment (ramp angle is 25 degree)

Figure 3.18 Comparison of Flow Structures at Ramp



(a) The Schlieren Picture from Babinsky (b) Numerical Schlieren Picture at Central Plane

Figure 3.19 Comparison of Flow Structures after MVG

Chapter 4

NUMERICAL LES AND ANALYSIS OF VORTEX STRUCTURE BEHIND SUPERSONIC MVG

4.1 Inflow Boundary Layer Profiles

The inflow profiles are checked ahead of the MVG after long periods of computation. In order to define a reference coordinate system in this and following sections, the apex of the MVG is selected as the original point. The section for checking is located at 11.97h from the inlet in the streamwise direction. At this section, the Pitot pressure recovery coefficient and incompressible shape factor H_i are calculated and averaged in the spanwise direction. The Pitot pressure recovery coefficient used in this work is defined as:

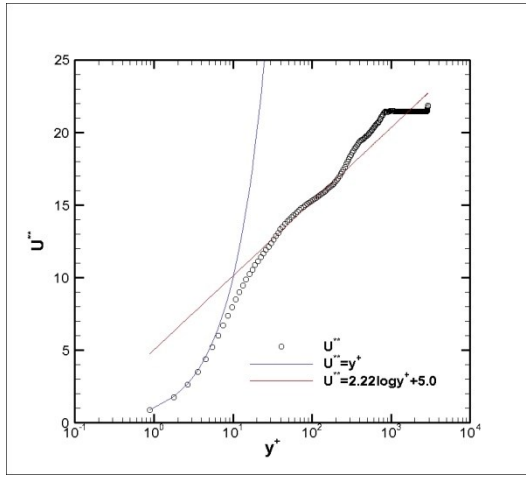
$$C_{P_{tot_{rc}}} = (1/H) \int_0^H (p_0 / p_{0\infty}) dy \quad (4.1)$$

where H can be a value approximately as the height of the domain. The definitions of displacement thickness (δ^*) and momentum thickness (θ) are given as:

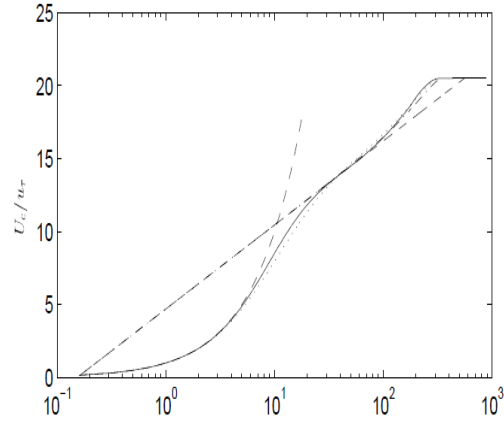
$$\left\{ \begin{array}{l} \delta^* = \int_0^H (1 - U / U_\infty) dy \\ \theta = \int_0^H (U / U_\infty) (1 - U / U_\infty) dy \end{array} \right. \quad (4.2)$$

Here, the averaged $C_{P_{tot_{rc}}}$ is 0.9912, and the averaged $H_i = \delta^* / \theta = 1.35$. As well known, the H_i for the laminar flow is around 2.6 and for the standard turbulent flow is about 1.2~1.4. So, the results indicate that the methods described in Chapter 3 produce a fully developed turbulent inflow.

Fig. 4.1 shows the inflow boundary layer velocity profile in log - coordinates. There is a well-defined log region and the agreement with the analytical profile is well throughout. These results are typical for a naturally grown turbulent boundary layer in equilibrium (see Guarini [54] et al).



(a)



(b)

(a) Inflow Velocity Profile by Our Computation

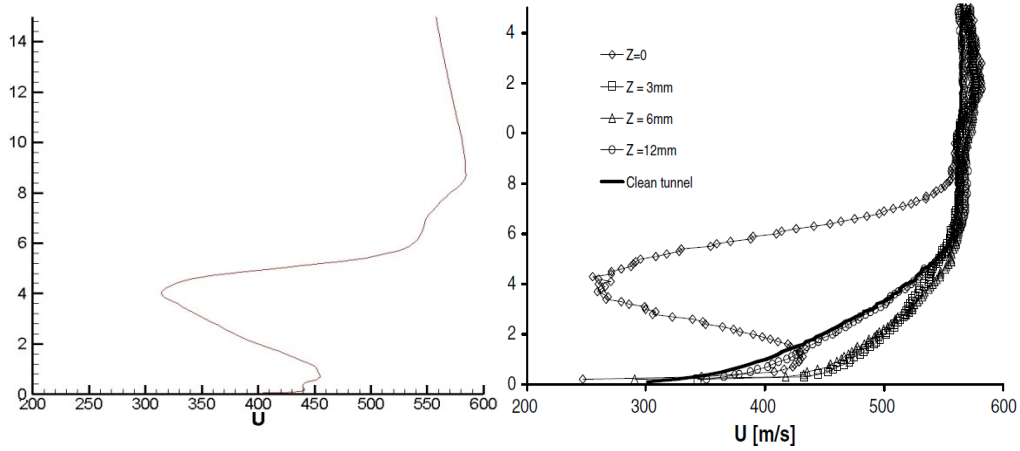
(b) Inflow Velocity Profile by Guarini [54] ($U^{**} = 2.5 \log y^{+} + 4.7$)

Figure 4.1 Inflow Boundary-layer Profile Comparison with GUARINI et al's

4.2 Results of the MVG Controlled Ramp Flow - Vortex Rings

4.2.1 Velocity Profile Behind MVG

Fig. 4.2 gives a qualitative comparison with experiment (Babinsky et al [7], 2009) in the time and spanwise averaged velocity profile behind MVG. In this study, numerical simulations are made with $M=2.5$ and $Re_{\theta}=5760$, but the experiment of Babinsky has a much larger Re_{θ} , i.e., about 28800. So the comparison between the computation and experiment in this paper should mainly be qualitative and agreement is achieved.



(a) Averaged Velocity Profile behind MVG (b) Averaged Velocity Profile by Babinsky et al

Figure 4.2 Qualitative Comparison of Averaged Velocity Profile behind MVG

4.2.2 The New Dynamic Vortex Model

According to results of the present investigation, a dynamic vortex model can be given in Fig.4.3 (half domain). The dominant vortex near the MVG is the primary vortex; underneath there are two first secondary counter-rotating vortices, which later leave the body surface and become fully 3D separations by the way of spiral points in body surface. These vortices will merge into the primary vortex propagating downstream, while new secondary vortices will be generated under the primary vortex. This dynamic vortex model is confirmed recently by Mohd R. Saad et al[63] in their experiment work (Figure 4.4) and work of UT Arlington in the experiment at the same Mach number [56,68] (Figure 4.5). The spiral points are also confirmed by both experiments.

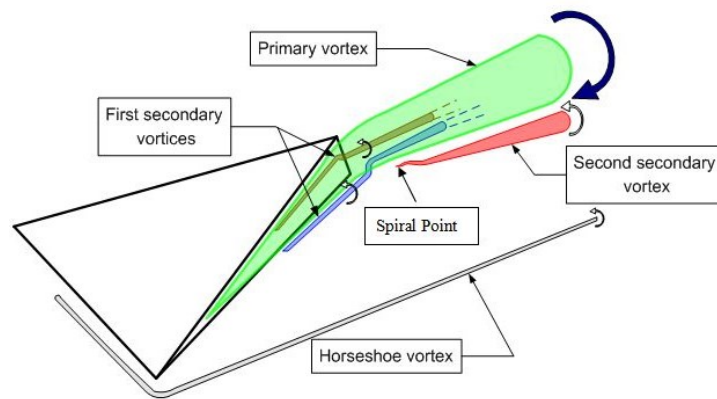


Figure 4.3 The dynamic vortex model (Li and Liu[37])

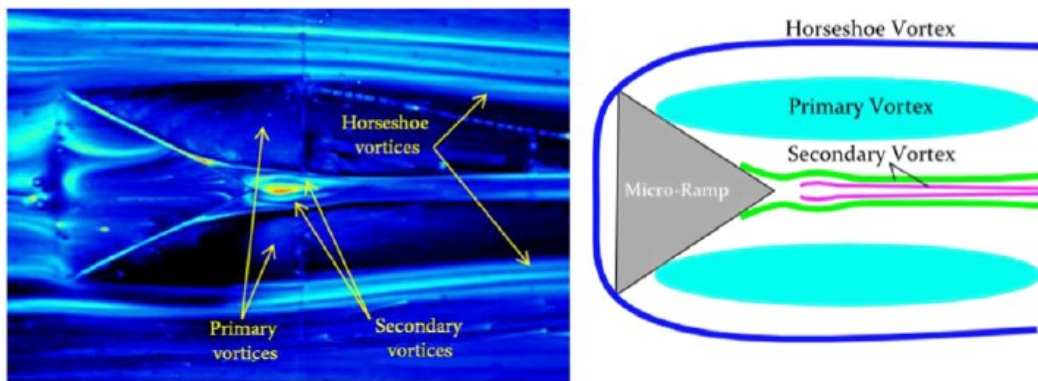


Figure 4.4 Surface flow visualization image and the vortex model given by
Mohd R. Saad et al [63]

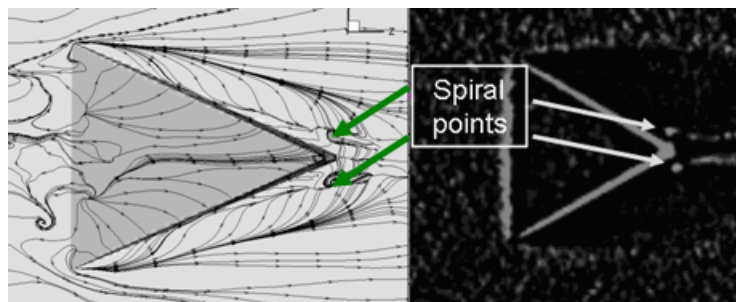


Figure 4.5 The Comparison between Computation and the Experiment of Lu[56]

4.2.3. Vortex Rings - A New Mechanism in MVG-ramp Flow Control

According to the up-to-date knowledge from the experiment and computation, a pair of primary counter-rotating streamwise vortices and the underneath attached secondary ones are considered to be the mechanism of the flow control. The primary vortices will bring about high speed momentum entrainment to the location near to the floor [64], which is favorable to resistance of the adverse gradient of the pressure. According to our computation and the results from other authors [8], the rotation of the streamwise vortices becomes weak quickly (see Fig. 4.6) and streamlines oscillate in the space due to the shear layer instability around the momentum deficit circle. It suggests that there might be some other mechanism in the MVG controlled flow, besides the only pair of streamwise vortex tubes to cause the momentum exchange.

Because the vortex axis is usually the location with the minimum pressure, the iso-surface of pressure is an easy tool to visualize the vortex tube. In Fig. 4.7, we draw the iso-surface of pressure using the same instantaneous data as that of Fig. 4.6. Besides the expansion wave and the surface wrapping the tube near the trailing-edge, the ring-like structures are found in the subsequent downstream region. Such rings appear initially not far away from the trailing-edge, and become larger and irregular when moving downstream; in the meanwhile the streamwise vortex tubes become weaker and less observable at certain locations.

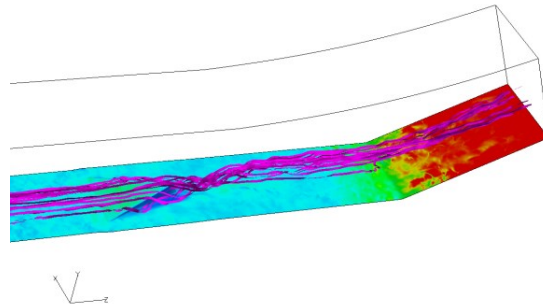


Figure 4.6 The Instantaneous Spatial Streamlines

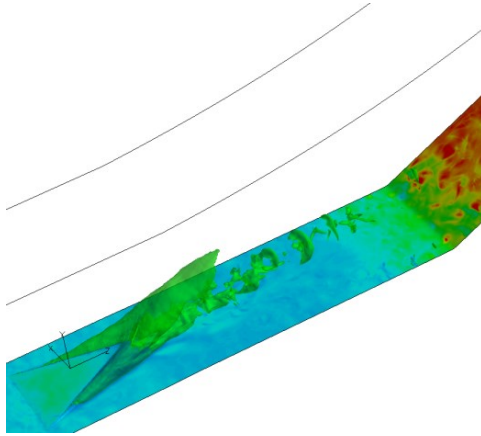


Figure 4.7 The Iso-surface of the Instantaneous Pressure

4.2.4 Analysis of The Structure of Vortex Rings

To reveal the coherent structure of the flow, the iso-surface of λ_2 scalar field [55] is used (figure 4.8). A small negative value is selected for visualization. It is very clear that there is a chain of vortex rings, starting from behind of the trailing-edge of MVG. The rings are generated almost erectly (normal to the wall) at first and then they are continuously distorted and enlarged while propagating downstream. These rings could be a dominant factor of the mechanisms of MVG in control of shock boundary layer interaction.

The well-shaped rings are approximately perpendicular to the flat plate, and then begin to deform while propagating downstream. The lower part of the ring first hits the shock and the speed decelerates. Then the upper part of the ring hits the shock. So the vortex rings on the ramp appear in an oblique posture. The rings maintain their existence until flowing out of the domain.

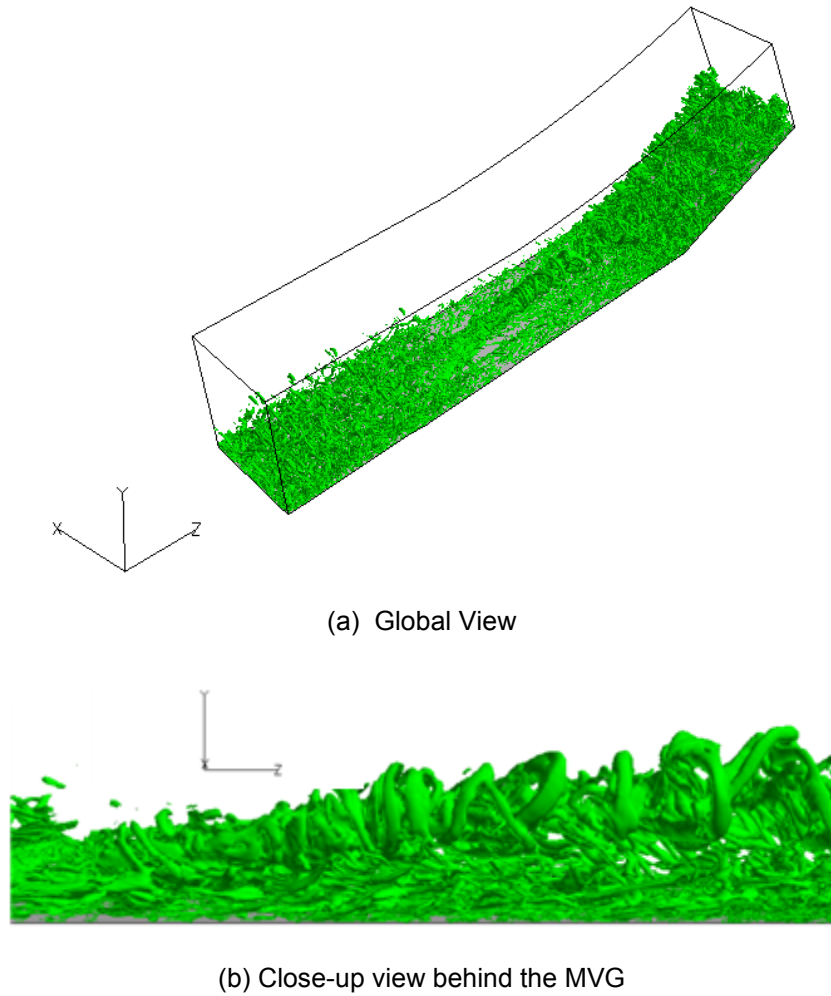


Figure 4.8 Vortex rings shown by iso-surface of λ_2

Fig. 4.9 demonstrates the instantaneous numerical schlieren at the central plane. We can see many vortex rings appear in circular shapes. Informed with the prediction of vortex rings, the experimentalists in UT Arlington used some technology to validate the discovery. They used the particle image velocimetry (PIV) and the acetone vapor screen visualization to track the movement of the flow. More specifically, the flash of a laser sheet is used to provide the light exposure at a time interval of micro seconds. Fig. 4.10 presents a typical image at the center plane using PIV and the acetone vapor technology(Lu et al [47]). It is clearly demonstrated that a chain of vortex rings exists in the flow field after the MVG, same as shown in LES results (see Fig. 4.9).

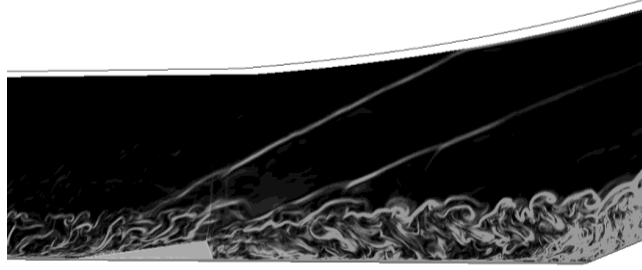
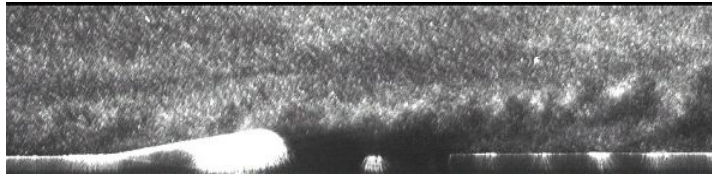
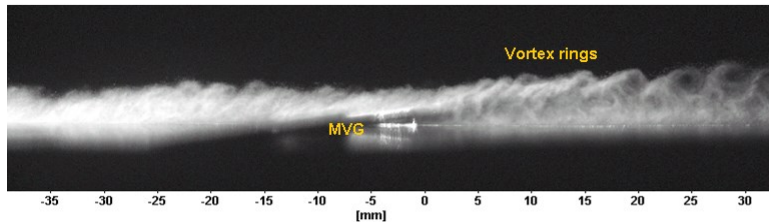


Figure 4.9 The Numerical Shilieren at the Center Plane[51]



(a) Using PIV



(b) Using the Acetone Vapor

Figure 4.10 The Laser-sheet Flash Image at the Center Plane (Lu et al 2010)

Our numerical discoveries of the vortex ring structures are also confirmed by 3-D PIV experiment (Fig. 4.11) conducted by Sun et al at Delft University [33,69]. Compared the two results, we can find the similar distribution of streamwise (ω_z) and spanwise vorticity (ω_x) components, which also proves the existence of ring structures. The Kevin-Helmholtz vortices part in Fig. 4.12 corresponds with the ring head in Fig. 4.8. The underneath part which is illustrated as streamwise vortices are two counter rotating primary vortices which are considered to be the main source of the ring structure as explained later .

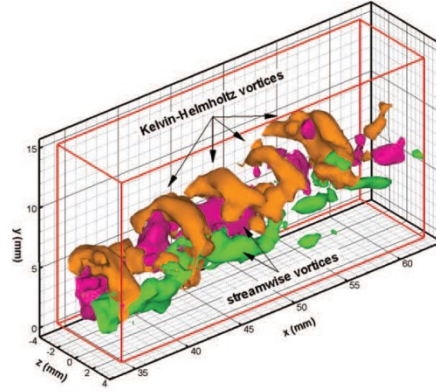


Figure 4.11 K-H rings behind MVG by (Sun et al 2011)

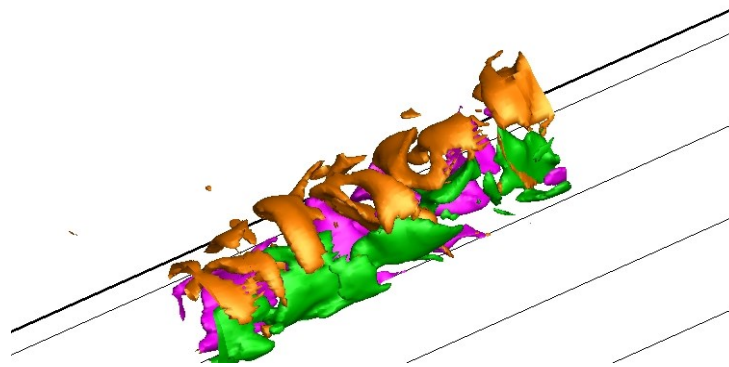
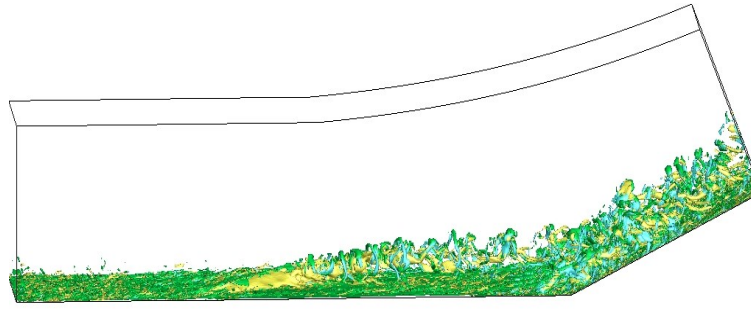
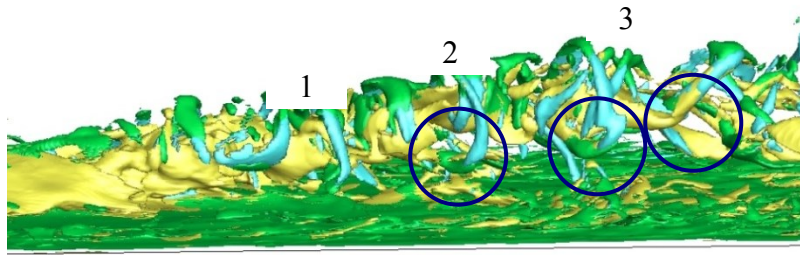


Figure 4.12 Distribution of K-H Vortices and Streamwise Vortices from LES[58]

The vorticity component which revolves towards the vertical direction (ω_y in our case) is not shown in Fig. 4.11 and 4.12. If this missing part was provided, we can see the vortex ring structure clearly by the combination of all the components of vorticity as shown in Fig. 4.13 which is in accordance with the structure in Fig. 4.8.



(a) Global view



(b) Close-up View

Figure 4.13 Vortex Rings shown by the Components of Vorticity[58]

According to further analysis, we find that the ring structure is mainly composed by ω_x and ω_y , while the streamwise vorticity component ω_z is absolutely the major source of two counter-rotating primary vortex inside the ring structure. ω_x constitutes the head and part of the bottom of the rings and ω_y forms the two sides. Also, the ring structure is not the perfect one since it is not closed on the bottom, instead, the two feet of each ring penetrate inside and connect with the inner primary vortices, as shown inside the circles in Fig. 4.13. In Fig. 4.14, the ring structure is clearly illustrated by both the total vorticity magnitude and each vorticity components. Actually, the vortex tube of each ring changes its direction and is connected to the two streamwise primary vortices inside at the foot part which is clearly shown in Fig. 15. Once the ring is generated, it will never break up into pieces or separated parts and disconnect from the main vortex structure.

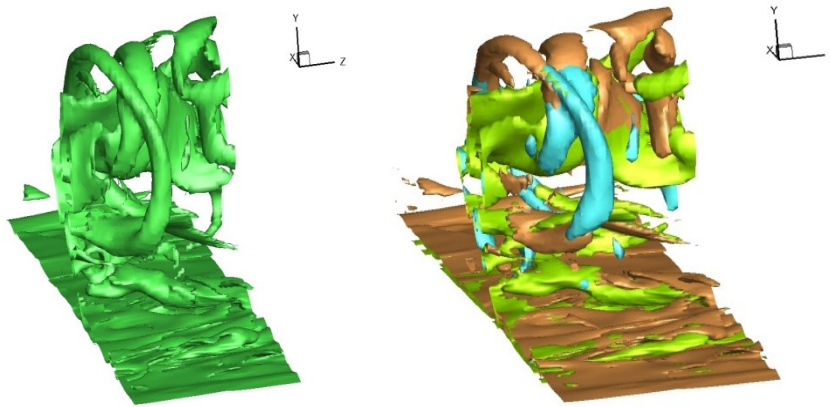


Figure 4.14 Part of the Ring Structure shown by Total Vorticity Magnitude (left) and each Components (right)[58]

To further support the conclusion that the ring structure never breaks up and each ring has the feet connected inside, a close-up bottom view of vortex structure illustrated by λ_2 is given in Fig. 4.15 by another transient data set at different time and different location. Here, only half of the spanwise domain is used to make the vortex structure more clear. The iso-surface of λ_2 can show the vortex tubes accurately and it captures two adjacent vortex rings in Fig. 4.15, and it apparently visualized the vortex tubes connect to the ring feet inside the vortex structure.

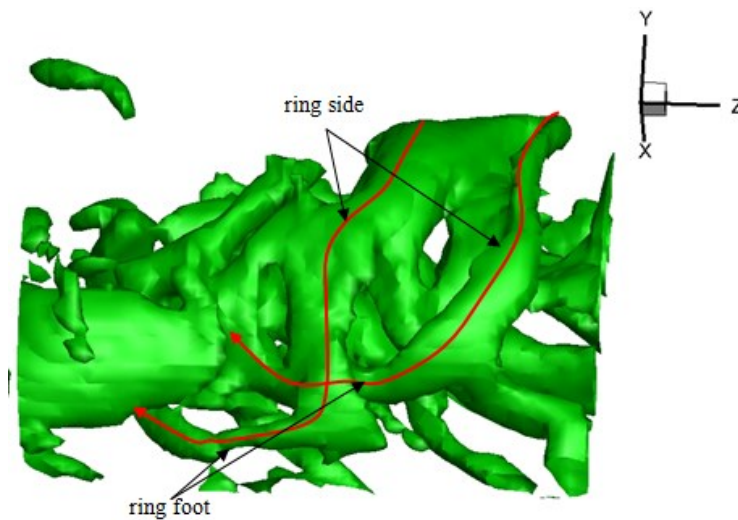


Figure 4.15 Part of the Ring Structure shown by λ_2 (from the bottom view)[58]

From the analysis of the magnitude of each vorticity component, ω_x and ω_z play the leading role during the process of propagating downstream. ω_x mainly originates from the shredding of the upstream MVG boundary layer, however, the other two components which forms the ring structure are separated from the viscous sub-layer underneath after about 1.1h away from the trailing edge of the MVG downstream. They are very likely following the vorticity conversion of the streamwise part. During the propagating, ω_x is reduced gradually and the rings are extended. In the end of the evolution, the momentum deficit (caused by streamwise vortex) disappears and the ring structure is totally distorted.

Fig. 4.16 shows the velocity field on a cross section in which it is found that the low speed flow from the viscous sub-layer is inhaled into the momentum deficit area continuously as a result of two counter rotating streamwise vortices inside the rings. This may explain why the momentum deficit area can survive such a long way and determines the development of the ring structure. Fig. 4.17 is the flow field close to the foot and the head of a vortex ring which shows the vortex ring is extended outside by the velocity field around it, and that velocity field also helps the conversion between the components of vorticity.

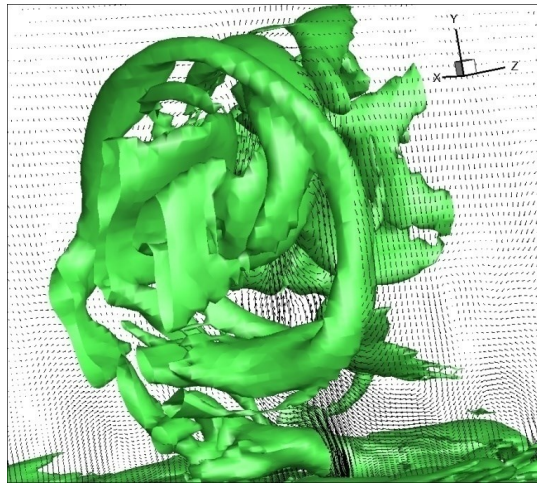


Figure 4.16 The Velocity Field on the Cross Section[58]

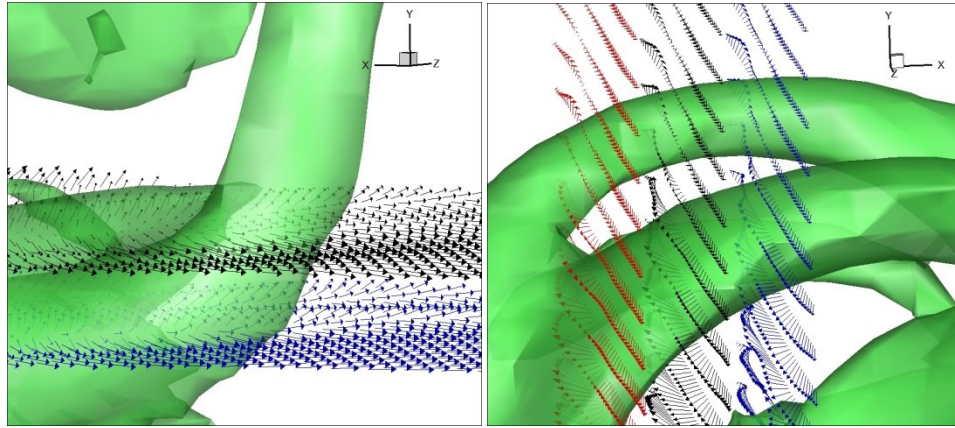


Figure 4.17 The Velocity Field close to the Foot (left) and the Head (right) of a Vortex Ring[58]

4.2.5 Conservation of Vorticity

Because the original streamwise vortices and new generated vortex rings are both located away from viscous sub-layer for some distance, new vorticity in K-H vortex rings can only be transported to from the primary streamwise vortices if the distance is not far away from the MVG. The conservation of vorticity should make the vortices closely related to each other. The vorticity of the shear layer which results in the generation of the vortex rings should be transported from the original streamwise vortices. In order to investigate the relationship among the vortices, we measured the distribution of the maximum value of both streamwise and spanwise vorticity in a specific region (as seen in Fig. 4.18) to avoid the possible affection from the viscous sub-layer.

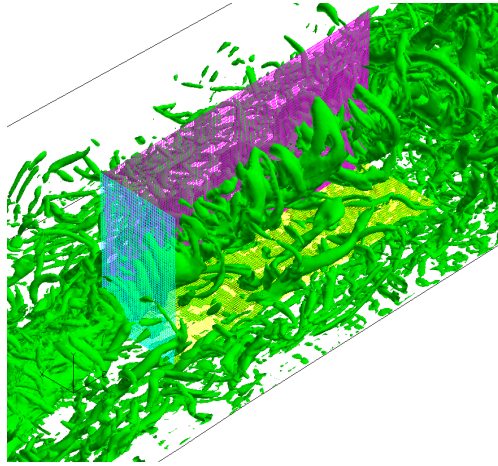


Figure 4.18 The Scope for Vorticity Magnitude Check

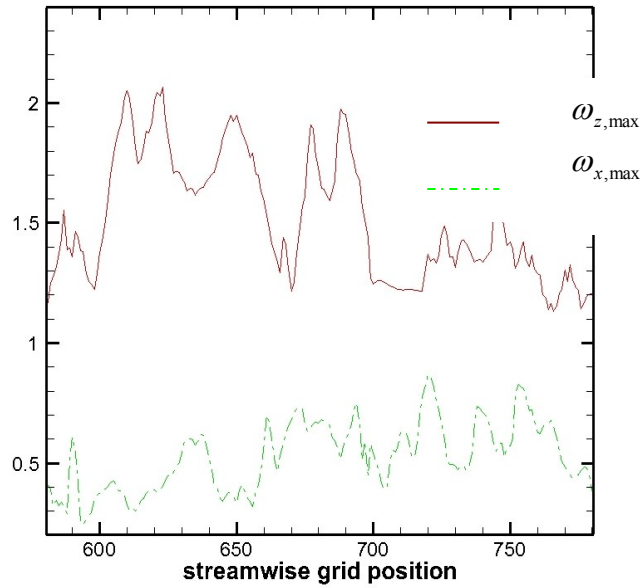


Figure 4.19 The Instantaneous Vorticity Distribution(Y Yan et al)

Considering the pair of streamwise vortices are counter-rotating and vortex rings intersect the center plane in two locations, we only took the right half part and used positive values in Fig. 4.19. Since the grids are not uniform, it is more convenient to use streamwise grid position to mark the positions which range from about 1.0h to 9.5h after the trailing edge of MVG. Fig. 4.19 gives the instantaneous distribution of the two quantities along streamwise position of grids.

From the figure and analysis of the flow field, the following results can be obtained:

1. The locations of the peaks of $\omega_{x,max}$ represent the upper intersection of the K-H vortex rings and the center plane. The positions of those peaks are nearly the same as the locations of the upper cores of new generated K-H vortex ring tubes which means the maximum value of spanwise vorticity happens on the ring head and at the central spanwise plane.

2. The quantities of $\omega_{x,max}$ and $\omega_{z,max}$ both substantially oscillate along the streamwise direction. The change of $\omega_{z,max}$ is relatively greater, while the quantity of the spanwise vorticity between the vortex rings appears relatively smaller. This is normal since the two counter rotating streamwise vortices are the main structure and almost only the streamwise vorticity is generated by MVG at very beginning.

3. There are two stages of the evolution of the vorticity, which reflect the interaction or coupling between the streamwise vorticity and vortex rings:

The first stage is the coupling stage from the beginning to about 700 ($z \approx 5h$ after the trailing edge of MVG). In this stage, not only the falling down of $\omega_{x,max}$ corresponds to the peaks of $\omega_{z,max}$, they also oscillate in the opposite directions. This is reasonable because in this period, the vortex rings, which are just generated, must obtain the vorticity from the primary streamwise vortex due to the vorticity conservation law.

The second stage, the post-coupling stage, starts from 700 to the end of box. In this stage, the momentum deficit area begins to disappear but the two curves still oscillate asynchronously. The interaction between streamwise and spanwise vorticity of course still exists, the quantity of the $\omega_{x,max}$ is reduced and the frequency of the oscillation is also increased. However, they are not directly against each other. This is because each new generated K-H vortex ring is stretching and developing individually. They are no longer aligned with the root on the vortex ring bottom.

The variation of the quantity of streamwise and spanwise vorticity confirms that vorticity of the rings comes from the streamwise vortex structure inside the momentum deficit. Without

enough complement of vorticity from the subviscous layer underneath, new generated spanwise vorticity can only be transported from the primary streamwise vorticity. Also, at the very beginning part of the first stage, when the vortex structure is not separated from the subviscous layer absolutely, the variation of the two vorticity components keeps the same rule. This declares that the conservation of vorticity plays the leading law during the whole process of the ring structure generation.

4.3 Stability Analysis to the Velocity Profile

In order to explore the mechanism of the vortex ring generation, the distributions of time and spanwise averaged streamwise-velocity are given in Fig. 4.20 along the normal grid lines at the central plane. The streamwise positions of the lines are $L_{\text{from apex}}/h \approx 3.3, 6.7, 10$ and 11 , where $L_{\text{from apex}}$ is the streamwise distance measured from the apex of MVG. The dip of the lines corresponds to the momentum deficit. From the results, it can be seen clearly that there are at least two high shear layers in the central plane, one is located at the upper edge of the dip and the other is located at the lower edge. Within the shear layer, there is at least one inflection point. In order to demonstrate the existence of the inflection points, the second order derivative $\partial^2 w / \partial y^2$ (w is the streamwise velocity and y is the normal direction) is calculated along the lines, and the result of the line at $L_{\text{from apex}}/h \approx 3.3$ is plotted in Fig. 4.21 as an example. The existence and correspondence of the inflection points at the upper and lower shear layers is clearly illustrated as follow.

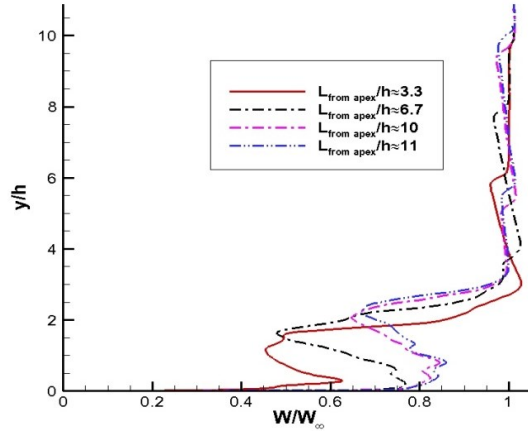
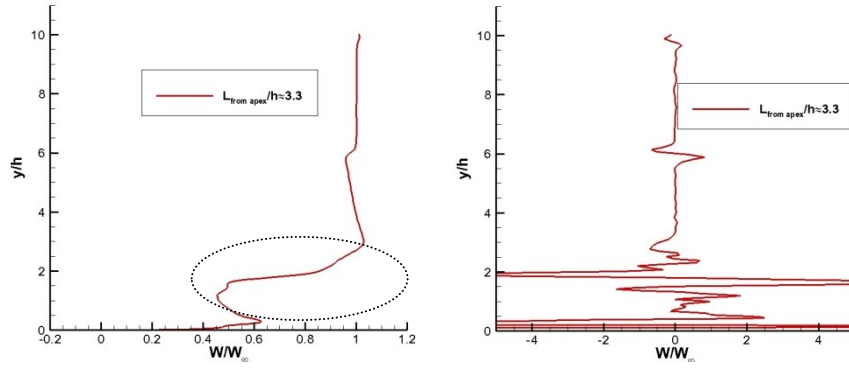


Figure 4.20 Averaged Streamwise Velocity at Different Sections



(a) Averaged Streamwise Velocity at $L_{\text{from apex}}/h \approx 3.3$ (b) $\partial^2 w / \partial y^2$ at $L_{\text{from apex}}/h \approx 3.3$

Figure 4.21 Inflection Points (surface for 3-D)

It is obvious that the existence of the inflection point in shear layer will cause the flow losing the stability and generate vortex rollers by the Kelvin-Helmholtz instability (K-H) theory. So the mechanism for the vortex ring generation is a result caused by the K-H type instability, and the lost of the stability of the shear layer results in the roll-up of the vortex rings. In order to explore the mechanism of the vortex ring generation with viscous fluid, it is necessary to make analysis about stability upon the velocity profile.

4.3.1 Derivation of Linear Stability Equation

As discussed below, a linear stability analysis based on incompressible but viscous flow is conducted as following. First, the velocity profile of the upper boundary of the momentum deficit area (circled in Fig. 4.21a) is taken to study since the intensity of the upper shear layer appears to be stronger than that of the lower shear layer (Fig. 4.21a). If we can prove that, even for this temporal and spanwise averaged velocity profile, the flow is instable, and then the instantaneous velocity distribution should be unconditional instable.

$$\begin{cases} \frac{\partial V}{\partial t} + V \cdot \nabla V = -\nabla p + \frac{1}{\text{Re}} \nabla^2 V \\ \nabla \cdot V = 0 \end{cases} \quad (4.3)$$

Equation (4.3) denotes the incompressible and non-dimensional Navier-Stokes equation in which, $V = (u, v, w)$ is the velocity vector. Considering that

$$q(x, y, t) = q_0(y) + q'(x, y, t) \quad (4.4)$$

where q can be specified as (u, v, w, p) , $q_0 = (u_0, v_0, w_0, P_0)$ which indicates the value of mean flow, and q' denotes the corresponding linear perturbation. By eliminating the second order perturbation terms, the governing equation for small perturbations can be written as,

$$\begin{aligned} \frac{\partial V'}{\partial t} + (V_0 \cdot \nabla)V' + (V' \cdot \nabla)V_0 + \nabla p' &= \nabla^2 V' / \text{Re} \\ \nabla \cdot V' &= 0 \end{aligned} \quad (4.5)$$

As a first step, a localized 2-D incompressible temporal stability for shear layer is conducted. Actually, it relates to the distance among two neighboring vortices in the central streamwise plane. Assume the normal mode is

$$\begin{aligned} V &= \hat{V}(y)e^{i(\alpha x + \beta z - \omega t)} + c.c. \\ p &= \hat{p}(y)e^{i(\alpha x + \beta z - \omega t)} + c.c. \end{aligned} \quad (4.6)$$

where the parameter α is given, which is real and set to be 0.5 according to the averaged distance between the new generated rings, and c should be a complex number. By plugging in Equation (4.6), Equation (4.4) can be rewritten as,

$$\begin{aligned} L\hat{u} &= \text{Re}(Du_0)\hat{v} + i\alpha \text{Re} \hat{p} \\ L\hat{v} &= \text{Re}(D\hat{p}) \\ L\hat{w} &= i\beta \text{Re} \hat{p} \\ i(\alpha\hat{u} + \beta\hat{w}) + D\hat{v} &= 0 \end{aligned} \tag{4.7}$$

where $L = \{D^2 - (\alpha^2 + \beta^2) - i\text{Re}(\alpha u_0 - \omega)\}$, and $D = \frac{d}{dr}$

Considering in 2D case (without w), and by eliminating \hat{u}, \hat{p} , we can obtain the standard O-S equation on \hat{v} ,

$$(D^2 - \alpha^2)^2 \hat{v} - i\alpha \text{Re}[(U_0 - c)(D^2 - \alpha^2) - D^2 U_0] \hat{v} = 0 \tag{4.8}$$

Equation (4.8) is about \hat{v} , but we need to get the value of c . The value of c determines the property of stability of the equation. Let $c = c_r + ic_i$, if $c_i > 0$, then the disturbance will continuously grow and the flow would be instable. Otherwise, the flow would be stable.

4.3.2 Stability Analysis to the Averaged Velocity Profile

If there is no disturbance at the boundary and it will be free stream outside the domain (a, b) , then we have the corresponding boundary condition for function \hat{v} as $\hat{v}(a) = \hat{v}(b) = 0$ and $D\hat{v}(a) = D\hat{v}(b) = 0$. The second order central difference scheme (Equation (4.9)) is used to derive the finite different equation from Equation (4.7),

$$\begin{cases} D^2 \psi = (\psi_{n+1} - 2\psi_n + \psi_{n-1}) / h^2 \\ D^4 \psi = (\psi_{n+2} - 4\psi_{n+1} + 6\psi_n - 4\psi_{n-1} + \psi_{n-2}) / h^2 \end{cases} \tag{4.9}$$

Apply (4.9) to Equation (4.8) we can get the generalized eigenvalue problem:

$$A\varphi + Bc\varphi = 0 \tag{4.10}$$

Where A (symmetric pentadiagonal matrix) and B (symmetric tridiagonal matrix) are the coefficients' matrix and the vector φ denotes the values of \hat{v} at different position. c becomes the generalized eigenvalue of Equation (4.10).

$$A = \begin{bmatrix} a_{11} & a_{12} & a_{13} & 0 & . & . & . & . \\ a_{21} & a_{22} & a_{23} & a_{24} & 0 & . & . & . \\ a_{31} & a_{32} & a_{33} & a_{34} & a_{35} & 0 & . & . \\ . & . & . & . & . & . & . & . \\ . & . & . & . & . & . & . & . \\ . & . & . & 0 & a_{n-2,n-3} & a_{n-2,n-2} & a_{n-2,n-1} & a_{n-2,n} \\ & & & & 0 & a_{n-1,n-2} & a_{n-1,n-1} & a_{n-1,n} \\ & & & & & 0 & a_{n,n-1} & a_{n,n} \end{bmatrix} \quad (4.11)$$

$$B = \begin{bmatrix} b_{11} & b_{12} & 0 & 0 & . & . & . & . \\ b_{21} & b_{22} & b_{23} & 0 & 0 & . & . & . \\ 0 & b_{32} & b_{33} & b_{34} & 0 & 0 & . & . \\ . & . & . & . & . & . & . & . \\ . & . & . & . & . & . & . & . \\ . & . & . & 0 & b_{n-2,n-3} & b_{n-2,n-2} & b_{n-2,n-1} & 0 \\ & & & & 0 & b_{n-1,n-2} & b_{n-1,n-1} & b_{n-1,n} \\ & & & & & 0 & b_{n,n-1} & b_{n,n} \end{bmatrix} \quad (4.12)$$

$$\varphi = (\varphi_1, \dots, \varphi_n)^t \quad (4.13)$$

In the m^{th} line of matrix A and B,

$$a_{m+2} = 1 / h^4 \quad (4.14)$$

$$a_{m+1} = -4 / h^4 - (2\alpha^2 + i\alpha \text{Re}U_0) / h^2 \quad (4.15)$$

$$a_m = 6 / h^4 + (4\alpha^2 + 2i\alpha \text{Re}U_0) / h^2 + \alpha^4 + i\alpha \text{Re}(\alpha^2 + D^2U_0) \quad (4.16)$$

$$a_{m-1} = -4 / h^4 - (2\alpha^2 + i\alpha \text{Re}U_0) / h^2 \quad (4.17)$$

$$a_{m-2} = 1 / h^4 \quad (4.18)$$

$$b_{m+1} = \frac{i\alpha \text{Re}}{h^2} \quad (4.19)$$

$$b_m = \frac{2i\alpha \text{Re}}{h^2} \quad (4.20)$$

$$b_{m-1} = \frac{i\alpha \text{Re}}{h^2}$$

(4.21)

By solving the general eigenvalue problem (4.10), we can get the physical solution of the frequency c , whose imaginary part c_i is about 0.068 for our case. The positive value means this kind of flow is unstable. Fig. 4.22 shows the corresponding shape of the eigenvector function, \hat{v} .

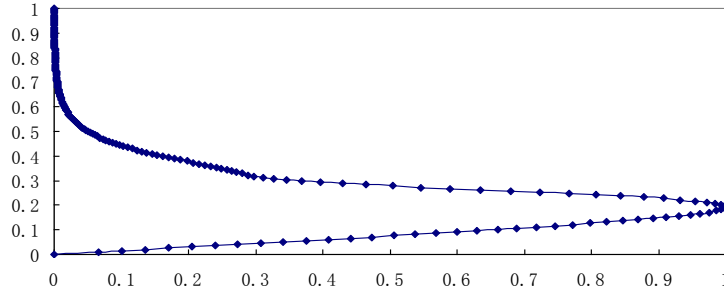


Figure 4.22 Eigenvector Function of \hat{v}

In Fig. 4.23, the 3D distribution of three components of vorticity is given right after the MVG. It shows that spanwise vorticity is first generated at the top of momentum deficit area where clusters the streamwise vortices. After that, the ring sides for the first ring are also generated on the boundary of momentum deficit. This confirms our assumption above. The top boundary of the momentum deficit has the most unstable shear layer, so the spanwise vorticity is first generated while the corresponding vortex directly connect to the streamwise vortex inside at first. Then the rings show up soon due to the evolution of the instable shear layer. Also we can find that the whole ring is generated on the boundary of the momentum deficit, neither from

inside nor outside region. So, the shear layer instability is the main mechanism of the ring generation.

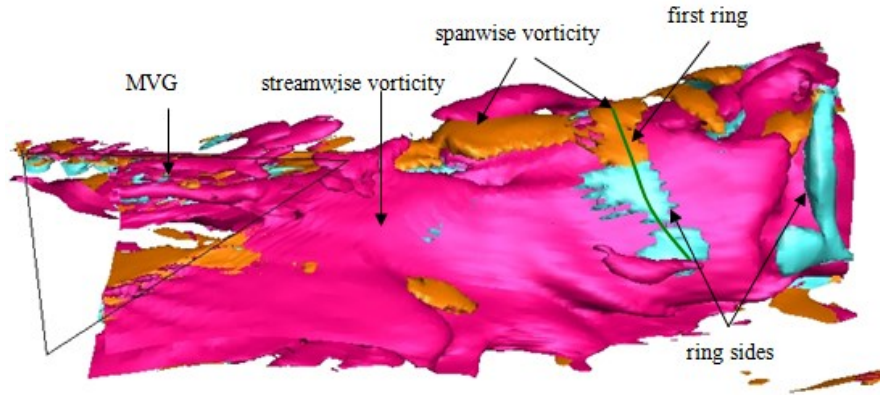


Figure 4.23 The Instantaneous Vorticity Distribution[57]

The mechanism of the ring generation is a real 3D process. Study in non-linear, 3D and compressible stability analysis is needed to reveal the full mechanism of the shear layer instability behind MVG. The current study only involves temporal, linear, and incompressible stability analysis which can be considered as a first step to study the wake instability of MVG.

The interaction between the streamwise vortices and vortex rings shown by vorticity is a new interesting phenomenon. The interaction and vorticity conservation of the primary streamwise vortex and new generated K-H vortex ring needs validation by experiment and the mechanism is still under investigation.

Chapter 5

INVESTIGATION OF MOMENTUM DEFICIT

The momentum deficit and primary vortices were considered two major features of supersonic flow control with MVG. Benefited from the high order scheme which is able to resolve detailed turbulent structures, the LES study of Li et al.[57] summarized several other flow features, such the ring vortex generated by the Kelvin-Helmholtz (K-H) instability at the circular shear layer. Since these two features are especially significant in the wake of the micro-ramp, a question would be raised regarding the connection between them: Is the momentum deficit a result of the primary vortices, or where is the origin of the low momentum fluid in the deficit region?

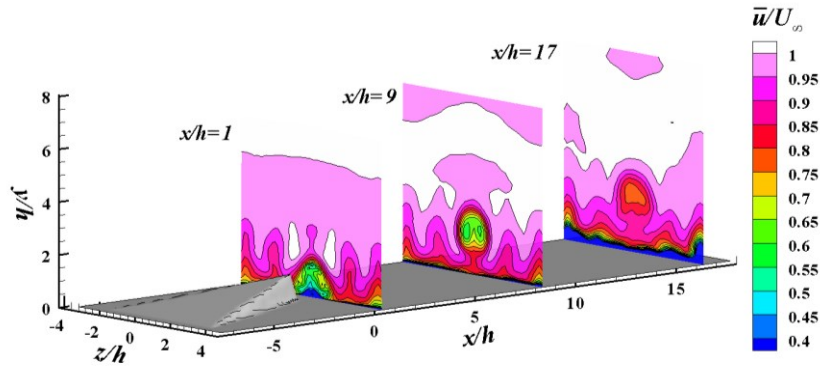
In order to consolidate the observation of Li et al.[57], the flow around the micro-ramp was simulated by means of LES with high order high resolution difference scheme in the present study. In the exploration of the deficit origin, streamline tracing at several heights in the incoming boundary layer was performed.

5.1 The Momentum Deficit

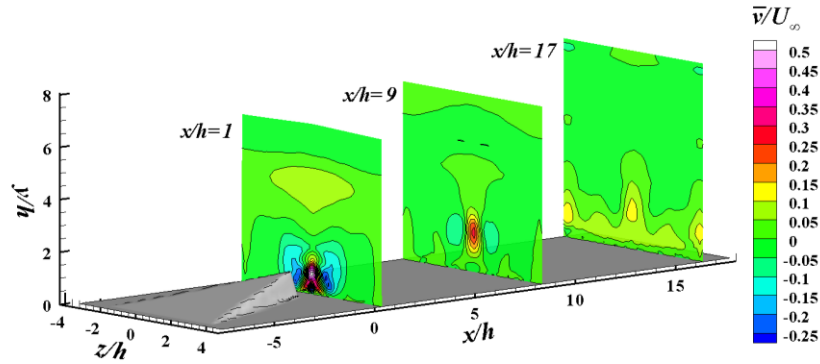
5.1.1 The deficit in the mean flow

As an entry to the understanding of the momentum deficit generation, the mean and instantaneous flow properties of the supersonic wake that contains the momentum deficit are first introduced. An overall view of the averaged wake is plotted in figure 10, where three different streamwise slices of u and v contours are included, so that the streamwise development can be visualized. It should be mentioned that the color bar for u is chosen from $0.4U_\infty$ to $1.0U_\infty$, instead of starting from 0, for better visualization of the decayed flow pattern further downstream. A region with significant low u is produced immediately after the micro-ramp. Elevation in position and recovery in magnitude are experienced when traveling downstream. Correspondingly, the v forms a focused central upwash and two symmetric downwash events at both sides, which coalesce to notify the counter rotating vortex pair. The

decay of v -event also happens throughout the development. A sharp reader would notice the wavy contour lines close to the flow floor in figure 5.1 (a). This is the residual large structure embedded in the turbulent boundary layer from the DNS result, as limited ensemble size ($N=300$) is used for averaging the flow.



(a) Contours of averaged u ;



(b) Contours of averaged v ;

Figure 5.1 An overview of the streamwise development of the micro-ramp wake, cross-sections are at $x/h=1, 9$ and 17 respectively.

In order to investigate the wake in detail, the three cross-sections in figure 10 are further enlarged in figure 5.2. The color bars are kept consistent with those in figure 10. The intended momentum deficit can be easily detected through the region containing weak u . A triangular shape is displayed at $x/h=1$ as it is the initial stage of the deficit. Upon leaving the

wall, a circular shape as shown in figure 5.2(b) is obtained. Throughout the development of the wake, the minimum u decreases from $0.5U_\infty$ at $x/h=1$ to $0.8U_\infty$ at $x/h=17$. Due to the velocity difference between the free stream and the deficit, a shear layer is formed wrapping the deficit.

As the presence of the symmetric slant edges of the micro-ramp, a pair of opposing vortices is produced in streamwise direction. These two vortices can be observed through the overlaid vectors and they are located inside the deficit region. The vortices also decay, as strong swirling vectors are visualized at $x/h=1$ while they are barely visible at $x/h=17$.

The focused central upward region of v is generated as a joint result of upwash vectors. Meanwhile, two symmetric downwash events are produced, obtaining approximately half the strength of the upwash in measure of v magnitude. Following the decay of vorticity strength, the maximum upward v of $0.5U_\infty$ at $x/h=1$ reduces to approximately $0.1U_\infty$ at $x/h=17$, indicating a weak imprint of upwash in the downstream position.

A side observation of the vectors in figure 5.2(a) and 5.2(d) features the secondary vortex pair shedded from the root portion of the sharp trailing edge. This pair of secondary vortices also obtain counter rotations and are produced in a smaller scale than the primary pair. Since it is not very influential to the present topic of the large scale momentum deficit, this secondary pair is not going to be elaborated in detail.

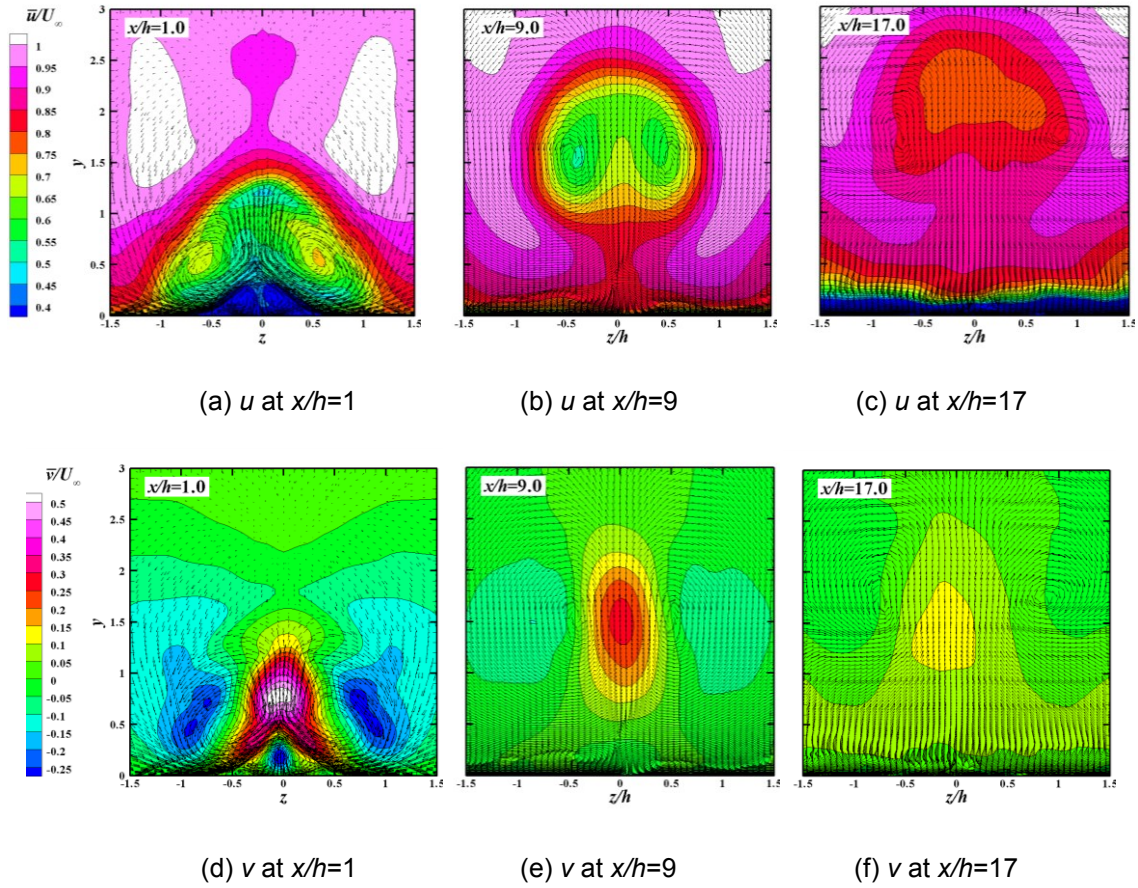


Figure 5.2 Cross-sections of mean u and v contours at three streamwise positions with two-dimensional vectors overlaid.

5.1.2 The deficit in the instantaneous flow

Instead of visualizing the smoothed flow patterns through averaged flow field, the instantaneous realizations on the other hand offer to exhibit the instantaneous variations. Cross-sections at $x/h=1, 9$ and 17 are again extracted from one flow field snapshot and plotted in figure 5.3.

All the revealed structures, such as the u -deficit, the upwash and downwash, and the primary vortex pair, can also be observed in the instantaneous velocity contours. At the immediate downstream of the trailing edge, i.e. $x/h=1.0$, the contours of both u and v resemble the averaged pattern with only a slight curvature of the contour lines, indicating greater flow

instability. Further downstream, considerable variations are presented. For the current instantaneous representation at $x/h=9$, the mushroom-shaped u -deficit has sever curved edges and it further inclined towards the left side at $x/h=17$. The upward region of v at $x/h=9$ obtains a central peak magnitude of approximately $0.3U_\infty$, however a stronger downwash with $v=-0.2U_\infty$ at the right side is generated, suggesting the asymmetric vortex strength. Although a peak of upward v still persists at $x/h=17$, it only survives in a really small region with $v=0.25U_\infty$ and deviates from the central location.

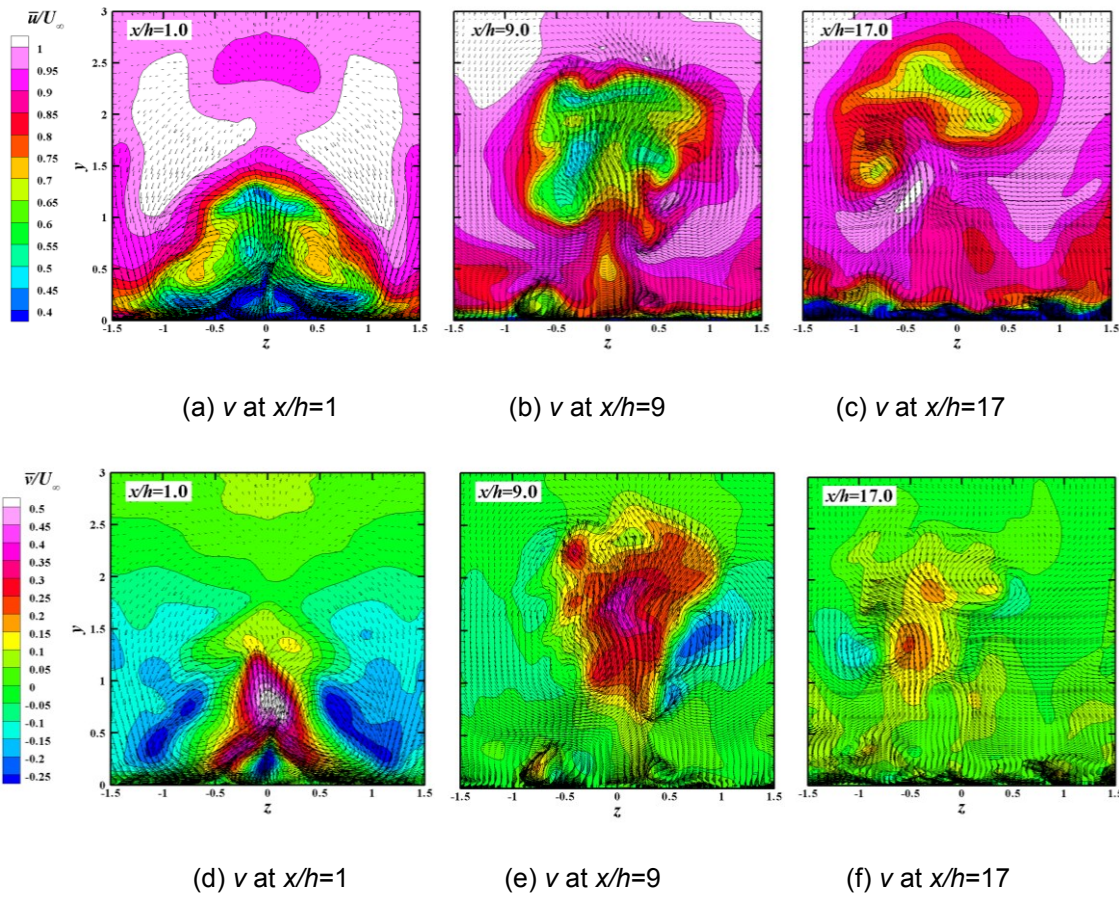


Figure 5.3 Cross-sections of instantaneous u and v contours at three streamwise positions with two-dimensional vectors overlaid.

5.1.3 The mean and instantaneous streamwise vortical structure

Although the streamwise vortices can be observed and qualitatively studied from the overlaid vectors in the contour plots, a dedicated representation and quantitative investigation can be achieved through the distribution of streamwise vorticity component as plotted in Fig.

5.4. It should be mentioned that the instantaneous vorticity in the right column is calculated from the same snapshot, and different color bars are used for the purpose of visualizing the reduced magnitude of downstream vorticity. Decent symmetry of the vortex pair is presented through the mean representation, although curved edges can be observed due to limited statistical ensemble size. Instead of using upward and downward v as an indication of vortical activity, a straightforward evaluation of the vorticity development can be achieved. The vortical strength at $x/h=17$ reduces to approximately one tenth of that at $x/h=1$.

Variation from the mean vortical pattern is exhibit by the instantaneous representations in the right column of figure 5.4. The primary vortex pair is produced on either side of the center plane, resembling the mean flow. Affected by fluctuation and flow instability, namely the Kelvin-Helmholtz instability (see Sun et al.[33]), the focused mean vorticity pattern is distributed into several irregular spatial pockets following the variation of the u -deficit.

The momtmtum deficit can so far be understood as a region containing reduced magnitude of u with a central upwash and side downwashes. On the other hand, a pair of primary opposing vortices is generated and obtains a similar decay process as the velocity patterns.

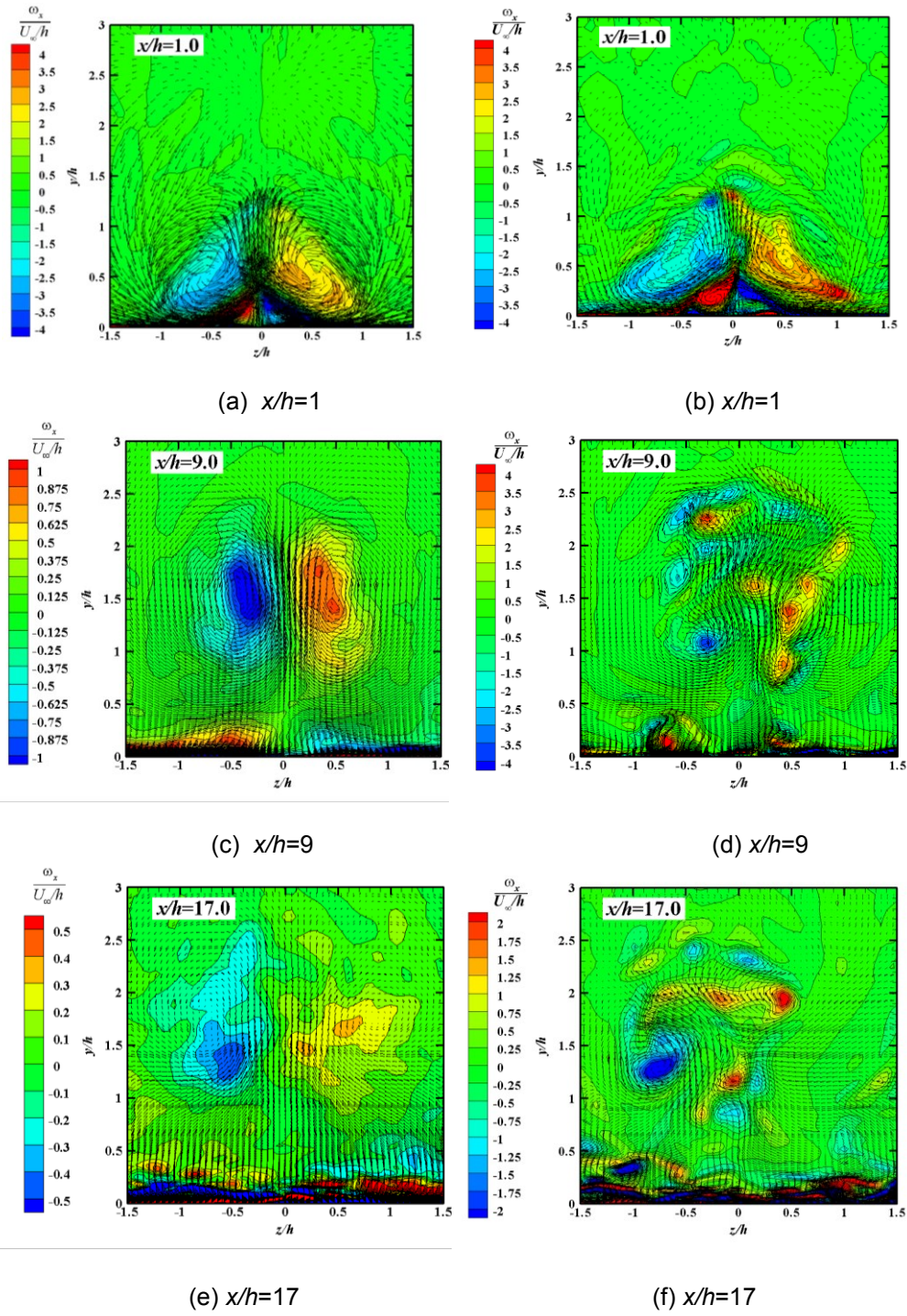


Figure 5.4 Cross-sectional contours of streamwise component of vorticity ω_x .

5.2. The Origin of Momentum Deficit

In order to reveal the source of momentum deficit, streamline tracing at different wall-normal positions are carried out and six of them are plotted in figure 5.5. This analysis is based on the mean flow field. Figure 5.5(a) shows the streamlines that stem from $y_0/h=0.0092$. They mainly form the leading edge separation due to their low momentum. However, the streamlines close to the edges of the micro-ramp are capable of passing downstream and then contracted towards the center along the slant edges and are further lifted upward through the spiral motion. The flow outside the width of the micro-ramp is barely affected by the micro-ramp although slight curvature of the streamlines can be observed there. In figure 5.5(b), the streamlines originate from $y_0/h = 0.0412$. The leading edge separation is reduced because of higher momentum the fluid obtains. More streamlines are entrained downstream by vortical motion and contribute into the u-deficit. As the tracing position is elevated, as shown in figure 5.5(c) and 5.5(d), no separation remains. The flow there along the whole span moves forward and concentrate into two parallel neighboring vortices through the spiral activity once the micro-ramp is past. However, less spiral motion is behaved by the flow originates from even higher wall-normal positions (as shown in figure 5.5(e) and 5.5(f)). The major portion of the flow along the micro-ramp span is directed downward and enters into the flow below the momentum-deficit, although a few streamlines close to the center are diverted outward forming the streamlines that wrap the deficit region and resultantly contribute to the circular shear layer.

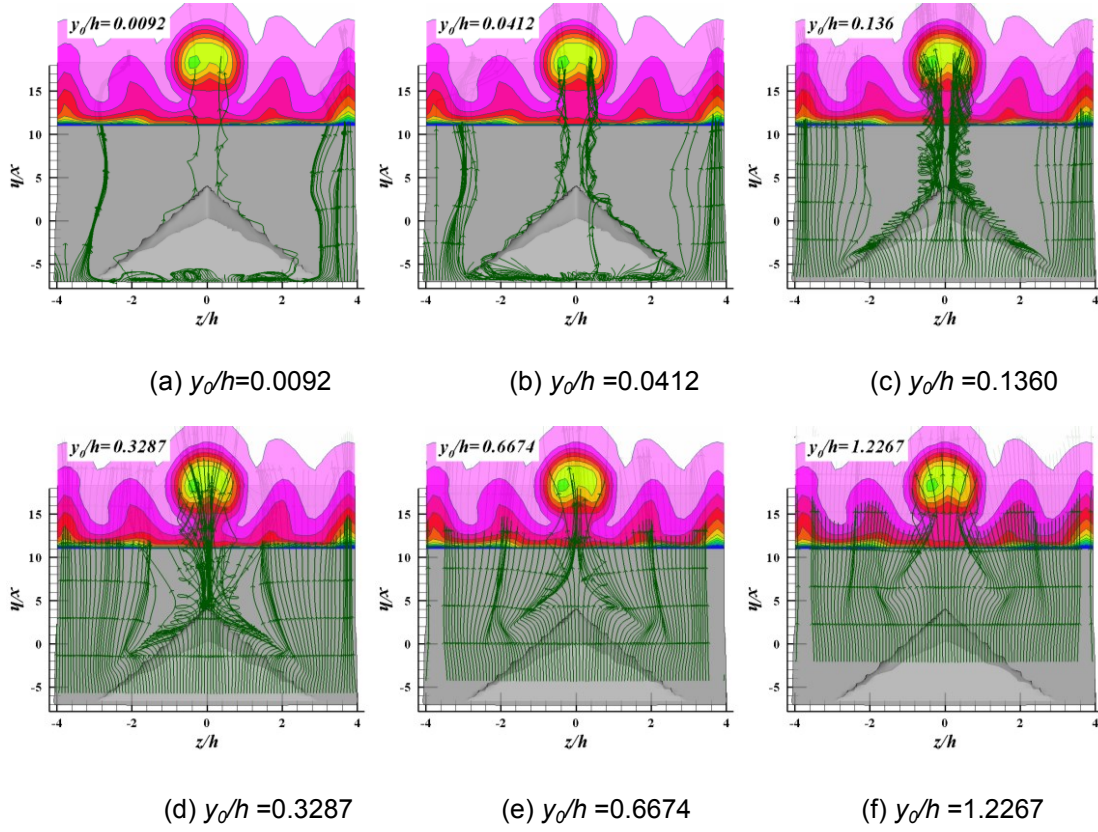


Figure 5.5 Streamlines with origins at different wall-normal positions upstream of the microramp.

The streamline rake originating from a fixed spanwise position at $z/h=1.1$ is further plotted in figure 5.6 to consolidate the above observations in figure 5.5. Apart from the confirmation of deficit origin from the lower portion of the boundary layer, the *position alternation* is better revealed: the lower level flow in the incoming boundary layer is lifted upward through the vortical activity forming the momentum deficit, while the upper level flow with higher momentum is, on the contrary, directed into a lower position past the micro-ramp, resulting in a fuller boundary layer close to the floor.

As the position alternation happens along the whole span of the micro-ramp, in order to entrain larger amount high momentum fluid of the incoming boundary layer into the near wall region, a wider micro-ramp should be considered. Recall the result of Lee and Loth[65], the half

width micro-ramp produces worse downstream boundary layer than the regular type in measure of shape factor.

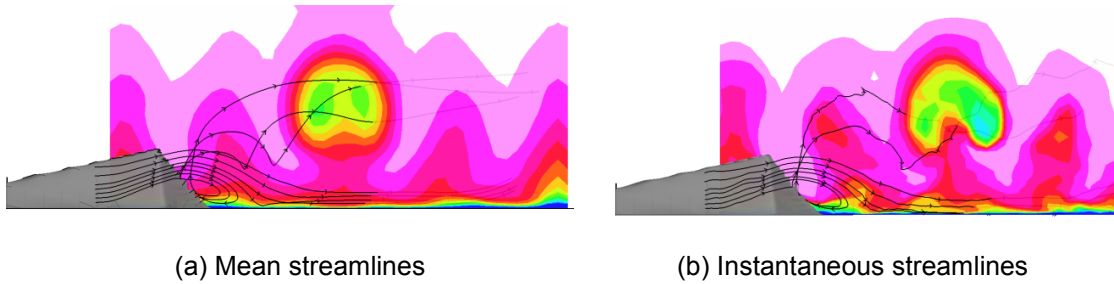


Figure 5.6 Streamlines with origins at a fixed spanwise position $z/h=1.1$.

5.3 The Position Alternation – A Revised Mechanism

As revealed by section 5.2, the process of position alternation is going to be explored in detail. The seven mean streamlines in figure 5.6(a) are extracted and projected into the x-y plane as shown in figure 5.7. It should be mentioned that the axis ratio is exaggerated to help observation. It should also be noted that no line map is listed in figure 5.7 as they can be identified from the position of origination. Solid lines are used to feature the lower level streamlines which are lifted, while dashed lines for the higher level flow entrained downward. The same line system is applied to figure 5.8. A clear bifurcation of the streamlines right after the micro-ramp is better visualized, indicating the position alternation. The winding of the solid curves represents the swirling motion. The lowest level fluid, namely the red curve, endures strong spiral activity, while less for the higher ones, namely the solid blue and black curves. However no spiral motion can be observed for the dashed streamlines. And once they are entrained into the near wall region, their positions remain.

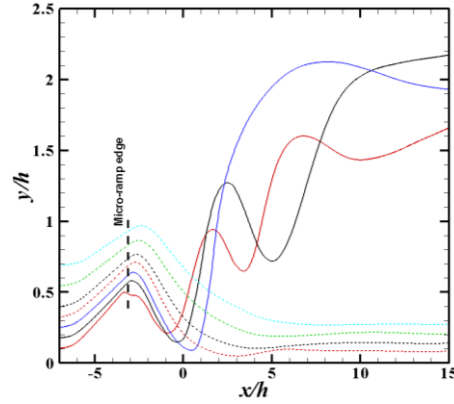
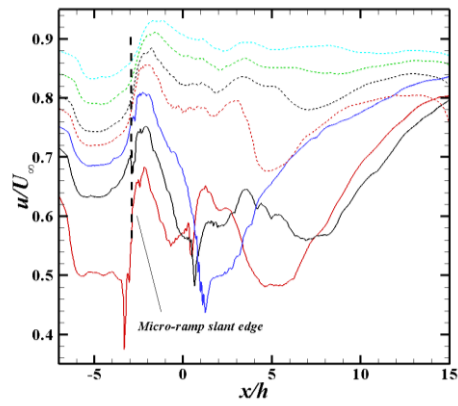


Figure 5.7. The projected streamline in the x - y plane, the streamlines are those in figure 5.6(a).

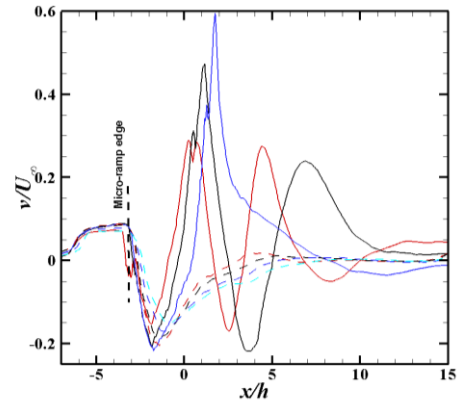
Streamwise and wall-normal velocity components along the streamlines in figure 5.7 are further plotted in figure 5.8. Upon leaving the micro-ramp, a sudden drop of u is endured by the lower level flow due to the flow separation. Fluctuations are further experienced through the swirling in the deficit region and eventually recover to a higher magnitude, which is consistent with the recovery of momentum deficit.

A rapid increase of v can be observed close to the trailing edge, and a maximum is later reached. This is a common event for the fluid along these streamtraces and explains the focused upwash behind the micro-ramp. Similar to the behavior of u , fluctuating v is also exhibited. At far downstream, wall-normal velocity for all the streamlines approaches zero. The downward entrained flow with higher momentum, represented by the dashed curves, exhibits less fluctuation for both u and v , as no large scale vortical effects are present there.

At this point, the current observation does not give support to the prescribed knowledge of the working principle which considers the higher momentum in the downstream flow is entrained from the surrounding free stream. Because the foregoing illustrations find that the desired high momentum in the near wall region is achieved through the position alternation triggered by the micro-ramp instead of the downstream trailing vortex filaments.



(a) streamwise component



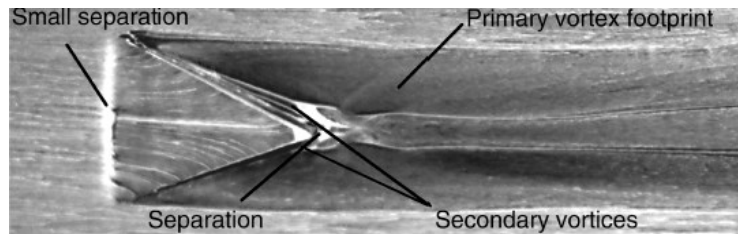
(b) wall-normal component

Figure 5.8 The streamwise and wall-normal velocity components along the extracted streamlines(Sun et al.).

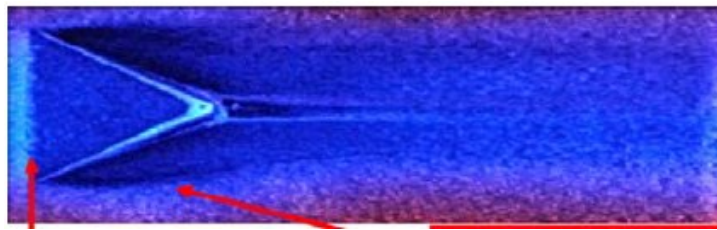
Chapter 6

VORTICAL STRUCTURES IN THE REAR SEPARATION AND WAKE AFTER MVG

Larger scale structures like vortex rings or the interaction mechanism between the ring vortex and shock wave, take place in the wake region, which is relatively downstream of the micro-ramp. However, less focus has been placed on the smaller scale structures in the flow close to the micro-ramp. A few forgoing studies have investigated the flow that takes place around the micro-ramp[66,67]. Among those explorations, a common observation is the flow separation at the junction between the micro-ramp trailing edge and the flow floor. Shown in figure 6.1 and 6.2 are some experimental and numerical results of rear separation. These visualization work shows the flow structures like spiral points and vortex filaments close to the trailing edge of MVG. To better understand the mechanism of flow pass MVG, velocity distribution and vortex line method, has been used to the analysis of flow structures near trailing edge.

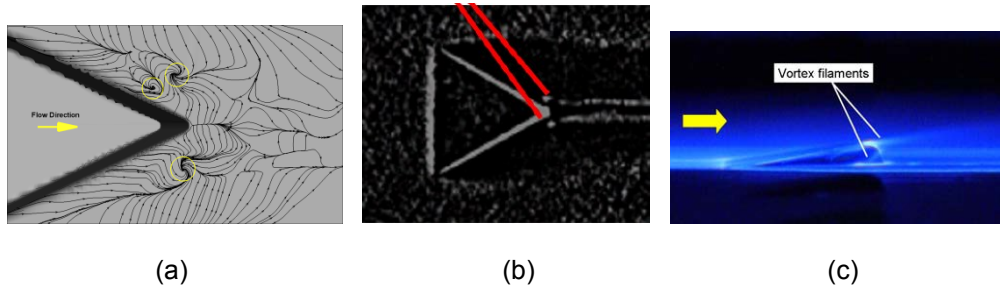


(a) Trailing edge separations in the oil flow visualization by Babinsky et al.[7].



(b) Trailing edge separation in the surface flow visualization by Lu et al.[56]

Figure 6.1 Experimental visualization of the rear separation.



(a) The spiral points close to the trailing edge (reproduction according to Li[66]).

(b) The spiral points in the experiment of Lu et al.[56]

(c) The vortex filaments from the experiment of Lu et al.[56]

Figure 6.2. The spiral point at the rear

6.1. Two-Dimensional Representation of the Rear Separation

According to the previous studies, the separation region is recognized as a common phenomenon. By plotting the instantaneous snapshots of u -contours close to the micro-ramp at different heights, the flow organization is evident.

Figure 6.3(a) is the instantaneous contour of u at $y/h=0.018$ after the flow is "stable". Two regions with reverse u are clearly observed and their positions are similar to the observations in oil flow visualization (see Fig. 6.1(a)). The reverse flow obtains a maximum magnitude of approximately $0.2U_\infty$ at this height and has a streamwise extension of about $2.0h$. Thus a shear is formed at the border of the reverse region and surrounding downstream moving fluid. According to the overlaid projected streamlines, three vortices (labeled as V1, V2 and V3 in Fig. 6.3 (a)) are produced at the edge of the reverse regions, among which V2 and V3 appear in pair and have counter rotation, while V1 stays at the outer edge. Note that the slices in Fig. 6.3 are extracted from the same snapshot as that in Fig. 6.2(a), the revealed vortices can then be taken as the cross-sections of the vortex filament. The contour in Fig. 6.3(b) is at $y/h=0.036$. The reverse regions at this height contract in area and become slimmer. V2 and V3 are still visualized at the edge, and both of them shifted slightly in position, which can be compared in table II. Figure 6.3(c) and (d) represent the contour at $y/h=0.047$ and 0.100 , respectively, where

the reverse flow is weaker and shrinks. V2 exists at the outer edge of the reverse region, and two additional vortices, namely V5 and V6, are produced at the downstream edges of the reverse region. The detailed spatial coordinates of the revealed vortices are summarized in table II.

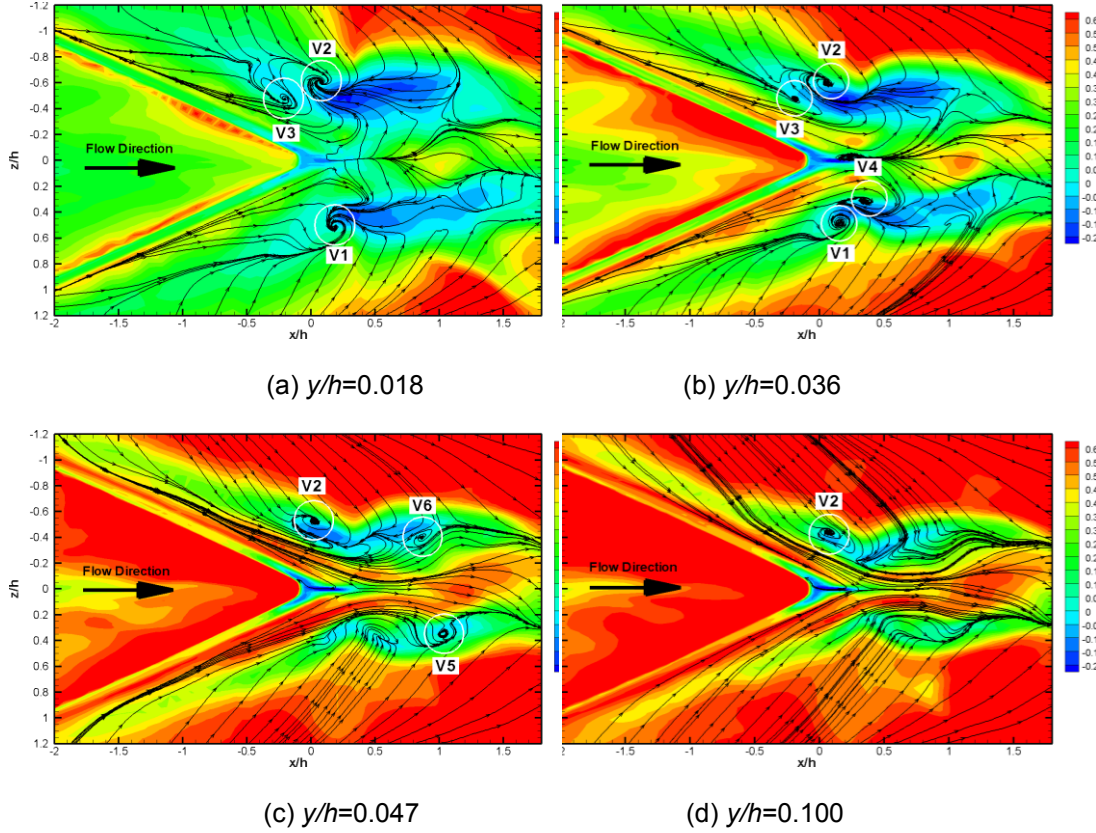


Figure 6.3. Contour of u at four heights with projected streamlines.

We used the position of V2 and V1 in table II and drew vortex lines from the core of vortices(see Fig. 6.4). The vortex lines clear revealed that V2 and V1 are actually one connected vortex tube and Fig. 6.3 is the cross-section of this Ω shaped vortex at different heights.

Table 6.1 The coordinates of the revealed vortices in Fig. 6.3.

	$y/h=0.018$	$y/h=0.036$	$y/h=0.047$	$y/h=0.100$
V1 ($x/h, z/h$)	(0.192, 0.514)	(0.154, 0.489)	-	-
V2 ($x/h, z/h$)	(0.085, -0.600)	(0.057, -0.600)	(0.036, -0.529)	(0.075, -0.438)
V3 ($x/h, z/h$)	-0.197, -0.473	(-0.191, -0.471)	-	-
V4 ($x/h, z/h$)	-	(0.351, 0.318)	-	-
V5 ($x/h, z/h$)	-	-	(1.033, 0.349)	(0.864, -0.401)
V6 ($x/h, z/h$)	-	-	-	-

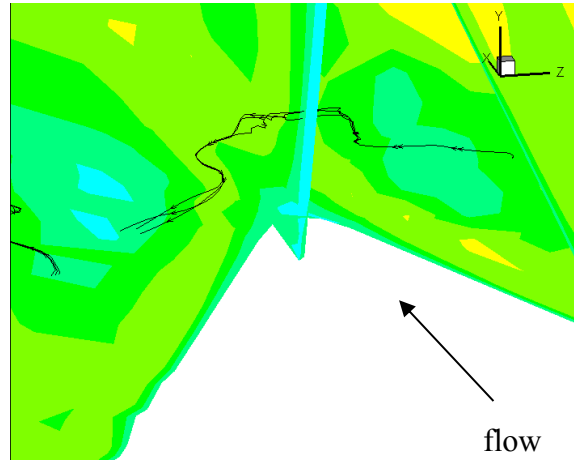


Figure 6.4. Vortex lines passing vortex cores of v_z and v_1 .

6.2. Three-Dimensional Representation of the Rear Separation.

By examining the evolution of the reverse flow along the wall-normal direction, it obtains a larger base portion and a thinner body at higher elevation. A mountain-shaped reverse flow region can thus be imagined. The three-dimensional representation of the separation region is illustrated in Fig. 6.5 through isosurface of u with a value of $-0.01U_\infty$. All the stronger reverse flow is inside the current isosurface. It should be noted that a third reverse flow region is present along the trailing edge.

Till this point, questions can be raised regarding the revealed vortices in the Fig. 6.3: what is their three-dimensional organization? Are they related in space? These questions can be answered by analyzing the vortex line. In Fig. 6.6 five vortex lines are plotted in the vicinity of reverse region 1. Note that the second vortex line from left in Fig. 7(a) passes through V2 in Fig. 6.3(a). All the vortex lines originate from the wall surface where significant vorticity magnitude is present. Once lifted away from the wall, they follow the inclined surface of the separation region, after passing the summit, it drops in height, but, however, still follow the iso-surface slope. The appearance of the vortex line forms an Ω -like shape. Similar analysis has been carried out on the vortex lines around reverse region 2 and Ω -like vortex lines are also resulted. The vortices as visualized in Fig. 6.6 can hence be concluded as imprints of the omega-shaped filaments and they are produced due to the strong shear between the core reverse flow and the surrounding fast-moving flow.

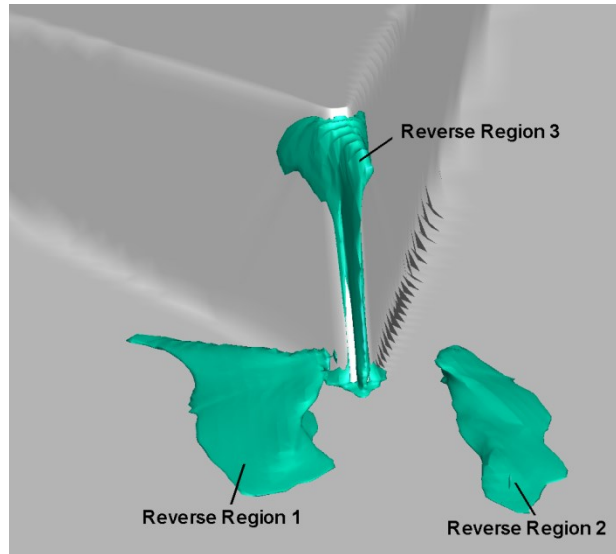


Figure 6.5. The three-dimensional representation of the rear separation regions using isosurface of $u=-0.01U_{\infty}$.

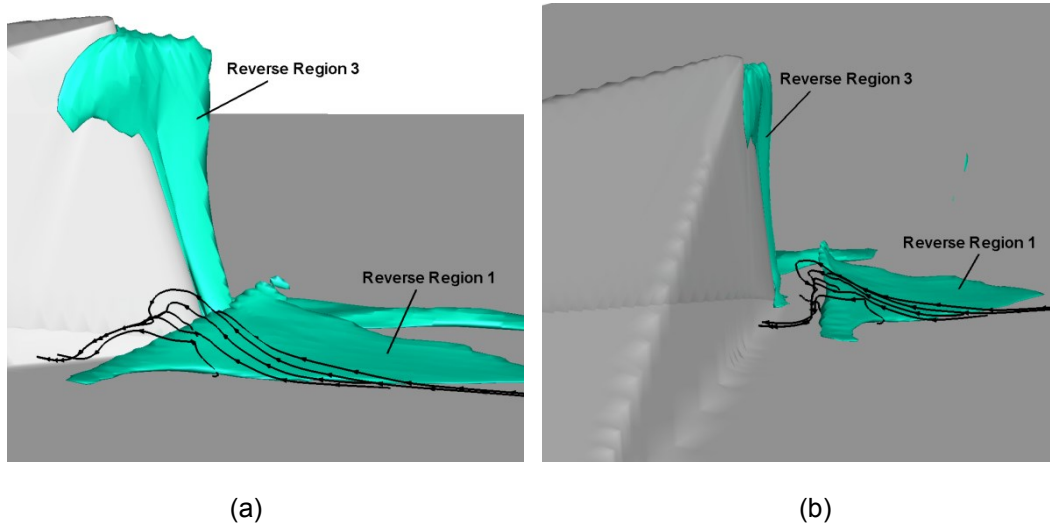


Figure 6.6 The Ω -shaped vortex lines around reverse region 1.

6.3. Similar Vortical Structure in the Micro-Ramp Wake

Recalling the flow organization in the wake of the micro-ramp, a momentum deficit is at the center and a curved shear layer is then formed between the deficit region and free stream. Due to the instability of the shear layer, arch-shaped Kelvin-Helmholtz vortices are generated. This turbulent activity that happens in the wake has been substantially discussed by Sun et al.⁸. Comparing the two flow structures at the rear separation and the wake region, they are conceived to be similar, as both obtain low speed flow in the center and higher speed in the outer flow and a shear layer in between are plotted. Q-criterion is chosen to feature the isosurface in Fig. 6.7 (a) and (b), so that the arch-shaped K-H vortices together with the streamwise vortices can be visualized simultaneously. If we draw vortex lines from the position of vorticity core, the vortex lines follow the shape of the Q-isosurface, especially the round head portion.

In Fig. 6.7 (c) and (d), a streamwise velocity component of $u=0.5U_\infty$ is chosen to represent the momentum deficit in the wake, all the vortex lines curve at the top to wrap the deficit region. These two observations, especially the later one, are rather similar as that in Fig. 6.6 in which the vortex lines also wrap the reverse regions.

By removing the isosurface, the three vortex lines are solely depicted in Fig. 6.8 with different colors. The most upstream vortex line (red) exhibits a strict Ω shape, suggesting this larger scale vortex receives vorticity from the near wall region. The next two downstream vortex lines (black and green) obtain a round head, however they both have stretched legs extending upstream, which means streamwise vortices contribute to these two vortices. The transformed Ω -shaped vortex line (black and green) resembles the similar vortex line that takes place in the turbulent boundary layer which shows up as the hairpin vortex. Due to the similarity, studying the micro-ramp flow can also shed some light into the understanding of wall bounded turbulence. Because of its larger scale, it provides a relatively easier entry level.

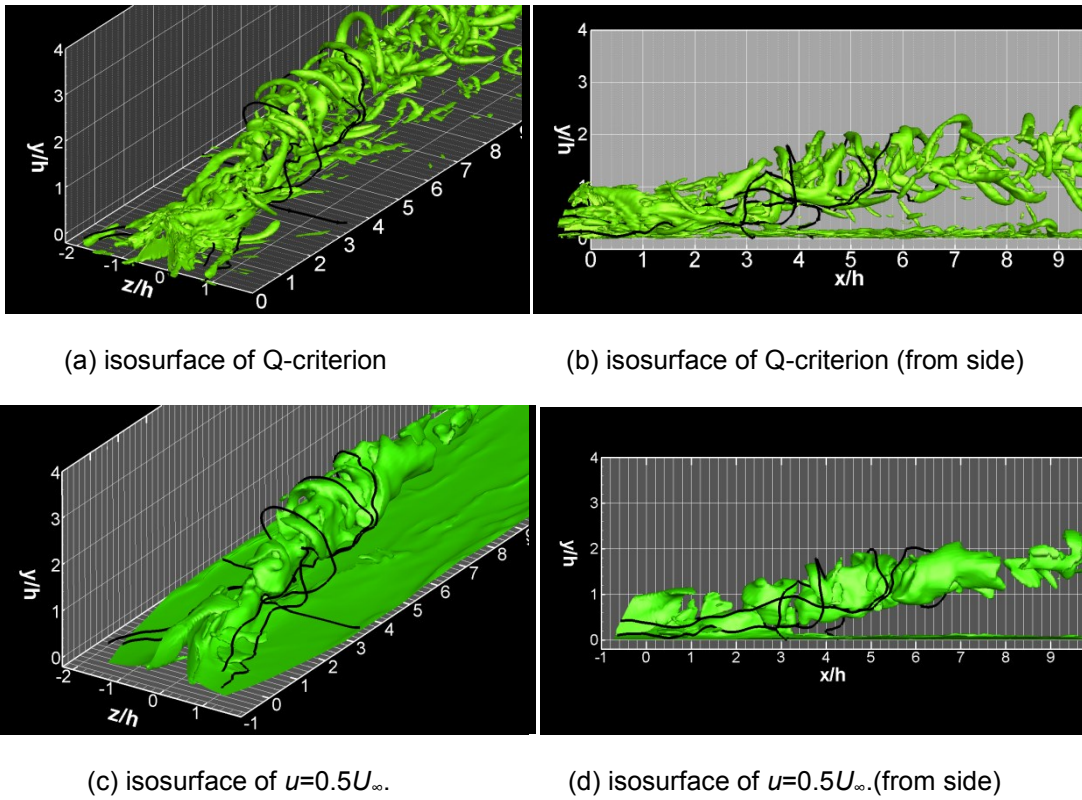


Figure 6.7. The three-dimensional representation of the micro-ramp wake with vortex lines.

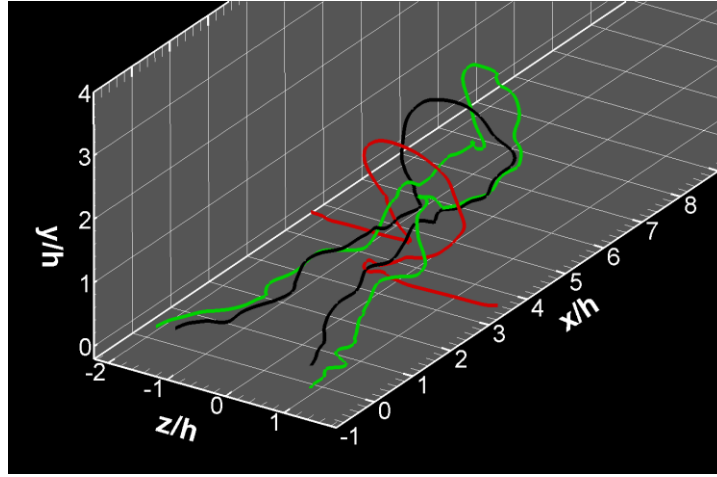


Figure 6.8 The three vortex lines after removing the isosurface in Fig. 6.7.

6.4 Conclusions and new conceptual topology model

Summarizing the above discussion on the vortical structures in the rear separation and wake region, several conclusions can be drawn:

1. The flow separation has been clearly revealed and the current numerical result agrees with the experimental observation through the velocity contours.
2. The spiral points at the rear of the micro-ramp can now be understood as the cross-sections of the small scale vortices. Through the vortex line method, these vortices take the form of Ω -like shape and wrap the recirculation region.
3. The micro-ramp wake obtains similar flow structure as the rear separation where high speed flow wrapping the low speed with shear layer in between. Similar Ω -shaped vortex lines have been a proof. However the vortex lines in the wake region may exhibit extended leg portions corresponding to the streamwise vortices. A conceptual model for the common vortical structure for both the rear separation and the wake region is sketched in Fig. 6.9.
4. Similarity between the current vortical structure and that in the wall bounded turbulence can be proposed. As the flow structure has larger scale, further effort to the micro-ramp flow is desired to be mirrored into the smaller scale wall turbulence.

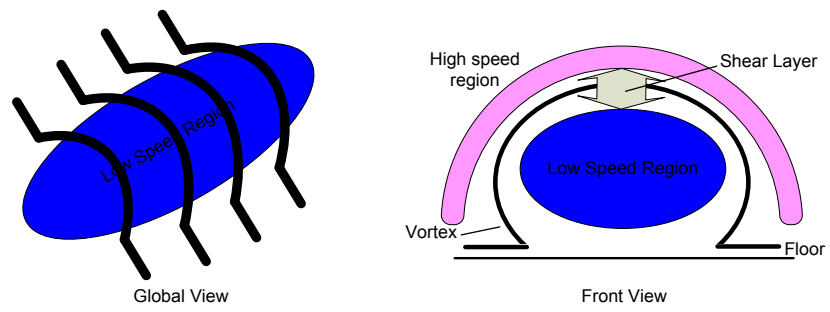


Figure 6.9. The conceptual model of the flow topology.

Chapter 7

STABILITY ANALYSIS OF COMPRESSIBLE FLOW PASSING A FLAT PLATE

7.1 The derivation of linear stability equations

Reorder Navier-Stokes equations governing the flow of a viscous compressible ideal gas as momentum, continuity and energy equation. Combined with status equation, the system could be written as:

$$\rho \frac{\partial \vec{v}}{\partial t} + \rho(\vec{v} \cdot \nabla) \vec{v} = -\nabla p + \frac{1}{Re} \nabla \cdot [\mu(\nabla \vec{v} + \nabla \vec{v}^{tr}) + \lambda(\nabla \cdot \vec{v}) \bar{I}] \quad (7.1)$$

$$\frac{\partial \rho}{\partial t} + \nabla \cdot (\rho \vec{v}) = 0 \quad (7.2)$$

$$\frac{Dh}{Dt} = \rho \frac{D}{Dt} \left(e + \frac{\vec{v}^2}{2} \right) = \frac{Dp}{Dt} + \frac{1}{(\gamma-1)PrReM_\infty^2} \nabla \cdot k \nabla T + q_R + \frac{1}{Re} \Phi \quad (7.3)$$

$$p = \rho RT \quad (7.4)$$

where \vec{v} is the velocity vector, ρ the density, p the pressure, T the temperature, R the gas constant, $Re = \rho_{\infty} u_{\infty} l / \mu_e$ the Reynolds number, γ the ratio of specific heats, Pr the Prandtl number, M_∞ the Mach number of inflow, k the thermal conductivity, c_p the specific heat at constant pressure. μ the first coefficient of viscosity, λ the second coefficient of viscosity, \bar{I} is the surface pressure tensor. The viscous dissipation Φ is given as:

$$\Phi = \frac{\mu}{2} (\nabla \vec{v} + \nabla \vec{v}^{tr})^2 + \lambda (\nabla \cdot \vec{v})^2 \quad (7.5)$$

The governing equations for the steady, basic flow may be derived by invoking the boundary layer assumption. The stability equations are then derived by assuming small disturbances superposed on the basic flow and substituting in the above Navier-Stokes equations. Though real gas effects become important at hypersonic speeds in atmosphere flight, we consider ideal gas flow since the numerical methods developed here would be applicable to the real gas conditions.

7.1.1. Basic Flow

We consider boundary-layer flow past two-dimensional or axisymmetric bodies. The governing equations for the basic state whose stability is the subject of this paper can be derived using the Mangler-Levy-Lees transformation[61]

$$d\zeta = \rho_e \mu_e u_e \left(\frac{r_0(x)}{L_r} \right)^{2j} dx \quad (7.6)$$

$$d\eta = [\rho_e \mu_e / (2\zeta)^{1/2}] (r/L_r)^j (\rho/\rho_e) dy \quad (7.7)$$

where ρ_e is the edge density, μ_e the edge viscosity, u_e the streamwise edge velocity, r_0 the body radius, L_r a reference length, x the distance along the body, and y normal to it. The exponent $j=0$ for a two-dimensional body and $j=1$ for an axisymmetric body. In $\zeta - \eta$ coordinates, the governing equations for the boundary layer flow may be written as:

$$(cf'')' + ff' + \bar{\beta} \left[\frac{\rho_e}{\rho} - (f')^2 \right] = 2\zeta \left(f' \frac{\partial f'}{\partial \zeta} - f'' \frac{\partial f}{\partial \zeta} \right) \quad (7.8)$$

$$(a_1 g' + a_2 f' f'') + fg' = 2\zeta \left(f' \frac{\partial g}{\partial \zeta} - g' \frac{\partial f}{\partial \zeta} \right) \quad (7.9)$$

where $f \equiv u/u_e$, $c \equiv (1+x)^{2j} \rho \mu / \rho_e \mu_e$, $\bar{\beta} \equiv \left(\frac{2\zeta}{u_e} \right) (du_e/d\zeta)$, $g \equiv H/H_e$, $a_1 \equiv c/P_r$,

$a_2 \equiv \frac{(\gamma-1)M^2}{1+(\frac{\gamma-1}{2})M^2} (1 - \frac{1}{P_r})c$ and χ is the transverse curvature parameter, $\bar{\beta}$ the pressure

gradient parameter, H the enthalpy, γ the ratio of specific heats, and M the edge Mach number defined as

$$M = \frac{u_e}{\sqrt{\gamma \mathcal{R} T_e}} \quad (7.10)$$

The Prandtl number P_r is defined as

$$P_r = \frac{\mu c_p}{k} \quad (7.11)$$

Where P_r is the specific heat at constant pressure and is assumed to be constant. The viscosity μ is assumed to be given by the Sutherland formula,

$$\mu = T^{\frac{3}{2}} \frac{1+C}{T+C}, \quad C = \frac{110.4}{T_\infty}$$

The thermal conductivity k may also be prescribed by a similar formula. For the results presented in this paper, however, we computer it by assuming $P_r = 0.7$.

For a flat plate with no pressure gradient, the above equations reduce to

$$(cf''')' + ff'' = 0 \quad (7.12)$$

$$(a_1g' + a_2f'f'')' + fg' = 0 \quad (7.13)$$

Note that this is a system of ordinary differential equations which have been solved by a fourth-order accurate compact difference scheme and nonlinear shooting method. Non-slip boundary conditions were used for either an insulated wall or for a specified wall temperature.

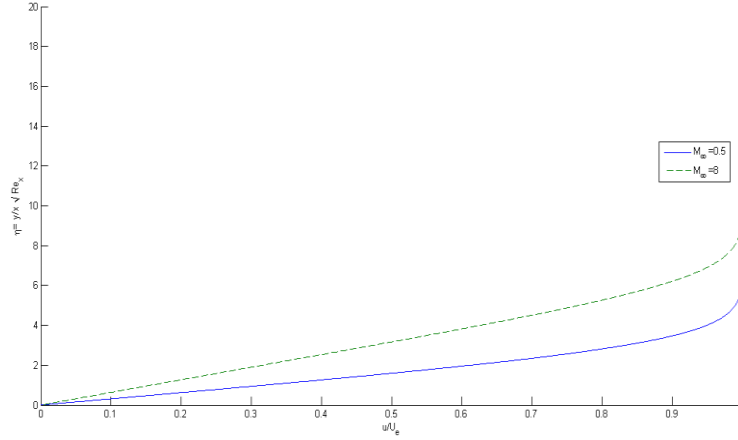


Figure 7.1. Velocity profile in a compressible laminar boundary-layer over our flat plate
(adabatic wall)

7.1.2 Compressible Linear Stability Equations

We use Cartesian coordinates x, y, z , where x is the streamwise direction, z is the spanwise direction and y is normal to the solid boundary. All the lengths are assumed scaled by a reference length l , velocities by u_e , density by ρ_e , pressure by $\rho_e u_e^2$, time by l/u_e , and other variables by corresponding boundary layer edge values. The instantaneous values of velocities, u, v, w , pressure p , temperature T , density ρ , may be repressed as the sum of a mean and a fluctuation quantity, i.e.,

$$u = \bar{U} + \tilde{u}, \quad v = \bar{V} + \tilde{v}, \quad w = \bar{W} + \tilde{w}$$

$$p = \bar{p} + \tilde{p}, \quad T = \bar{T} + \tilde{T}, \quad \rho = \bar{\rho} + \tilde{\rho}$$

$$\mu = \bar{\mu} + \tilde{\mu}, \quad \lambda = \bar{\lambda} + \tilde{\lambda}, \quad k = \bar{k} + \tilde{k}$$

Substituting these into the nondimensional form of the governing equations yields the linearized perturbation equations (after dropping "bars" from the mean quantities)

$$\begin{aligned} & \bar{\rho} \begin{bmatrix} \frac{\partial \tilde{u}}{\partial t} \\ \frac{\partial \tilde{v}}{\partial t} \\ \frac{\partial \tilde{w}}{\partial t} \end{bmatrix} + \bar{\rho} \begin{bmatrix} \bar{U} \frac{\partial \tilde{u}}{\partial x} + \tilde{u} \frac{\partial \bar{U}}{\partial x} + \bar{V} \frac{\partial \tilde{u}}{\partial y} + \tilde{v} \frac{\partial \bar{U}}{\partial y} + \bar{W} \frac{\partial \tilde{u}}{\partial z} + \tilde{w} \frac{\partial \bar{U}}{\partial z} \\ \bar{U} \frac{\partial \tilde{v}}{\partial x} + \tilde{u} \frac{\partial \bar{V}}{\partial x} + \bar{V} \frac{\partial \tilde{v}}{\partial y} + \tilde{v} \frac{\partial \bar{V}}{\partial y} + \bar{W} \frac{\partial \tilde{v}}{\partial z} + \tilde{w} \frac{\partial \bar{V}}{\partial z} \\ \bar{U} \frac{\partial \tilde{w}}{\partial x} + \tilde{u} \frac{\partial \bar{W}}{\partial x} + \bar{V} \frac{\partial \tilde{w}}{\partial y} + \tilde{v} \frac{\partial \bar{W}}{\partial y} + \bar{W} \frac{\partial \tilde{w}}{\partial z} + \tilde{w} \frac{\partial \bar{W}}{\partial z} \end{bmatrix} + \tilde{\rho} \begin{bmatrix} \bar{U} \frac{\partial \bar{U}}{\partial x} + \bar{V} \frac{\partial \bar{U}}{\partial y} + \bar{W} \frac{\partial \bar{U}}{\partial z} \\ \bar{U} \frac{\partial \bar{V}}{\partial x} + \bar{V} \frac{\partial \bar{V}}{\partial y} + \bar{W} \frac{\partial \bar{V}}{\partial z} \\ \bar{U} \frac{\partial \bar{W}}{\partial x} + \bar{V} \frac{\partial \bar{W}}{\partial y} + \bar{W} \frac{\partial \bar{W}}{\partial z} \end{bmatrix} = - \begin{bmatrix} \frac{\partial \tilde{p}}{\partial x} \\ \frac{\partial \tilde{p}}{\partial y} \\ \frac{\partial \tilde{p}}{\partial z} \end{bmatrix} + \\ & \frac{1}{Re} \left\{ \frac{\partial}{\partial x} \left[\begin{aligned} & 2 \left(\bar{\mu} \frac{\partial \tilde{u}}{\partial x} + \tilde{\mu} \frac{\partial \bar{U}}{\partial x} \right) + \bar{\lambda} \left(\frac{\partial \tilde{u}}{\partial x} + \frac{\partial \tilde{v}}{\partial y} + \frac{\partial \tilde{w}}{\partial z} \right) + \tilde{\lambda} \left(\frac{\partial \bar{U}}{\partial x} + \frac{\partial \bar{V}}{\partial y} + \frac{\partial \bar{W}}{\partial z} \right) \\ & \bar{\mu} \left(\frac{\partial \tilde{u}}{\partial y} + \frac{\partial \tilde{v}}{\partial x} \right) + \tilde{\mu} \left(\frac{\partial \bar{U}}{\partial y} + \frac{\partial \bar{V}}{\partial x} \right) \\ & \bar{\mu} \left(\frac{\partial \tilde{u}}{\partial z} + \frac{\partial \tilde{w}}{\partial y} \right) + \tilde{\mu} \left(\frac{\partial \bar{U}}{\partial z} + \frac{\partial \bar{W}}{\partial y} \right) \end{aligned} \right] + \\ & \frac{\partial}{\partial y} \left[\begin{aligned} & \bar{\mu} \left(\frac{\partial \tilde{v}}{\partial x} + \frac{\partial \tilde{u}}{\partial y} \right) + \tilde{\mu} \left(\frac{\partial \bar{V}}{\partial x} + \frac{\partial \bar{U}}{\partial y} \right) \\ & 2 \left(\bar{\mu} \frac{\partial \tilde{v}}{\partial y} + \tilde{\mu} \frac{\partial \bar{V}}{\partial y} \right) + \bar{\lambda} \left(\frac{\partial \tilde{u}}{\partial x} + \frac{\partial \tilde{v}}{\partial y} + \frac{\partial \tilde{w}}{\partial z} \right) + \tilde{\lambda} \left(\frac{\partial \bar{U}}{\partial x} + \frac{\partial \bar{V}}{\partial y} + \frac{\partial \bar{W}}{\partial z} \right) \\ & \bar{\mu} \left(\frac{\partial \tilde{v}}{\partial z} + \frac{\partial \tilde{w}}{\partial y} \right) + \tilde{\mu} \left(\frac{\partial \bar{V}}{\partial z} + \frac{\partial \bar{W}}{\partial y} \right) \end{aligned} \right] + \\ & \frac{\partial}{\partial z} \left[\begin{aligned} & \bar{\mu} \left(\frac{\partial \tilde{w}}{\partial y} + \frac{\partial \tilde{u}}{\partial z} \right) + \tilde{\mu} \left(\frac{\partial \bar{W}}{\partial y} + \frac{\partial \bar{U}}{\partial z} \right) \\ & \bar{\mu} \left(\frac{\partial \tilde{w}}{\partial x} + \frac{\partial \tilde{v}}{\partial z} \right) + \tilde{\mu} \left(\frac{\partial \bar{W}}{\partial x} + \frac{\partial \bar{V}}{\partial z} \right) \\ & 2 \left(\bar{\mu} \frac{\partial \tilde{w}}{\partial z} + \tilde{\mu} \frac{\partial \bar{W}}{\partial z} \right) + \bar{\lambda} \left(\frac{\partial \tilde{u}}{\partial x} + \frac{\partial \tilde{v}}{\partial y} + \frac{\partial \tilde{w}}{\partial z} \right) + \tilde{\lambda} \left(\frac{\partial \bar{U}}{\partial x} + \frac{\partial \bar{V}}{\partial y} + \frac{\partial \bar{W}}{\partial z} \right) \end{aligned} \right] \right\} \end{aligned} \quad (7.14)$$

$$\frac{\partial \tilde{p}}{\partial t} + \frac{\partial}{\partial x} (\bar{\rho} \tilde{u} + \tilde{\rho} \bar{U}) + \frac{\partial}{\partial y} (\bar{\rho} \tilde{v} + \tilde{\rho} \bar{V}) + \frac{\partial}{\partial z} (\bar{\rho} \tilde{w} + \tilde{\rho} \bar{W}) = 0 \quad (7.15)$$

$$\begin{aligned}
& \bar{\rho} C_p \left(\frac{\partial \tilde{T}}{\partial t} + \bar{U} \frac{\partial \tilde{T}}{\partial x} + \tilde{u} \frac{\partial \bar{T}}{\partial x} + \bar{V} \frac{\partial \tilde{T}}{\partial y} + \tilde{v} \frac{\partial \bar{T}}{\partial y} + \bar{W} \frac{\partial \tilde{T}}{\partial z} + \tilde{w} \frac{\partial \bar{T}}{\partial z} \right) + \tilde{\rho} C_p \left(\bar{U} \frac{\partial \bar{T}}{\partial x} + \bar{V} \frac{\partial \bar{T}}{\partial y} + \bar{W} \frac{\partial \bar{T}}{\partial z} \right) \\
& = \left(\frac{\partial \tilde{p}}{\partial t} + \bar{U} \frac{\partial \tilde{p}}{\partial x} + \tilde{u} \frac{\partial \bar{p}}{\partial x} + \bar{V} \frac{\partial \tilde{p}}{\partial y} + \tilde{v} \frac{\partial \bar{p}}{\partial y} + \bar{W} \frac{\partial \tilde{p}}{\partial z} + \tilde{w} \frac{\partial \bar{p}}{\partial z} \right) \\
& + \frac{1}{(\gamma - 1) Pr Re M_\infty^2} \left[\frac{\partial}{\partial x} \left(\bar{k} \frac{\partial \tilde{T}}{\partial x} + \tilde{k} \frac{\partial \bar{T}}{\partial x} \right) + \frac{\partial}{\partial y} \left(\bar{k} \frac{\partial \tilde{T}}{\partial y} + \tilde{k} \frac{\partial \bar{T}}{\partial y} \right) + \frac{\partial}{\partial z} \left(\bar{k} \frac{\partial \tilde{T}}{\partial z} + \tilde{k} \frac{\partial \bar{T}}{\partial z} \right) \right] \\
& + \frac{1}{Re} \left\{ 2\bar{\mu} \left[2 \frac{\partial \bar{U}}{\partial x} \frac{\partial \tilde{u}}{\partial x} + 2 \frac{\partial \bar{V}}{\partial y} \frac{\partial \tilde{v}}{\partial y} + 2 \frac{\partial \bar{W}}{\partial z} \frac{\partial \tilde{w}}{\partial z} + 2 \left(\frac{\partial \bar{U}}{\partial y} + \frac{\partial \bar{V}}{\partial x} \right) \left(\frac{\partial \tilde{u}}{\partial y} + \frac{\partial \tilde{v}}{\partial x} \right) + 2 \left(\frac{\partial \bar{U}}{\partial z} + \frac{\partial \bar{W}}{\partial y} \right) \left(\frac{\partial \tilde{u}}{\partial z} + \frac{\partial \tilde{w}}{\partial y} \right) + \right. \right. \\
& 2 \left(\frac{\partial \bar{V}}{\partial z} + \frac{\partial \bar{W}}{\partial y} \right) \left(\frac{\partial \tilde{v}}{\partial z} + \frac{\partial \tilde{w}}{\partial y} \right) \left. \right] + 2\bar{\mu} \left[2 \left(\frac{\partial \bar{U}}{\partial x} \right)^2 + 2 \left(\frac{\partial \bar{V}}{\partial y} \right)^2 + 2 \left(\frac{\partial \bar{W}}{\partial z} \right)^2 + \left(\frac{\partial \bar{U}}{\partial y} + \frac{\partial \bar{V}}{\partial x} \right)^2 + \left(\frac{\partial \bar{U}}{\partial z} + \frac{\partial \bar{W}}{\partial y} \right)^2 + \right. \\
& \left. \left(\frac{\partial \bar{V}}{\partial z} + \frac{\partial \bar{W}}{\partial y} \right)^2 \right] + \bar{\lambda} \left[2 \left(\frac{\partial \bar{U}}{\partial x} + \frac{\partial \bar{V}}{\partial y} + \frac{\partial \bar{W}}{\partial z} \right) \left(\frac{\partial \tilde{u}}{\partial x} + \frac{\partial \tilde{v}}{\partial y} + \frac{\partial \tilde{w}}{\partial z} \right) \right] + \bar{\lambda} \left[2 \left(\frac{\partial \bar{U}}{\partial x} \right)^2 + 2 \left(\frac{\partial \bar{V}}{\partial y} \right)^2 + 2 \left(\frac{\partial \bar{W}}{\partial z} \right)^2 + 2 \left(\frac{\partial \bar{U}}{\partial x} \frac{\partial \bar{V}}{\partial y} + \right. \right. \\
& \left. \left. \frac{\partial \bar{U}}{\partial x} \frac{\partial \bar{W}}{\partial z} + \frac{\partial \bar{V}}{\partial y} \frac{\partial \bar{W}}{\partial z} \right) \right] \left. \right\} \quad (7.16)
\end{aligned}$$

$$\tilde{\rho} = \gamma M^2 \frac{\tilde{p}}{\bar{T}} - \frac{\rho}{\bar{T}} \tilde{T} \quad (7.17)$$

Where $Re = \rho_e u_e l / \mu_e$ is the Reynolds number, $Pr = C_p \mu_e / k_e$ is the Prandtl number, γ is the ratio of the specific heats. The mean equation of state can be written as:

$$\gamma M^2 P = \rho T \quad (7.18)$$

We consider the stability of locally parallel compressible boundary layer flow. The “locally parallel flow” assumption is the same as used in the application of the Orr-Sommerfeld equation to the incompressible boundary layer flow. Under this assumption,

$$\bar{U} = U(y), \quad \bar{V} = 0, \quad \bar{W} = W(y), \quad \bar{T} = T(y), \quad \bar{\rho} = \rho(y) \quad (7.19)$$

Due to the boundary layer assumption, p is constant across the layer and is equal to $1/\gamma M^2$. In that case $\rho = 1/T$ and Eq. (7.17) simplifies to

$$\tilde{\rho} = \gamma M^2 \frac{\tilde{p}}{\bar{T}} - \frac{\tilde{T}}{\bar{T}^2} \quad (7.20)$$

Equation can be used to eliminate density $\tilde{\rho}$ from Eq. (7.14)-(7.17). Furthermore, we can write

$$\bar{\mu} = \frac{d\mu}{d\bar{T}} \tilde{T}, \quad \bar{\lambda} = \frac{d\lambda}{d\bar{T}} \tilde{T}, \quad \bar{k} = \frac{dk}{d\bar{T}} \tilde{T} \quad (7.21)$$

Plug equation (7.19) and (7.20) into equations (7.14) - (7.17) and simplify, we get

$$\begin{aligned}
& \frac{1}{T} \begin{bmatrix} \frac{\partial \tilde{u}}{\partial t} \\ \frac{\partial \tilde{v}}{\partial t} \\ \frac{\partial \tilde{w}}{\partial t} \end{bmatrix} + \frac{1}{T} \begin{bmatrix} \bar{U} \frac{\partial \tilde{u}}{\partial x} + \tilde{v} \frac{\partial \bar{U}}{\partial y} + \bar{W} \frac{\partial \tilde{u}}{\partial z} \\ \bar{U} \frac{\partial \tilde{v}}{\partial x} + \bar{W} \frac{\partial \tilde{v}}{\partial z} \\ \bar{U} \frac{\partial \tilde{w}}{\partial x} + \tilde{v} \frac{\partial \bar{W}}{\partial y} + \bar{W} \frac{\partial \tilde{w}}{\partial z} \end{bmatrix} = - \begin{bmatrix} \frac{\partial \tilde{p}}{\partial x} \\ \frac{\partial \tilde{p}}{\partial y} \\ \frac{\partial \tilde{p}}{\partial z} \end{bmatrix} + \\
& \frac{1}{Re} \left\{ \frac{\partial}{\partial x} \begin{bmatrix} 2 \left(\bar{\mu} \frac{\partial \tilde{u}}{\partial x} \right) + \bar{\lambda} \left(\frac{\partial \tilde{u}}{\partial x} + \frac{\partial \tilde{v}}{\partial y} + \frac{\partial \tilde{w}}{\partial z} \right) \\ \bar{\mu} \left(\frac{\partial \tilde{u}}{\partial y} + \frac{\partial \tilde{v}}{\partial x} \right) + \frac{d\bar{\mu}}{dT} \tilde{T} \frac{\partial \bar{U}}{\partial y} \\ \bar{\mu} \left(\frac{\partial \tilde{u}}{\partial z} + \frac{\partial \tilde{w}}{\partial y} \right) + \frac{d\bar{\mu}}{dT} \tilde{T} \frac{\partial \bar{W}}{\partial y} \end{bmatrix} + \frac{\partial}{\partial y} \begin{bmatrix} \bar{\mu} \left(\frac{\partial \tilde{v}}{\partial x} + \frac{\partial \tilde{u}}{\partial y} \right) + \frac{d\bar{\mu}}{dT} \tilde{T} \left(\frac{\partial \bar{U}}{\partial y} \right) \\ 2 \left(\bar{\mu} \frac{\partial \tilde{v}}{\partial y} \right) + \bar{\lambda} \left(\frac{\partial \tilde{u}}{\partial x} + \frac{\partial \tilde{v}}{\partial y} + \frac{\partial \tilde{w}}{\partial z} \right) \\ \bar{\mu} \left(\frac{\partial \tilde{v}}{\partial z} + \frac{\partial \tilde{w}}{\partial y} \right) + \frac{d\bar{\mu}}{dT} \tilde{T} \left(\frac{\partial \bar{W}}{\partial y} \right) \end{bmatrix} + \right. \\
& \left. \frac{\partial}{\partial z} \begin{bmatrix} \bar{\mu} \left(\frac{\partial \tilde{w}}{\partial y} + \frac{\partial \tilde{u}}{\partial z} \right) + \frac{d\bar{\mu}}{dT} \tilde{T} \left(\frac{\partial \bar{W}}{\partial y} \right) \\ \bar{\mu} \left(\frac{\partial \tilde{w}}{\partial y} + \frac{\partial \tilde{v}}{\partial z} \right) + \frac{d\bar{\mu}}{dT} \tilde{T} \left(\frac{\partial \bar{W}}{\partial y} \right) \\ 2 \left(\bar{\mu} \frac{\partial \tilde{w}}{\partial z} + \frac{d\bar{\mu}}{dT} \tilde{T} \frac{\partial \bar{W}}{\partial z} \right) + \bar{\lambda} \left(\frac{\partial \tilde{u}}{\partial x} + \frac{\partial \tilde{v}}{\partial y} + \frac{\partial \tilde{w}}{\partial z} \right) \end{bmatrix} \right\} \quad (7.22)
\end{aligned}$$

$$\begin{aligned}
& \frac{\gamma M^2}{T} \frac{\partial \tilde{p}}{\partial t} - \frac{1}{T^2} \frac{\partial \tilde{T}}{\partial t} + \frac{1}{T} \frac{\partial \tilde{u}}{\partial x} + \left(\frac{\gamma M^2}{T} \frac{\partial \tilde{p}}{\partial x} - \frac{1}{T^2} \frac{\partial \tilde{T}}{\partial x} \right) \bar{U} + \frac{1}{T} \frac{\partial \tilde{v}}{\partial y} - \frac{1}{T^2} \frac{\partial \tilde{T}}{\partial y} \tilde{v} + \frac{1}{T} \frac{\partial \tilde{w}}{\partial z} + \left(\frac{\gamma M^2}{T} \frac{\partial \tilde{p}}{\partial z} - \frac{1}{T^2} \frac{\partial \tilde{T}}{\partial z} \right) \bar{W} = 0 \\
& \quad (7.23)
\end{aligned}$$

$$\begin{aligned}
& \frac{1}{\bar{T}} C_p \left(\frac{\partial \tilde{T}}{\partial t} + \bar{U} \frac{\partial \tilde{T}}{\partial x} + \tilde{v} \frac{\partial \bar{T}}{\partial y} + \bar{W} \frac{\partial \tilde{T}}{\partial z} \right) \\
& = \left(\frac{\partial \tilde{p}}{\partial t} + \bar{U} \frac{\partial \tilde{p}}{\partial x} + \bar{W} \frac{\partial \tilde{p}}{\partial z} \right) + \frac{1}{(\gamma-1)PrReM_\infty^2} \left[\frac{\partial}{\partial x} \left(\bar{k} \frac{\partial \tilde{T}}{\partial x} \right) + \frac{\partial}{\partial y} \left(\bar{k} \frac{\partial \tilde{T}}{\partial y} \right) + \frac{\partial}{\partial y} \left(\frac{d\bar{k}}{dT} \tilde{T} \frac{\partial \tilde{T}}{\partial y} \right) + \frac{\partial}{\partial z} \left(\bar{k} \frac{\partial \tilde{T}}{\partial z} \right) \right] \\
& + \frac{1}{Re} \left\{ 2\bar{\mu} \left[2 \left(\frac{\partial \bar{U}}{\partial y} \right) \left(\frac{\partial \tilde{u}}{\partial y} + \frac{\partial \tilde{v}}{\partial x} \right) + 2 \left(\frac{\partial \bar{W}}{\partial y} \right) \left(\frac{\partial \tilde{u}}{\partial z} + \frac{\partial \tilde{w}}{\partial y} \right) + 2 \left(\frac{\partial \bar{W}}{\partial y} \right) \left(\frac{\partial \tilde{v}}{\partial z} + \frac{\partial \tilde{w}}{\partial y} \right) \right] + 2 \frac{d\bar{\mu}}{dT} \tilde{T} \left[\left(\frac{\partial \bar{U}}{\partial y} \right)^2 + \right. \right. \\
& \left. \left. \left(\frac{\partial \bar{W}}{\partial y} \right)^2 \right] \right\} \quad (7.24)
\end{aligned}$$

We may now assume that the velocity, pressure, and temperature fluctuations maybe represented by a harmonic wave of the form

$$(\tilde{u}, \tilde{v}, \tilde{w}) = [\hat{u}(y), \hat{v}(y), \hat{w}(y)] e^{i(\alpha x + \beta z - \omega t)} \quad (7.25)$$

$$\tilde{p} = \hat{p}(y) e^{i(\alpha x + \beta z - \omega t)} \quad (7.26)$$

$$\tilde{T} = \hat{T}(y) e^{i(\alpha x + \beta z - \omega t)} \quad (7.27)$$

Where α, β are the wave numbers and ω is the frequency which, in general, are all complex. In temporal stability theory, α, β are assumed to be real and ω is complex while the converse is true in the spatial stability theory.

Substituting equations (7.25)-(7.27) into (7.22)-(7.24), it can be shown that the linear disturbances satisfy the following system of ordinary differential equations

$$(AD^2 + BD + C)\phi = 0 \quad (7.28)$$

Where ϕ is a five-element vector defined by

$$\{\hat{u}, \hat{v}, \hat{p}, \hat{T}, \hat{w}\}^{tr}.$$

Here $D \equiv d/dy$, while A is given as

$$A = \begin{bmatrix} 1 & & \cdots & & 0 \\ & 1 & & & \\ \vdots & & 0 & & \vdots \\ 0 & & \cdots & 1 & \\ & & & & 1 \end{bmatrix}$$

and B and C are 5×5 matrices whose nonzero elements are given in Appendix A.

Since we are interested in two-dimensional basic flow, the velocity component $W(y)$ may be set to zero and \hat{w} momentum equation may be dropped, thus the order of the system is reduced.

The boundary conditions for equation (7.28) are:

$$y = 0, \quad \phi_1 = \phi_2 = \phi_4 = \phi_5 = 0 \quad (7.29)$$

$$y \rightarrow \infty, \quad \phi_1, \phi_2, \phi_4, \phi_5 \rightarrow 0 \quad (7.30)$$

Here temperature perturbation are assumed to vanish at the solid boundary whereas the mean flow may be treated with an insulated wall.

Equations (7.28) - (7.30) constitute an eigenvalue problem described by the complex dispersion relation

$$\omega = \omega(\alpha, \beta) \quad (7.31)$$

and the determination of this relation is essentially the subject.

7.2 Second Order Finite-Difference (2FD) Method

There are two classes of numerical methods that can be used for computing the eigenvalues: global and local methods. For global method a generalized eigenvalue problem can be set up and the eigenvalues are obtained by standard algorithm like LR or QR or QZ. These algorithm yield all the eigenvalues of discretized system and a guess for the eigenvalues

is not needed. The local method requires an initial guess. Only the eigenvalue that happens to lie in the neighborhood of the guess is computed using iterative techniques such as Newton's method. Global methods are computationally much more expensive than local methods but if there are no guess of the eigenvalues, it would be useful.

The methods we described below is for temporal stability where wave number α , β are known and the desired eigenvalue is the complex frequency ω .

The governing system of equations (7.28) is represented using a second-order accurate finite-difference formula on a staggered mesh. First the boundary layer coordinate y , $0 \leq y \leq y_{\max}$, is mapped onto the computational domain $0 \leq \eta \leq 1$ by the algebraic mapping

$$y = \frac{a\eta}{b-\eta} \quad (7.32)$$

where $b = 1 + a/y_{\max}$. Here y_{\max} is the location where free-stream boundary conditions are satisfied and a is a scaling parameter chosen to optimize the accuracy of the calculations. Here we use $a = 0.1$ which will make the meshing grids thicker in the boundary layer.

The computational domain η is divided into equal intervals and the second-order equations are represented as

$$\begin{aligned} f_1 A_j \left[\frac{\phi_{j+1} - 2\phi_j + \phi_{j-1}}{\Delta\eta^2} \right] + d_1 \left[(f_2 A_j + f_3 B_j) \left(\frac{\phi_{j+1} - \phi_{j-1}}{2\Delta\eta} \right) + C_j \phi_j \right] \\ + d_2 \left[f_3 B_j \left(\frac{\phi_{j+1/2} - \phi_{j-1/2}}{\Delta\eta} \right) + C_j \left(\frac{\phi_{j+1/2} + \phi_{j-1/2}}{2} \right) \right] = 0 \quad (j = 1, \dots, N-1), \end{aligned} \quad (7.33)$$

where ϕ_j is the value of ϕ at $\eta = j/N$ and has components ϕ_{kj} ($k = 1, \dots, 5$). Also, $d_1 = 1, d_2 = 0$, except $d_1 = 0, d_2 = 1$ for the \hat{p} component of ϕ , and

$$f_1 = \frac{(b-\eta)^4}{b^2 a^2}$$

$$f_2 = \frac{2(b - \eta)^3}{b^2 a^2}$$

$$f_3 = \frac{(b - \eta)^2}{ba}$$

The first-order continuity equation is represented as

$$f_3 B_{j+1/2} \frac{\phi_{j+1} - \phi_j}{\Delta \eta} + C_{j+1/2} \phi_{j+1/2} = 0 \quad (j = 0, \dots, N - 1) \quad (7.34)$$

Equations 7.33-7.34 along with boundary conditions (7.29)-(7.30) represent $5N+4$ equations for $5N+4$ unknowns. Since the velocity and temperature disturbances are assumed to be identically zero at the solid boundary the system reduces to $5N$ equations for $5N$ unknowns. This is a block-tridiagonal system of equations with 5×5 blocks. Note that no artificial pressure boundary conditions are needed since we use staggered mesh.

The problem should be converted to an eigenvalue problem:

$$\bar{A} \phi = \omega \bar{B} \phi \quad (7.35)$$

where ω is the eigenvalue and ϕ is the discrete representation of the eigenfunction. The eigenvalue is determined by the determinate condition

$$\text{Det} |\bar{A} - \omega \bar{B}| = 0 \quad (7.36)$$

which is the standard matrix eigenvalue problem, solvable by LR or QR methods[14] if \bar{B} is invertible or QZ method if not.

7.3 Numerical Results

We chose the velocity profile from $Re_x=187,000$ as the input section of temporal case (Fig. 7.2). Flow parameters are described in table 7.1. Mach number M , Reynolds number Re , velocity profile position x_m , inflow temperature T_∞ , wall temperature T_w and nondimensional displacement thickness δ^* (scaled with length scale $l = \sqrt{\nu_e x / u_e}$, where ν_e is the kinematic viscosity at free stream temperature) are presented.

Table 7.1 Flow Parameters

M_∞	Re	x_{in}	δ^*	T_w	T_∞
0.5	1000	187	1.8236	273.15	273.15

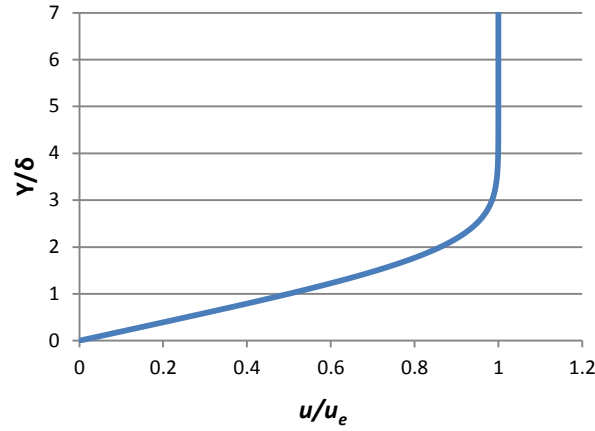


Figure 7.2. Velocity profile near boundary layer used in numerical analysis

Figure 7.3 shows the solution of eigenvalue problem in equation (7.35) using our code.

We can also get the corresponding physical solution ω , whose imaginary part ω_i is 0.0593 for this case. The positive value of imaginary part means flow at this position is unstable.

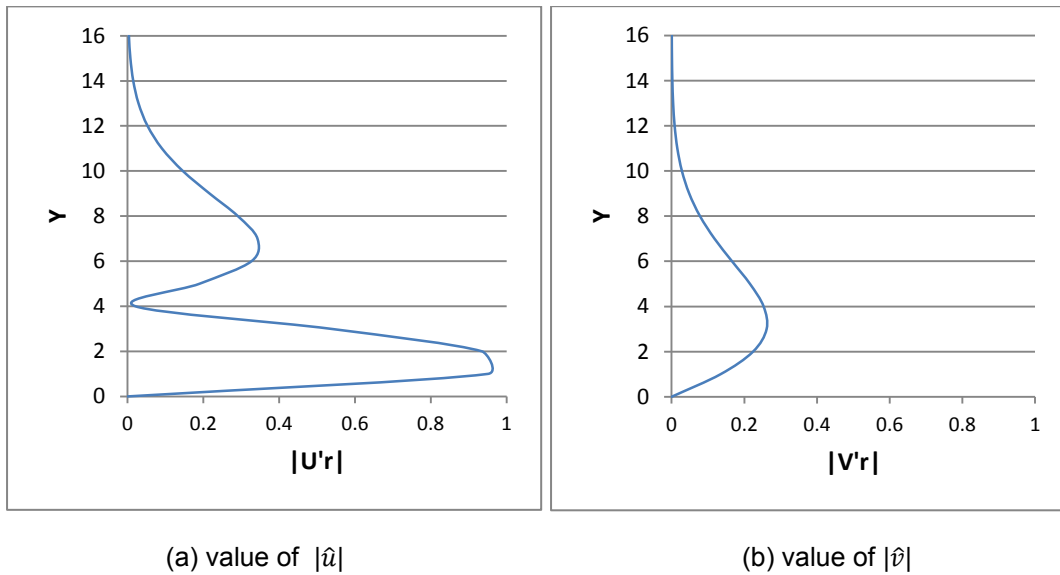
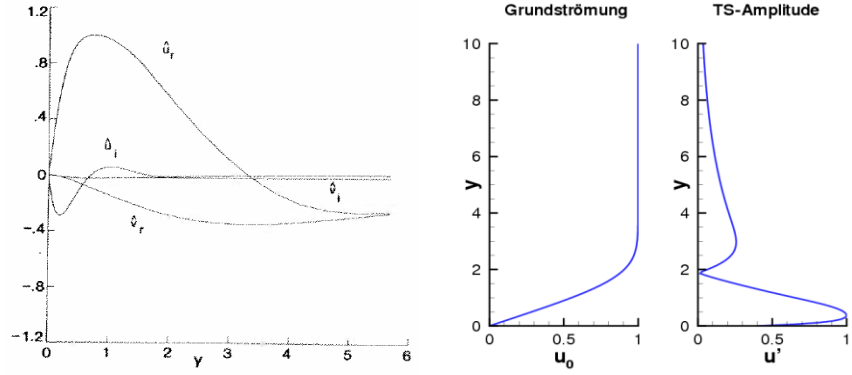


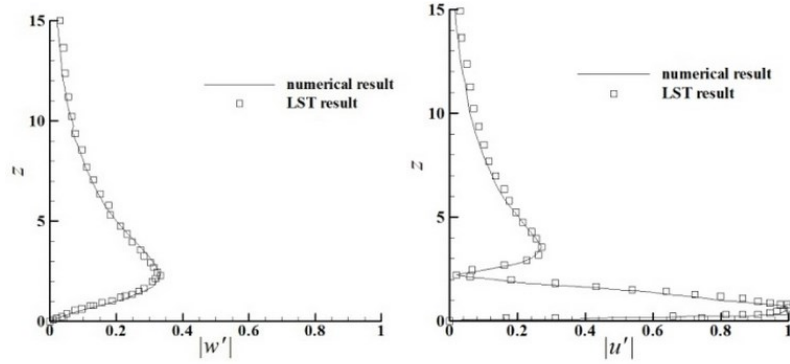
Figure 7.3 Eigenvector Function at $Re_x = 187,000$

For reference, eigenfunctions of Malik et. al. [61] and Lu [60] were listed for qualitative comparison. Since different cases are different in Mach number and Reynolds number, quantitative comparison is not available.



(a) Eigenfunction from Malik[59]

(b) Eigenfunction of TS wave by A. Babucke



(c) Numerical and LST profiles of TS wave from P. Lu et al [60]

Figure 7.4 Eigenfunction of compressible stability equations for comparison

The mechanism of the ring generation is a real 3D process. Study in non-linear, 3D and compressible stability analysis is needed to reveal the full mechanism of the shear layer instability behind MVG. The current study only involves temporal, linear, and compressible stability analysis which can be considered as a first step to study the wake instability of MVG.

Chapter 8

CONCLUDING REMARKS

In this work, by using the implicitly implemented large eddy simulation method with fifth order bandwidth-optimized WENO scheme, studies are made on the MVG controlled ramp flow at $M=2.5$ and $Re_0=5760$. A body-fitted grid scheme is adopted to make the computational accuracy as high as possible.

Through the computation on the MVG-ramp flow, the same basic wave system is obtained as that given by Babinsky. Reasonable agreement in the shape of shocks between the computation and experiment is obtained. The implicitly implemented LES has been demonstrated to be capable of resolving the detailed structures in the supersonic micro-ramp flow, such as the primary vortex pair and the momentum deficit. A number of new findings and new mechanisms are obtained through the LES simulation because of the high order accuracy and high resolution of the computation, which include:

i). The complete separation topology is obtained, a representative pair of spiral points are found on the plate beside the end of MVG, which implies a new five-pair-vortex model around the MVG, and the model is different from the one reported by previous literatures.

ii). The mechanism of the formation of the momentum deficit is investigated. The momentum deficit originates from the fluid in the lower portion of the incoming boundary layer along the whole span of the micro-ramp, while the high momentum fluid in the near wall region behind the micro-ramp is from the higher portion of the upstream boundary.

iii). A new phenomenon and its mechanism are discovered in MVG-ramp flow control, i.e., the vortex rings generated by the high shear layer. Vortex rings are generated and strongly interact with the separation zone and the separation shock, and play an important role in the reduction of the size of the separation zone. Base on numerical results, the vortex ring structure is studied in detail. The inflection points inside the momentum deficit area are found. The mechanism for the vortex rings was analyzed and found that, the existence of the high shear

layer and inflection surface generated by the momentum deficit will cause the corresponding Kelvin-Helmholtz instability, which develops into a series of vortex rings. The experiment work demonstrated that a chain of vortex rings exist in the flow field after the MVG, and these structures qualitatively resemble the vortex structure found by the numerical simulation. The relation between spanwise and streamwise vorticities are investigated and the vorticity conservation control the process of the vortex development.

iv). The flow separation has been clearly revealed and the current numerical result agrees with the experimental observation through the velocity contours. The spiral points at the rear of the micro-ramp can now be understood as the cross-sections of the small scale vortices. Through the vortex line method, these vortices take the form of Ω -like shape and wrap the recirculation region. The micro-ramp wake obtains similar flow structure as the rear separation where high speed flow wrapping the low speed with shear layer in between. Similar Ω -shaped vortex lines have been a proof. However the vortex lines in the wake region may exhibit extended leg portions corresponding to the streamwise vortices. A conceptual model for the common vortical structure for both the rear separation and the wake region is brought about for better understanding.

Stability analysis on compressible flow over a flat plate was studied. Global method with second order finite-difference method on staggered grids are used to solve the eigenvalue problem. The temporal stability analysis was able to reveal the whole spectrum and is the first step to reveal the full mechanism of the 3D shear layer instability behind MVG.

Appendix A

The non-zero elements of the coefficient matrix B, C in Eq. (7.28)

$$B_{11} = \frac{1}{\mu} \frac{d\mu}{d\bar{T}} T'$$

$$B_{12} = i\alpha l_1$$

$$B_{14} = \frac{1}{\mu} \frac{d\mu}{d\bar{T}} U'$$

$$B_{21} = i\alpha l_1/l_2$$

$$B_{22} = \frac{1}{\mu} \frac{d\mu}{d\bar{T}} T'$$

$$B_{23} = -R_e/(l_2 \mu)$$

$$B_{25} = i\beta l_1/l_2$$

$$B_{32} = 1$$

$$B_{41} = 2(\gamma - 1)\sigma M^2 U'$$

$$B_{44} = 2k'/k$$

$$B_{45} = 2(\gamma - 1)\sigma M^2 W'$$

$$B_{52} = i\beta l_1$$

$$B_{54} = \frac{1}{\mu} \frac{d\mu}{d\bar{T}} W'$$

$$B_{55} = \frac{1}{\mu} \frac{d\mu}{d\bar{T}} T'$$

$$C_{11} = -i\xi R_e/(\mu T) - (l_2 \alpha^2 + \beta^2)$$

$$C_{12} = -R_e U'/(\mu \bar{T}) + \frac{i\alpha}{\mu} \frac{d\mu}{d\bar{T}} \bar{T}'$$

$$C_{13} = -i\alpha R_e/\mu$$

$$C_{14} = \frac{1}{\mu} \frac{d\mu}{d\bar{T}} U'' + \frac{1}{\mu} \frac{d^2 \mu}{d\bar{T}^2} \bar{T}' U'$$

$$C_{15} = -\alpha \beta l_1$$

$$C_{21} = i\alpha \frac{1}{\mu} \frac{d\mu}{d\bar{T}} \bar{T}' l_0/l_2$$

$$C_{22} = -i\xi R_e/(l_2 \mu \bar{T}) - (\alpha^2 + \beta^2)/l_2$$

$$C_{24} = i \frac{1}{\mu} \frac{d\mu}{d\bar{T}} (\alpha U' + \beta W') / l_2$$

$$C_{25} = i\beta \frac{1}{\mu} \frac{d\mu}{d\bar{T}} \bar{T}' l_0 / l_2$$

$$C_{31} = i\alpha$$

$$C_{32} = -\bar{T}' / \bar{T}$$

$$C_{33} = i\gamma M^2 \xi$$

$$C_{34} = -i\xi / \bar{T}$$

$$C_{35} = i\beta$$

$$C_{42} = 2i(\gamma - 1)M^2 \alpha (\alpha U' + \beta W') - \sigma R_e \bar{T}' / \mu \bar{T}$$

$$C_{43} = i\xi (\gamma - 1)M^2 \sigma R / \mu$$

$$C_{44} = -i\xi R_e \sigma / (\mu \bar{T}) - (\alpha^2 + \beta^2) + (\gamma - 1)M^2 \sigma \frac{1}{\mu} \frac{d\mu}{d\bar{T}} (U'^2 + W'^2) + k'' / k$$

$$C_{51} = -\alpha \beta l_1$$

$$C_{52} = i\beta \left(\frac{1}{\mu} \frac{d\mu}{d\bar{T}} \right) \bar{T}' - R_e W' / (\mu \bar{T})$$

$$C_{53} = -i\beta R_e / \mu$$

$$C_{54} = \frac{1}{\mu} \frac{d\mu}{d\bar{T}} W'' + \frac{1}{\mu} \frac{d^2 \mu}{d\bar{T}^2} \bar{T}' W'$$

$$C_{55} = -i\xi R_e / (\mu \bar{T}) - (\alpha^2 + l_2 \beta^2)$$

where $()' \equiv d/d_y$ and

$$\xi = \alpha \bar{U} + \beta \bar{W} - \omega$$

$$l_j = j + \lambda / \mu$$

References

- [1] Lin J. C. Review of Research on Low-Profile Vortex Generators to Control Boundary-Layer Separation. Progress in Aerospace Sciences, Vol. 38, pp.389-420(2002).
- [2] Ashill, P. R., Fulker, J. L., Hackett, K. C. A Review of Recent Developments in Flow Control. The Aeronautical Journal, 109, 1095, pp.205-232(2005).
- [3] Anderson, B. H., Tinapple, J. Surber, L. Optimal Control of Shock Wave Turbulent Boundary Layer Interaction Using Micro-Array Actuation. AIAA paper 2006-3197.
- [4] Hoden, H. A., Babinsky, H. Vortex Generators Near Shock/Boundary Layer Interactions. AIAA paper 2004-1242.
- [5] Ford, C. W., P., Babinsky, H. Micro-Ramp Control for Oblique Shock Wave/Boundary Layer Interaction. AIAA paper 2007-4115.
- [6] Holden, H., Babinsky. Effect of Microvortex Generators on Separated Normal Shock/Boundary Layer Interactions. AIAA J. pp.170-173(2007).
- [7] Babinsky, H., Li, Y., Ford, C. W. P. Microramp Control of Supersonic Oblique Shock-Wave/Boundary-Layer Interactions. AIAA J., Vol. 47, No. 3, pp.668-675(2009).
- [8] Ghosh, S., Choi J., Edwards, J. R. RANS and Hybrid LES/RANS Simulations of the Effects of Micro Vortex Generators Using Immersed Boundary Methods. AIAA paper 2008-3726.
- [9] Lee, S. Loth E. , Wang, C. LES of Supersonic Turbulent Boundary Layers with μ VG's. AIAA Paper 2007-3916.
- [10] Lee, S., Loth, E. Supersonic Boundary Layer Interactions with Various Micro-Vortex Generator Geometries. AIAA Paper 2009-3712.
- [11] Dolling, D. S., Murthy, M. Unsteadiness of the Separation Shock Wave Structure in a Supersonic Compression Ramp Flowfield. AIAA J., Vol. 12, pp.1628-1634(1983).
- [12] Dolling, D. S. High-Speed Turbulent Separated Flows: Consistency of Mathematic Models and Flow Physics. AIAA J., Vol. 36, pp. 725-732(1998).

- [13] Dolling, D. S. Fifty Years of Shock-Wave/Boundary-Layer Interaction Research: What next? AIAA J., Vol. 39, pp. 1517-1531(2001).
- [14] Settles, G. S. Dodson, L. J. Supersonic and Hypersonic Shock/Boundary Layer Interaction Database. AIAA J., Vol. 32, 1377-1383(1994).
- [15] Dussauge, J. P., Dupont, P., Debieve, J. F. Unsteadiness in Shock Wave Boundary Layer Interaction with Separation. Aerospace Science and Technology, Vol. 10, No. 2, pp.85-91(2006).
- [16] Andreopoulos, J., Agui, J. H., Briassulis, G. Shock Wave-Turbulence Interactions, Annu. Rev. Fluid Mech., Vol. 32, pp.309-345(2000).
- [17] Loginov, M. S., Adams, N. A., Zheltovodov, A. A. Large-Eddy Eimulation of Shock-Wave/Turbulent-Boundary-Layer Interaction. J. Fluid Mech., Vol. 565, pp. 135-169(2006).
- [18] Wilcox, D., Turbulence Modeling for CFD, DCW Industries, Inc., 1993
- [19] Zheltovodov, A. A. Advances and Problems in Modeling of Shock Wave Turbulent Boundary Layer Interactions. Proceedings of the international Conference on the Methods of Aerophysical research, Institute of Theoretical and Applied Mechanics, Novosibirsk, Russia, pp.149-157(2004)
- [20] Rizzetta, D., Visbal, M. Large Eddy Simulation of Supersonic Compression-Ramp Flow by High-Order Method. AIAA J., Vol. 39, No. 12, pp.2283-2292(2001).
- [21] Kaenel, R.V, Kleiser, L. Adams, N. A. Vos, J. B. Large-Eddy Simulation of Shock-Turbulence Interaction. AIAA J., Vol. 42, No. 12, pp.2516-2528(2004).
- [22] Adams, N. A. Direct simulation of the turbulent boundary layer along a compression ramp at $M = 3$ and $Re_\theta = 1685$. J. Fluid Mech., Vol. 420, pp. 47-83(2000).
- [23] Wu M. Martin, M. P. Direct Numerical Simulation of Supersonic Turbulent Boundary Layer over a Compression Ramp. AIAA J., Vol. 45, No. 4(2007).

- [24] Martín, M. P. Direct Numerical Simulation of Hypersonic Turbulent Boundary Layers. Part 1. Initialization and Comparison with Experiments. *J. Fluid Mech.*, vol. 570, pp. 347–364(2007).
- [25] Ringuette, M. Wu, M., Martín, M. P. Low Reynolds Number Effects in a Mach 3 Shock/Turbulent-Boundary-Layer Interaction. *AIAA J.*, Vol. 46, No. 7, pp.1884–1887(2008).
- [26] Wu, M., Martín, M. P. Analysis of Shock Motion in Shockwave and Turbulent Boundary Layer Interaction Using Direct Numerical Simulation Data. *J. Fluid Mech.*, Vol. 594, pp. 71–83(2008).
- [27] Ringuette, M. J. Wu, M., Martín, M. P. Coherent Structures in Direct Numerical Simulation of Turbulent Boundary Layers at Mach 3. *J. Fluid Mech.*, vol. 594, pp. 59–69(2008).
- [28] Priebe, S. Wu, M., Martín, M. P. Direct Numerical Simulation of a Reflected-Shock-Wave/Turbulent-Boundary-Layer Interaction. *AIAA J.*, Vol. 47, No. 5, pp.1173–1185(2009).
- [29] Bookey, P. Wyckham, C., Smits, A. Experimental Investigations of Mach 3 Shock-Wave Turbulent Boundary Layer Interactions. *AIAA Paper 2005-4899*, 2005.
- [30] LCattafesta III, L.N, Sheplak, M., Actuators for active flow control, *Annual Review of Fluid Mechanics* 43 (2011) 247–272. doi:10.1146/annurev-fluid-122109-160634.
- [31] Blinde, P.L., Humble, R. A., van Oudheusden, B.W., Scarano, F., Effects of micro-ramps on a shock wave/turbulent boundary layer interaction. *Shock Waves* 19 (6) (2009) 507–520. doi:10.1007/s00193-009-0231-9.
- [32] Saad, R., Erdem, E., Yang, L., Kontis, K., Experimental studies on micro ramps at Mach 5, in: Paper 2816, Proceedings of the 28th International, Symposium on Shock Waves, Manchester, U.K., 17–22 July, 2011.

- [33] Sun, Z., Schrijer, F.J.J., van Oudheusden, F.S.B.W., The three dimensional flow organization past a micro-ramp in a supersonic boundary layer, in press, *Physics of Fluids* (2012).
- [34] König, B., Paatzold, M., Lutz, T., Krämer, E., Rosemann, H., Richter, K., Uhlemann, H., Numerical and experimental validation of three dimensional shock control bumps, *Journal of Aircraft* 46 (2) (2009) 675–682. doi:10.2514/1.41441.
- [35] Marxen, O., Rist, U., Mean Flow Deformation in a Laminar Separation Bubble: Separation and Stability Characteristics, *Journal of Fluid Mechanics* (2010), vol. 660, pp. 37-54.
- [36] Smits, A. J., Dussauge, J. P. *Turbulent Shear Layers in Supersonic Flow*, 2nd ed., Springer Verlag, New York(2006).
- [37] Boris, J. P. Grinstein, F. F., Oran, E. S , Kolbe, R. J. New insights into large eddy simulation. *J. Fluid Dyn. Res.*, Vol. 10, 1992, pp. 199-228.
- [38] Fureby C. , Grinstein, F. F. Monotonically Integrated Large Eddy Simulation of Free Shear Flows. *AIAA J.*, Vol. 37, No. 5, pp.544-556(1999).
- [39] Fureby C., Grinstein, F. F. Large Eddy Simulation of High-Reynolds-Number and wall-Bounded Flows. *J. Comput. Phys.*, Vol. 181, pp. 68-97(2002).
- [40] Grinstein, F. F., Margolin, L. G., Rider, W. J. *Implicit Large Eddy Simulation*, Cambridge university press(2007).
- [41] Visbal, M. R., Morgan, P. E. , Rizzetta, D. P. An Implicit LES Approach Based on High-Order Compact Differencing and Filtering Scheme. *AIAA paper* 2003-4098.
- [42] Morgan, P. E. Rizzetta D. P. , Visbal, M. R. Large-Eddy Simulation of Separation Control for Flow over a Wall-Mounted Hump. *AIAA J.*, Vol. 45, No. 11, pp.2643-2660(2007).
- [43] Rizzetta, D. P. Visbal, M. R. Gaitonde, D. Large-Eddy Simulation of the Supersonic Compression-Ramp Flow by High-Order Method. *AIAA J.*, Vol. 39, No. 12,(2001).
- [44] Rizzetta, D. P. Visbal, M. R. Application of Large-Eddy Simulation to Supersonic Compression Ramps. *AIAA J.*, Vol. 40, No.8, pp.1574-1581(2002).

- [45] Garnier, E. On the Use of Shock-Capturing Schemes for Large-Eddy Simulation. J. Comput. Phys., Vol. 153, pp. 272-311(1999).
- [46] Ladeinde, F. Cai, X. , Visbal, M. R. , Gaitonde, D. V. Turbulent spectra characteristics of high order schemes for direct and large eddy simulation. Applied Num. Math., Vol. 36, pp. 447-474(2001).
- [47] Gao, R. Yu, J, Kong, W., Yan, C. Evaluation of a WENO Method in Implicit Large Eddy Simulation of Circular Cylinder Flow. The 2nd International Conference on Computer and Automation Engineering (ICCAE), Vol. 5(2010).
- [48] G.S. Jiang and C.W. Shu, Efficient implementation of weighted ENO scheme. J. Comput. Phys. 126 (1996), pp. 202–228.
- [49] Cockburn, B., Shu, C. W. TVD Runge-Kutta Local Projection Discontinuous Galerkin Finite Element Method for Conservation Laws II: General FrameWork. Mathematics of Computation, Vol. 52, No. 186, pp.411-443(1989).
- [50] Spekreijse, S. P. Elliptic Grid Generation Based on Laplace Equations and Algebraic Transformations. J. Comput. Phys., Vol. 118, pp.38-61(1995).
- [51] Li, Q., Liu, C. LES for Supersonic Ramp Control Flow Using MVG at $M=2.5$ and $Re_\theta=1440$. AIAA paper 2010-592.
- [52] Lund, T. S., Wu, X., Squires, K. D. Generation of turbulent inflow data for spatially developing boundary layer simulations. J. Comput. Phys. 140, 233–258(1998).
- [53] Liu C. and Chen, L. Study of Mechanism of Ring-Like Vortex Formation in Late Flow Transition. AIAA Paper 2010-1456.
- [54] Guarini, S. E.; Moser, R. D.; Shariff, K; Wray, A. Direct numerical simulation of a supersonic turbulent boundary layer at Mach 2.5. Journal of Fluid Mechanics, vol. 414, Issue 01, p.1-33(2000)
- [55] Tufo, H. M. , Fischer, P. F., Papka, M. E. , Blom, K. Numerical Simulation and Immersive Visualization of Hairpin Vortices. Conference on High Performance Networking and

- Computing archive, Proceedings of the 1999 ACM/IEEE conference on Supercomputing (CDROM) (1999).
- [56] Lu, F. Liu, C. Li, Q, Pierce, A. Experimental and Numerical Study of Multi-Ring Mechanism from Micro Vortex Generators for Shock/Boundary Layer Interaction Control. AIAA paper 2010-4623.
- [57] Y Yan, Q Li, C Liu, Numerical discovery and experimental confirmation of vortex ring generation by microramp vortex generator. Applied Mathematical Modelling 36 (11), 5700-5708
- [58] Y Yan, C Chen, X Wang, C Liu [LES study on the mechanism of vortex rings behind supersonic MVG with turbulent inflow](#) AIAA paper 1093
- [59] L. M. Mack, Computation of the stability of the compressible laminar boundary layer, Methods in Computational Physics, Academic Press, New York, 1965, Vol. 4, p. 247
- [60] L. M. Mack, Boundary Layer Linear Stability Theory, AGARD Report No. 709, 1984
- [61] M. R. Malik, Numerical Methods for Hypersonic Boundary Layer Stability, Journal of Computational Physics 86, 376-413(1990)
- [62] C. Liu, L. Chen, Study of mechanism of ring-like vortex formation in late flow transition, AIAA paper 2010-4623.
- [63] Mohd R. Saad, Hossein Zare-Behtash, Azam Che Idris and Konstantinos Kontis. "Micro-Ramps for Hypersonic Flow Control". *Micromachines* 2012, 3, 1-x manuscripts; doi:10.3390/mi30x000x
- [64] Lee, S. Loth E. , Wang, C. "LES of Supersonic Turbulent Boundary Layers with μ VG's." AIAA Paper 2007-3916.
- [65] S. Lee and E. Loth, Supersonic boundary-layer interactions with various micro-vortex generator geometries, Aeronautical J. 113 (1149) (2009) 683-697.

- [66] Li, Q., Yan, Y., Lu, P., Pierce, A., Liu, C. and Lu, F., "Numerical and Experimental Studies on the Separation Topology of the MVG Controlled Flow at $M=2.5$," AIAA paper 2011-72.
- [67] Lu, F. K., Pierce, A. J., Shih, Y., Liu, C. and Li, Q., "Experimental and Numerical Study of Flow Topology Past Micro Vortex Generators," AIAA 2010-4463.
- [68] Li, Q., Yan, Y., Liu, C., Lu F., Pierce, A. Numerical and experimental studies on the separation topology of the MVG controlled flow at $M=2.5$ and $Re_\theta=1440$. 49th AIAA Aerospace Sciences Meeting(2011).
- [69] Sun, Z., Schrijer, F.F.J., Scarano, F., and Oudheusden, B.W.V., "PIV Investigation of the 3D Instantaneous Flow Organization behind a Micro-Ramp in a Supersonic Boundary Layer, " University of Delft, ISSW28, July 17-22, 2011, Manchester, UK

Biographical Information

Xiao Wang has received a Bachelor and Masters' degree in Civil Engineering from Hunan University in China. His research interests include the numerical simulation of Navier-Stokes flows and flow control.